Monthly Notices
of the
ROYAL ASTRONOMICAL SOCIETY

Mon. Not. R. Astron. Soc. **418,** 1526–1556 (2011) doi:10.1111/j.1365-2966.2011.19387.x

Dark matter profiles and annihilation in dwarf spheroidal galaxies: prospectives for present and future γ-ray observatories – I. The classical dwarf spheroidal galaxies

A. Charbonnier,[1] C. Combet,[2] M. Daniel,[3] S. Funk,[4] J. A. Hinton,[2⋆]
D. Maurin[1,2,5,6⋆] C. Power,[2,7] J. I. Read,[2,8] S. Sarkar,[9] M. G. Walker[10,11⋆]
and M. I. Wilkinson[2]

[1]*Laboratoire de Physique Nucléaire et Hautes Energies, CNRS-IN2P3/Universités Paris VI et Paris VII, 4 Place Jussieu, Tour 33, 75252 Paris Cedex 05, France*
[2]*Department of Physics and Astronomy, University of Leicester, Leicester LE1 7RH*
[3]*Department of Physics, Durham University, South Road, Durham DH1 3LE*
[4]*W. W. Hansen Experimental Physics Laboratory, Kavli Institute for Particle Astrophysics and Cosmology, Department of Physics and SLAC National Accelerator Laboratory, Stanford University, Stanford, CA 94305, USA*
[5]*Laboratoire de Physique Subatomique et de Cosmologie, CNRS/IN2P3/INPG/Université Joseph Fourier Grenoble 1, 53 avenue des Martyrs, 38026 Grenoble, France*
[6]*Institut d'Astrophysique de Paris, UMR7095 CNRS, Université Pierre et Marie Curie, 98 bis bd Arago, 75014 Paris, France*
[7]*International Centre for Radio Astronomy Research, The University of Western Australia, 35 Stirling Highway, Crawley, WA 6009, Australia*
[8]*Department of Physics, Institute for Astronomy, ETH Zürich, Wolfgang-Pauli-Strasse 16, CH-8093 Zürich, Switzerland*
[9]*Rudolf Peierls Centre for Theoretical Physics, University of Oxford, 1 Keble Road, Oxford OX1 3NP*
[10]*Institute of Astronomy, University of Cambridge, Madingley Road, Cambridge CB3 0HA*
[11]*Harvard–Smithsonian Center for Astrophysics, 60 Garden Street, Cambridge, MA 02138, USA*

Accepted 2011 July 5. Received 2011 July 1; in original form 2011 April 3

ABSTRACT

Due to their large dynamical mass-to-light ratios, dwarf spheroidal galaxies (dSphs) are promising targets for the indirect detection of dark matter (DM) in γ-rays. We examine their detectability by present and future γ-ray observatories. The key innovative features of our analysis are as follows: (i) we take into account the *angular size* of the dSphs; while nearby objects have higher γ-ray flux, their larger angular extent can make them less attractive targets for background-dominated instruments; (ii) we derive DM profiles and the astrophysical J-factor (which parametrizes the expected γ-ray flux, independently of the choice of DM particle model) for the classical dSphs *directly* from photometric and kinematic data. We assume very little about the DM profile, modelling this as a smooth split-power-law distribution, with and without subclumps; (iii) we use a Markov chain Monte Carlo technique to marginalize over unknown parameters and determine the sensitivity of our derived J-factors to both model and measurement uncertainties; and (iv) we use simulated DM profiles to demonstrate that our J-factor determinations recover the correct solution within our quoted uncertainties.

Our key findings are as follows: (i) subclumps in the dSphs do *not* usefully boost the signal; (ii) the sensitivity of atmospheric Cherenkov telescopes to dSphs within $\sim$20 kpc with cored haloes can be up to $\sim$50 times worse than when estimated assuming them to be point-like. Even for the satellite-borne *Fermi*-Large Area Telescope (*Fermi*-LAT), the sensitivity is significantly degraded on the relevant angular scales for long exposures; hence, it is vital to consider the angular extent of the dSphs when selecting targets; (iii) *no* DM profile has been ruled out by current data, but using a prior on the inner DM cusp slope $0 \leq \gamma_{\rm prior} \leq 1$ provides J-factor estimates accurate to a factor of a few if an appropriate angular scale is chosen; (iv) the J-factor

⋆E-mail: jah85@leicester.ac.uk (JAH); dmaurin@lpsc.in2p3.fr (DM); walker@ast.cam.ac.uk (MGW)

is best constrained at a critical integration angle $\alpha_c = 2r_h/d$ (where r_h is the half-light radius and d is the distance from the dwarf) and we estimate the corresponding sensitivity of γ-ray observatories; (v) the 'classical' dSphs can be grouped into three categories: well constrained and promising (Ursa Minor, Sculptor and Draco), well constrained but less promising (Carina, Fornax and Leo I), and poorly constrained (Sextans and Leo II); and (vi) observations of classical dSphs with the *Fermi*-LAT integrated over the mission lifetime are more promising than observations with the planned Cherenkov Telescope Array for DM particle mass $\lesssim 700$ GeV. However, even the *Fermi*-LAT will *not* have sufficient integrated signal from the classical dwarfs to detect DM in the 'vanilla' Minimal Supersymmetric Standard Model. Both the Galactic Centre and the 'ultrafaint' dwarfs are likely to be better targets and will be considered in future work.

Key words: astroparticle physics – methods: miscellaneous – galaxies: dwarf – galaxies: kinematics and dynamics – dark matter – gamma-rays: general.

1 INTRODUCTION

The detection of γ-rays from dark matter (DM) annihilation is one of the most promising channels for indirect detection (Gunn et al. 1978; Stecker 1978). Since the signal goes as the DM density squared, the Galactic Centre seems to be the obvious location to search for such a signal (Silk & Bloemen 1987). However, it is plagued by a confusing background of astrophysical sources (see e.g. Aharonian et al. 2004). For this reason, the dwarf spheroidal galaxies (dSphs) orbiting the Milky Way have been flagged as favoured targets, given their potentially high DM densities and small astrophysical backgrounds (Lake 1990; Evans, Ferrer & Sarkar 2004).

Despite the growing amount of kinematic data from the classical dSphs, the inner parts of their DM profiles remain poorly constrained and can generally accommodate both cored or cuspy solutions (see e.g. Koch et al. 2007; Strigari et al. 2007a; Walker et al. 2009a, hereinafter W09). There are two dSphs – Fornax and Ursa Minor – that show indirect hints of a cored distribution (Kleyna et al. 2003; Goerdt et al. 2006); however, in both cases, the presence of a core is inferred based on a timing argument that assumes we are not catching the dSph at a special moment. Theoretical expectations remain similarly uncertain. Cusps are favoured by cosmological models that model the DM alone, assuming it is cold and collisionless (e.g. Navarro, Frenk & White 1996a). However, the complex dynamical interplay between stars, gas and DM during galaxy formation could erase such cusps leading to cored distributions (e.g. Navarro, Eke & Frenk 1996b; Read & Gilmore 2005; Mashchenko, Wadsley & Couchman 2008; Goerdt et al. 2010; Governato et al. 2010; Cole, Dehnen & Wilkinson 2011). Cores could also be an indication of other possibilities such as self-interacting DM (e.g. Hogan & Dalcanton 2000; Moore et al. 2000).

Knowledge of the inner slope of the DM profile is of critical importance as most of the annihilation flux comes from that region. Lacking this information, several studies have focused on the detectability of these dSphs by current γ-ray observatories such as the satellite-borne *Fermi*-Large Area Telescope (*Fermi*-LAT) and atmospheric Cherenkov telescopes (ACTs) such as the HESS, MAGIC and VERITAS, using a small sample of cusped and cored profiles (generally one of each). Most studies rely on standard core and cusp profiles fitted to the kinematic data of the dSph of interest (Bergström & Hooper 2006; Sánchez-Conde et al. 2007; Bringmann, Doro & Fornasa 2009; Pieri et al. 2009a; Pieri, Lattanzi & Silk 2009b). Other authors use a 'cosmological prior' from large-scale cosmological simulations (e.g. Kuhlen 2010). Both approaches may be combined, such as in Strigari et al. (2007b) and Martinez et al. (2009) who rely partially on the results of structure formation simulations to constrain the inner slope and then perform a fit to the data to derive the other parameters. However, such cosmological priors remain sufficiently uncertain that their use is inappropriate for guiding observational strategies. There have been only a few studies (e.g. Essig, Sehgal & Strigari 2009) which have *not* assumed strong priors for the DM profiles.

In this work, we revisit the question of the detectability of DM annihilation in the classical Milky Way dSphs, motivated by ambitious plans for next-generation ACTs such as the Cherenkov Telescope Array (CTA). We rely *solely* on published kinematic data to derive the properties of the dSphs, making minimal assumptions about the underlying DM distribution. Most importantly, we do not restrict our survey of DM profiles to those suggested by cosmological simulations. We also consider the effect of the spatial extent of the dSphs, which becomes important for nearby systems observed by background-limited instruments such as ACTs.

This paper extends the earlier study of Walker et al. (2011) which showed that there is a critical integration angle (twice the half-light radius divided by the dSph distance) where we can obtain a robust estimate of the J-factor (that parametrizes the expected γ-ray flux from a dSph, independently of the choice of DM particle model; see Section 2), regardless of the value of the central DM cusp slope γ. Here, we focus on the full radial dependence of the J-factor. We consider the effect of DM sublumps within the dSphs, discuss which dSphs are the best candidates for an observing programme, and examine the competitiveness of next-generation ACTs as DM probes.

This paper is organized as follows. In Section 2, we present a study of the annihilation γ-ray flux, focusing on which parameters critically affect the expected signal. In Section 3, we discuss the sensitivity of present/future γ-ray observatories. In Section 4, we present our method for the dynamical modelling of the observed kinematics of stars in dSphs. In Section 5, we derive DM density profiles for the classical dSphs using a Markov chain Monte Carlo (MCMC) analysis, from which the detection potential of future

γ-ray observatories can be assessed. We present our conclusions in Section 6.[1]

This paper includes detailed analyses from both high-energy astrophysics and stellar dynamical modelling. To assist readers from these different fields in navigating the key sections, we suggest that those who are primarily interested in the high-energy calculations may wish to focus their attention on Sections 2, 3 and 5 before moving to the conclusions. Readers from the dynamics community may instead prefer to read Sections 2, 4 and 5. Finally, those who are willing to trust the underlying modelling should proceed to Section 5 where our main results regarding the detectability of dSphs are presented in Figs 12, 15, 16 and 17 (shown later).

2 THE DARK MATTER ANNIHILATION SIGNAL: KEY PARAMETERS

2.1 The γ-ray flux

The γ-ray flux Φ_γ (photons cm^{-2} s^{-1} GeV^{-1}) from DM annihilation in a dSph, as seen within a solid angle $\Delta\Omega$, is given by (see Appendix A for definitions and conventions used in the literature)

$$\frac{\mathrm{d}\Phi_\gamma}{\mathrm{d}E_\gamma}(E_\gamma, \Delta\Omega) = \Phi^{\mathrm{pp}}(E_\gamma) \times J(\Delta\Omega)\,. \quad (1)$$

The first factor encodes the (unknown) particle physics of DM annihilation which we wish to measure. The second factor encodes the astrophysics *viz.* the line-of-sight (l.o.s.) integral of the DM density squared over solid angle $\Delta\Omega$ in the dSph – this is called the 'J-factor'. We now discuss each factor in turn.

2.1.1 *The particle physics factor*

The particle physics factor (Φ^{pp}) is given by

$$\Phi^{\mathrm{pp}}(E_\gamma) \equiv \frac{\mathrm{d}\Phi_\gamma}{\mathrm{d}E_\gamma} = \frac{1}{4\pi}\frac{\langle\sigma_{\mathrm{ann}}v\rangle}{2m_\chi^2} \times \frac{\mathrm{d}N_\gamma}{\mathrm{d}E_\gamma}\,, \quad (2)$$

where m_χ is the mass of the DM particle, σ_{ann} is its self-annihilation cross-section and $\langle\sigma_{\mathrm{ann}}v\rangle$ is the average over its velocity distribution, and $\mathrm{d}N_\gamma/\mathrm{d}E_\gamma$ is the differential photon yield per annihilation. A benchmark value is $\langle\sigma_{\mathrm{ann}}v\rangle \sim 3 \times 10^{-26}\,\mathrm{cm}^3\,\mathrm{s}^{-1}$ (Jungman, Kamionkowski & Griest 1996), which would result in a present-day DM abundance satisfying cosmological constraints.

Unlike the annihilation cross-section and particle mass, the differential annihilation spectrum [$\mathrm{d}N_\gamma/\mathrm{d}E_\gamma(E_\gamma)$] requires us to adopt a specific DM particle model. We focus on a well-motivated class of models that are within reach of upcoming direct and indirect experiments: the Minimal Supersymmetric Standard Model (MSSM). In this framework, the neutralino is typically the lightest stable particle and therefore one of the most favoured DM candidates (see e.g. Bertone, Hooper & Silk 2005). A γ-ray continuum is produced from the decay of hadrons (e.g. $\pi^0 \to \gamma\gamma$) resulting from the DM annihilation. Neutralino annihilation can also directly produce mono-energetic γ-ray lines through loop processes, with the formation of either a pair of γ-rays ($\chi\chi \to \gamma\gamma$; Bergström & Ullio 1997), or a Z^0 boson and a γ-ray ($\chi\chi \to \gamma Z^0$; Ullio & Bergström 1998). We do not take into account such line-production processes since they are usually subdominant and very model-dependent (Bringmann, Bergström & Edsjö 2008). The differential photon spectrum we use is restricted to the continuum contribution and is written as

$$\frac{\mathrm{d}N_\gamma}{\mathrm{d}E_\gamma}(E_\gamma) = \sum_i b_i \frac{\mathrm{d}N_\gamma^i}{\mathrm{d}E_\gamma}(E_\gamma, m_\chi)\,, \quad (3)$$

where the different annihilation final states i are characterized by a branching ratio b_i.

Using the parameters in Fornengo, Pieri & Scopel (2004), we plot the continuum spectra calculated for a 1-TeV mass neutralino in Fig. 1.

Apart from the $\tau^+\tau^-$ channel (dot–dashed line), all the annihilation channels in the continuum result in very similar spectra of γ-rays (dashed lines). For charged annihilation products, internal bremsstrahlung (IB) has recently been investigated and found to enhance the spectrum close to the kinematic cut-off (e.g. Bringmann et al. 2008). As an illustration, the long-dashed line in Fig. 1 corresponds to the benchmark configuration for a wino-like neutralino taken from Bringmann et al. (2008). However, the shape and amplitude of this spectrum are strongly model-dependent (Bringmann et al. 2009) and, as argued in Cannoni et al. (2010), this contribution is relevant only for models (and at energies) where the line contribution is dominant over the secondary photons.

We wish to be as model-independent as possible, and so do not consider IB. In the remainder of this paper, all our results will be based on an *average* spectrum taken from the parametrization

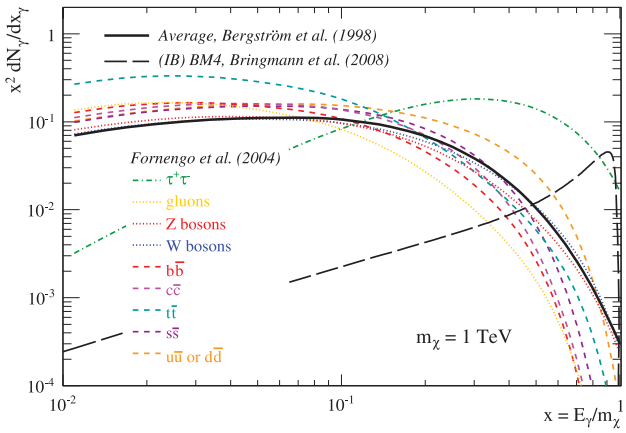

Figure 1. Differential spectra (multiplied by x^2) of γ-rays from the fragmentation of neutrino annihilation products (here for a DM particle mass of $m_\chi = 1$ TeV). Several different channels are shown, taken from Fornengo et al. (2004), and an average parametrization (Bergström et al. 1998) is marked by the black solid line; this is what we adopt throughout this paper. The black dashed line is the benchmark model BM4 (Bringmann et al. 2008) which includes IB and serves to illustrate that very different spectra are possible. However, the example shown here is dominated by line emission and therefore highly model-dependent; for this reason, we do not consider such effects in this paper.

[1] Technical details are deferred to appendices. In Appendix A, we comment on the various notations used in similar studies and provide conversion factors to help compare results. In Appendix B, we provide a toy model for quick estimates of the J-factor. In Appendix D, we calculate in a more systematic fashion the range of the possible 'boost factor' (due to DM clumps within the dSphs) for generic dSphs. In Appendix E, we show that convolving the signal by the point spread function (PSF) of the instrument is equivalent to a cruder quadrature sum approximation. In Appendix F, we discuss some technical issues related to confidence level (CL) determination from the MCMC analysis. In Appendix G, the reconstruction method is validated on simulated dSphs. In Appendix H, we discuss the impact of the choice of the binning of the stars and of the shape of the light profile on the J-factor determination.

(Bergström et al. 1998; solid line in Fig. 1):

$$\frac{\mathrm{d}N_\gamma}{\mathrm{d}E_\gamma} = \frac{1}{m_\chi}\frac{\mathrm{d}N_\gamma}{\mathrm{d}x} = \frac{1}{m_\chi}\frac{0.73\mathrm{e}^{-7.8x}}{x^{1.5}}, \quad (4)$$

with $x \equiv E_\gamma/m_\chi$. Finally, in order to be conservative in deriving detection limits, we also do not consider the possible 'Sommerfeld enhancement' of the DM annihilation cross-section (Hisano, Matsumoto & Nojiri 2004; Hisano et al. 2005).[2] This depends inversely on the DM particle velocity, and thus requires precise modelling of the velocity distribution of the DM within the dSph; we will investigate this in a separate study.

2.1.2 The J-factor

The second term in equation (1) is the astrophysical *J-factor* which depends on the spatial distribution of DM as well as on the beam size. It corresponds to the l.o.s. integration of the DM density squared over solid angle $\Delta\Omega$ in the dSph:

$$J = \int_{\Delta\Omega}\int \rho^2_{\mathrm{DM}}(l,\Omega)\mathrm{d}l\mathrm{d}\Omega. \quad (5)$$

The solid angle is simply related to the integration angle α_{int} by

$$\Delta\Omega = 2\pi[1-\cos(\alpha_{\mathrm{int}})].$$

The J-factor is useful because it allows us to rank the dSphs by their expected γ-ray flux, independently of any assumed DM particle physics model. Moreover, the knowledge of the relative J-factors would also help us to evaluate the validity of any potential detection of a given dSph, because for a given particle physics model, we could then scale the signal to what we should expect to see in the other dSphs.

All calculations of J presented in this paper were performed using the publicly available CLUMPY package (Charbonnier, Combet & Maurin, 2011) which includes models for a smooth DM density profile for the dSph, clumpy DM substructures inside the dSph, and a smooth and clumpy Galactic DM distribution.[3]

2.1.3 DM profiles

For the DM halo, we use a generalized (α, β, γ) Hernquist profile given by (Hernquist 1990; Dehnen 1993; Zhao 1996)

$$\rho(r) = \rho_{\mathrm{s}}\left(\frac{r}{r_{\mathrm{s}}}\right)^{-\gamma}\left[1+\left(\frac{r}{r_{\mathrm{s}}}\right)^{\alpha}\right]^{\frac{\gamma-\beta}{\alpha}}, \quad (6)$$

where the parameter α controls the sharpness of the transition from inner slope, $\lim_{r\to 0}\mathrm{dln}(\rho)/\mathrm{dln}(r) = -\gamma$, to outer slope $\lim_{r\to\infty}\mathrm{dln}(\rho)/\mathrm{d}\ln(r) = -\beta$, and r_{s} is a characteristic scale. In principle, we could add an additional parameter in order to introduce an exponential cut-off in the profile of equation (6) to mimic the effects of tidal truncation, as proposed in, for example, the Aquarius (Springel et al. 2008) or Via Lactea II (Diemand et al. 2008) simulations. However, the freedom to vary the parameters r_{s}, α and β in equation (6) already allows for density profiles that fall arbitrarily steeply at large radius. Moreover, given that our MCMC analysis later shows that the outer slope β is unconstrained by the available data and that the J-factor does not correlate with β, we choose not to add further shape parameters.

For profiles such as $\gamma \geq 1.5$, the quantity J from the inner regions diverges. This can be avoided by introducing a saturation scale r_{sat} that corresponds physically to the typical scale where the annihilation rate $[\langle\sigma v\rangle\rho(r_{\mathrm{sat}})/m_\chi]^{-1}$ balances the gravitational infall rate of DM particles $(G\bar{\rho})^{-1/2}$ (Berezinsky, Gurevich & Zybin 1992). Taking $\bar{\rho}$ to be about 200 times the critical density gives

$$\rho_{\mathrm{sat}} \approx 3\times 10^{18}\left(\frac{m_\chi}{100\,\mathrm{GeV}}\right)\times\left(\frac{10^{-26}\,\mathrm{cm^3\,s^{-1}}}{\langle\sigma v\rangle}\right)\mathrm{M_\odot\,kpc^{-3}}. \quad (7)$$

The associated saturation radius is given by

$$r_{\mathrm{sat}} = r_{\mathrm{s}}\left(\frac{\rho_{\mathrm{s}}}{\rho_{\mathrm{sat}}}\right)^{1/\gamma} \ll r_{\mathrm{s}}. \quad (8)$$

This limit is used for all of our calculations.

2.2 Motivation for a generic approach and reference models

In many studies, the γ-ray flux (from DM annihilation) is calculated using the point-source approximation (e.g. Bergström & Hooper 2006; Kuhlen 2010). This is valid so long as the inner profile is steep, in which case the total luminosity of the dSph is dominated by a very small central region. However, if the profile is shallow and/or the dSph is nearby, the effective size of the dSph on the sky is larger than the PSF of the detector, and the point-source approximation breaks down. For upcoming instruments and particularly shallow DM profiles, the effective size of the dSph may even be comparable to the field of view of the instrument. This difference in the radial extent of the signal does matter in terms of detection (see Section 3). Hence, we do not assume that the dSph is a point source but rather derive sky maps for the expected γ-ray flux.

2.2.1 Illustration: a cored versus cusped profile

Fig. 2 shows J as a function of the integration angle α_{int} for a dSph at 20 kpc (looking towards its centre). The black solid line is for a cored profile ($\gamma = 0$) and the green dashed line is for a cuspy profile ($\gamma = 1.5$); both are normalized to unity at $\alpha_{\mathrm{int}} = 5^\circ$. For the cuspy profile, ∼100 per cent of the signal is in the first bin, while for the cored profile, J builds up slowly with α_{int}, and 80 per cent

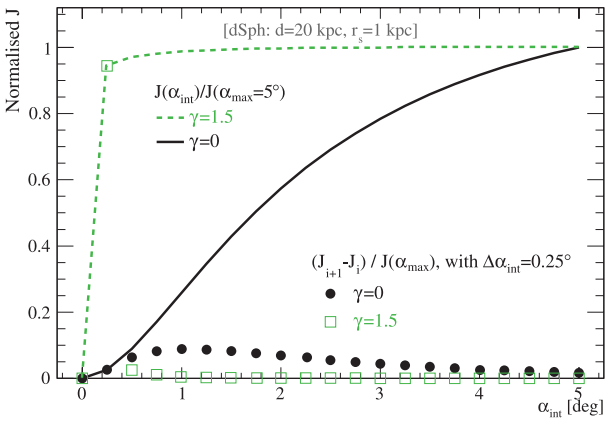

Figure 2. Finite size effects: J as a function of the integration angle α_{int} for a dSph at 20 kpc (pointing towards the centre of the dSph). The black solid line is for a cored profile ($\gamma = 0$) and the green dashed line is for a cuspy profile ($\gamma = 1.5$); both are normalized to unity at $\alpha_{\mathrm{int}} = 5^\circ$.

[2] This effect depends on the mass and the velocity of the particle; the resulting boost of the signal and the impact on detectability of the dSphs has been discussed, for example, in Pieri et al. (2009b).

[3] In Appendix B, we provide approximate formulae for quick estimates of the J-factor and cross-checks with the numerical results.

Table 1. The required normalization ρ_s to have $M_{300} = 10^7 M_\odot$ for a sample of (1, 3, γ) profiles with varying scale radius r_s.

	ρ_s (10^7 M$_\odot$ kpc^{-3})		
γ/r_s (kpc)	0.10	0.50	1.0
0.00	224	25.8	16.02
0.25	196	18.6	10.22
0.50	170	13.4	6.47
0.75	146	9.5	4.06
1.00	125	6.7	2.52
1.25	106	4.7	1.54
1.50	88	3.2	0.92

of the signal (with respect to the value for $\alpha_{\rm int} = 5^\circ$) is obtained for $\alpha^{80\,\rm per\,cent} \approx 3^\circ$. This is also indicated by the symbols which show the contribution of DM *shells* in two angular bins – whereas the (green) hollow squares have a spiky distribution in the first bin ($\gamma = 1.5$), the (black) filled circles ($\gamma = 0$) show a very broad distribution for J.

The integration angle required to have a sizeable fraction of the signal depends on several parameters: the distance d from the dSph, the inner profile slope γ and the scale radius r_s. Small integration angles are desirable since this minimizes contaminating background γ-ray photons and maximizes the signal-to-noise ratio. Thus, the true detectability of a dSph will depend on its spatial extent on the sky, and thus also on d, γ and r_s.

2.2.2 Generic dSph profiles

As will be seen in Section 5, the errors on the density profiles of the Milky Way dSphs are large, making it difficult to disentangle the interplay between the key parameters for detectability. Hence, we select some 'generic profiles' to illustrate the key dependencies.

The most constrained quantity is the mass within the half-light radius r_h (typically a few tenths of a kpc), as this is where most of the kinematic data come from (e.g. W09; Wolf et al. 2010). For the classical Milky Way dSphs, the typical mass within $r_h \sim 300$ pc is found to be $M_{300} \sim 10^7\,M_\odot$ (Strigari et al. 2008, see also the bottom panel of Fig. 13 shown later). If the DM scale radius is significantly larger than this ($r_s \gg r_h$) and the inner slope $\gamma \gtrsim 0.5$, we can approximate the enclosed mass by

$$M_{300} \simeq \frac{4\pi\rho_s r_s^3}{3-\gamma}\left(\frac{300\,\rm pc}{r_s}\right)^{3-\gamma} \approx 10^7\,M_\odot\,. \quad (9)$$

The parameter ρ_s is thus determined completely by the above condition, if we choose the scale radius r_s and cusp slope γ.

Table 1 shows, for several values of r_s and γ, the value required for ρ_s to obtain the assumed M_{300} mass. We fix $\alpha = 1$, $\beta = 3$ but our results are not sensitive to these choices.[4] The values of r_s are chosen to encompass the range of r_s found in the MCMC analysis (see Section 5). To further convince ourselves that the generic profiles we present here are a possible description of real dSphs, we checked (not shown) using typical stellar profiles and properties of these objects (i.e. half-light radius of a few 100 pc) that a flat $\sim$10 km s^{-1} velocity dispersion profile within the error bars is recovered. We also study below the effect of moving these dSphs from a distance of 10 kpc to 300 kpc, corresponding to the typical range covered by these objects.

2.2.3 Substructures within the dSph

Structure formation simulations in the currently favoured ΛCDM (cold DM plus a cosmological constant) cosmology find that DM haloes are self-similar, containing a wealth of smaller 'substructure' haloes down to Earth-mass haloes (e.g. Diemand, Moore & Stadel 2005). However, as emphasized in the introduction, such simulations typically neglect the influence of the baryonic matter during galaxy formation. It is not clear what effect these have on the DM substructure distribution. For this reason, we adopt a more generic approach. We assess the importance of clumps using the following recipe[5]:

(i) we take a fraction $f = 20$ per cent of DM mass in the form of clumps;

(ii) the spatial distribution of clumps follows the smooth one;

(iii) the clump profiles are calculated *à la*Bullock et al. (2001) (hereinafter B01), that is, an 'NFW' profile (Navarro et al. 1996a) with concentration related to the mass of the clumps;

(iv) the clump mass distribution is $\propto M^{-a}$ ($a = -1.9$), within a mass range $M_{\rm min}$–$M_{\rm max} = [10^{-6}$–$10^6]\,M_\odot$.

Although these parameters are very uncertain, they allow us to investigate the impact of subtructures on the J-factor. They are varied within reasonable bounds in Section 2.3.2 (and Appendix D) to determine whether the subclump contribution can boost the signal. Note that a 20 per cent clump mass fraction is about twice as large as the fraction obtained from numerical simulations (see e.g. Springel et al. 2008). This generous fraction does not affect our conclusions, as discussed below.

2.3 $J_{\rm sm}$ and $J_{\rm subcl}$ for the generic models

As an illustration, we show in Fig. 3 one realization of the 2D distribution of J from a generic core profile ($\gamma = 0$) with $r_s = 1$ kpc (subclump parameters are as described in Section 2.2.3). The dSph is at $d = 100$ kpc. We note that our consideration of a $\gamma = 0$ smooth component with NFW subclumps is plausible if, for example, baryon-dynamical processes erase cusps in the smooth halo but cannot do so in the sub-subhaloes. The total J is the sum of the smooth and subclump distributions. The centre is dominated by the smooth component, whereas some graininess appears in the outskirts of the dSph.

In this particular configuration, the 'extended' signal from the core profile, when integrated over a very small solid angle, could be subdominant compared with the signal of NFW subclumps that it hosts. The discussion of cross-constraints between detectability of subhaloes of the Galaxy versus subclumps in the dSph is left for a future study.

In the remainder of this paper, we will replace for simplicity the calculation of $J_{\rm subcl}(\alpha_{\rm int})$ by its mean value, as we are primarily interested in 'unresolved' observations. Hence, clumps are not drawn from their distribution function, but rather $\langle J_{\rm subcl}\rangle$ is calculated from

[4] For a different mass for the dSph, the results for J below have to be rescaled by a factor $(M_{300}^{\rm new}/10^7\,M_\odot)^2$ since the density is proportional to M_{300}, while J goes as the density squared.

[5] More details about the clump distributions can be found in Appendix B2. See also, for example, Section 2 in Lavalle et al. (2008) and references therein, as we use the same definitions as those given in that paper.

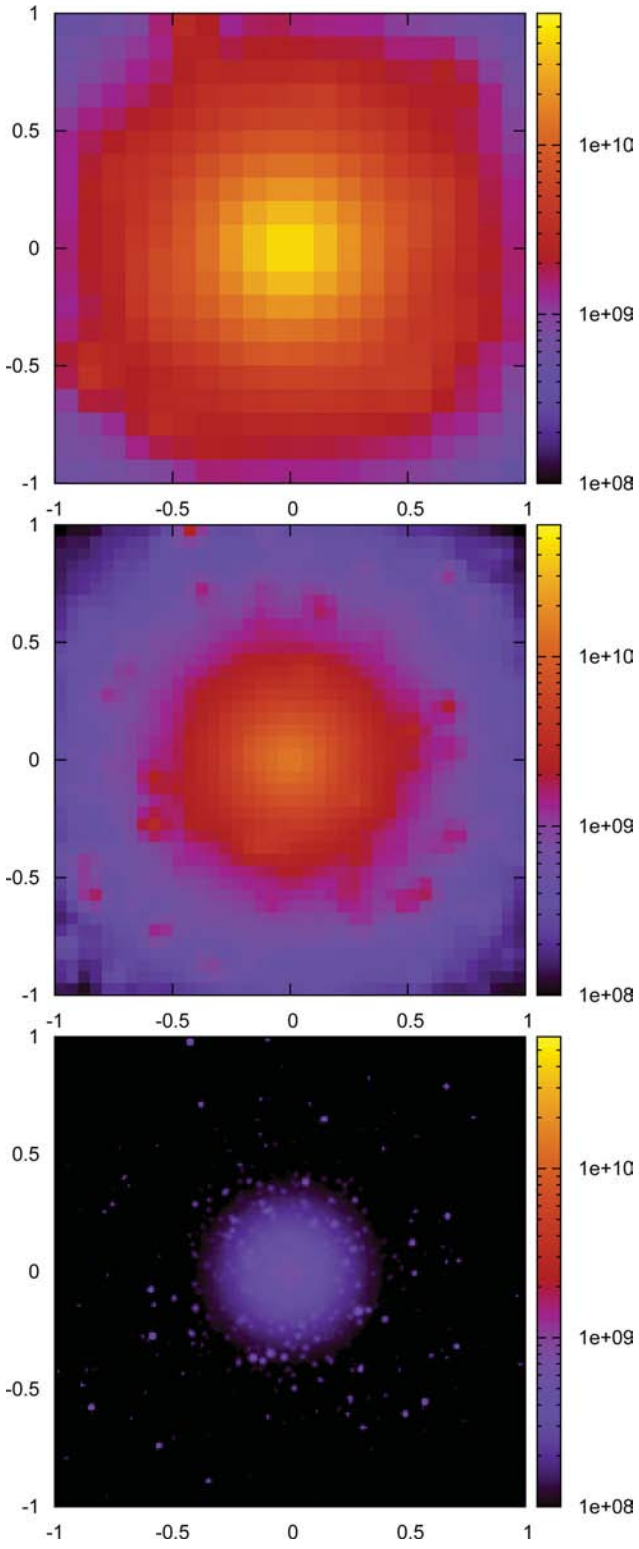

Figure 3. Two-dimensional view (x- and y-axes are in degrees) of J for the generic dSph with $\gamma = 0$ and $r_s = 1$ kpc at $d = 100$ kpc ($M_{300} = 10^7\,M_\odot$). The subclumps are drawn from the reference model described in Section 2.2.3, that is, $f = 20$ per cent, subclump distribution follows smooth, and subclump inner profiles have NFW with B01 concentration. From the top to bottom panel: $\alpha_{\rm int} = 0.^\circ1$, $0.^\circ05$ and $0.^\circ01$. For the sake of comparison, the same colour scale is taken for the three integration angles (J is in units of $M_\odot^2$ kpc^{-5}).

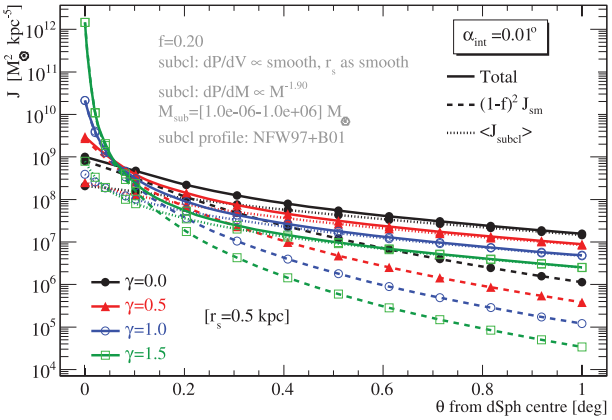

Figure 4. J as a function of the angle θ away from the dSph centre for a dSph at 100 kpc with $r_s = 0.5$ kpc (ρ_s is given in Table 1). The integration angle $\alpha_{\rm int} = 0.^\circ01$. For the four inner slope values γ, the various contributions to J are shown as the solid (total), dashed (smooth) and dotted lines (subclumps).

the integration of the spatial and luminosity (as a function of mass) distributions (see Appendix B2).

2.3.1 *Radial dependence of $J(\theta)$*

The radial dependence of J is shown in Fig. 4 for four values of γ (for an integration angle $\alpha_{\rm int} = 0.^\circ01$). The dashed lines show the result for the smooth distribution, the dotted lines show the subclump contribution, and the solid lines are the sum of the two. The peak of the signal is towards the dSph centre. As long as the distribution of clumps is assumed to follow the smooth one, regardless of the value of γ, the quantity $(1-f)^2 J_{\rm sm}(0)$ always dominates (at least by a factor of a few) over $\langle J_{\rm subcl}(0)\rangle$. (Recall that in our generic models, all dSphs have the same M_{300}.) The scatter in $J_{\rm tot}(0)$ is about four orders of magnitude for $\gamma \in [0.0\text{–}1.5]$, but only a factor of 20 for $\gamma \in [0.0\text{–}1.0]$. Beyond a few tenths of degrees, $\langle J_{\rm subcl}\rangle$ dominates. The crossing point depends on a combination of the clump mass fraction f, γ, r_s, d and $\alpha_{\rm int}$. The dependence of J on the two latter parameters are discussed in Appendix C. The radial dependence is as expected: the smooth contribution decreases faster than that of the subclump one, because the signal is proportional to the squared spatial distribution in the first case, but directly proportional to the spatial distribution in the second case. Halving f to match the fraction from N-body simulations would have a 25 per cent effect on $(1-f)^2 J_{\rm sm}$, but decreases $J_{\rm subcl}$ by a factor of 4, so that the cross-over between the two components would occur at a larger angle (Fig. 4).

2.3.2 *Boost factor*

Whether or not the signal is boosted by the subclump population is still debated in the literature (Strigari et al. 2007b; Kuhlen, Diemand & Madau 2008; Pieri, Bertone & Branchini 2008; Pieri et al. 2009a). As underlined in the previous sections, the subclump contribution towards the dSph centre never dominates over the smooth one if the spatial profile of the subclumps follows that of the smooth distribution, and if the integration angle remains below some critical angle discussed below.

Let us first define properly the parameters with respect to which this boost is calculated, as there is sometimes some confusion about this. Here, we define it with respect to the integration angle $\alpha_{\rm int}$ (the

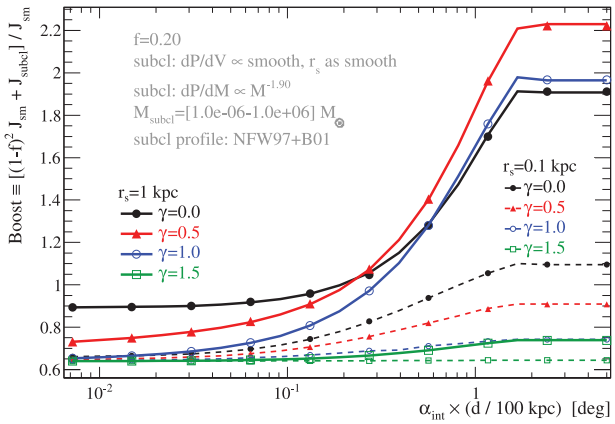

Figure 5. Boost factor as a function of $\alpha_{\rm int} \times (d/100\ {\rm kpc})$ for different inner slopes γ and with subclumps following the smooth profile (see Section 2.2.3): the dSph is at $d = 100$ kpc (lines) or $d = 10$ kpc (symbols).

pointing direction is still towards the dSph centre):

$$B(\alpha_{\rm int}) \equiv \frac{(1-f)^2 J_{\rm sm}(\alpha_{\rm int}) + J_{\rm subcl}(\alpha_{\rm int})}{J_{\rm sm}(\alpha_{\rm int})}\,. \tag{10}$$

In most studies, the boost has been calculated by integrating out to the clump boundary (i.e. $\alpha_{\rm int}^{\rm all} = R_{\rm vir}/d$). However, the boost depends crucially on $\alpha_{\rm int}$ (the radial dependence of the smooth and subclump contributions differs, see Section 2.3.1).

We plot in Fig. 5 the boost for different inner slopes γ, where a direct consequence of equation (C7) is the $\alpha_{\rm int} \times d$ rescaling. For $r_{\rm s} \lesssim 0.1$ kpc (regardless of γ), or for $\gamma \gtrsim 1.5$ (regardless of $r_{\rm s}$), the signal is never boosted.[6] For small enough $\alpha_{\rm int}$, B is smaller than unity, and if γ is steep enough, $B \approx (1-f)^2$. For large values, a plateau is reached as soon as $\alpha_{\rm int} d \gtrsim R_{\rm vir}$ (taken to be 3 kpc here). In between, the value of the boost depends on $r_{\rm s}$ and γ of the smooth component. Going beyond this qualitative description is difficult, as the toy-model formulae of Appendix B2 give results correct to only a factor of ∼2 (which is inadequate to evaluate the boost properly).

To conclude, the maximum value for subclump *follows* smooth is $\lesssim$2, and this value is reached only when integrating the signal out to $R_{\rm vir}/d$. The boost could still be increased by varying the subclump properties (e.g. taking a higher concentration). Conversely, if dynamical friction has caused the subclump population to become much more centrally concentrated than the smooth component, then the boost is decreased. This is detailed in Appendix D. For the most realistic configurations, there is *no* significant boost when a clump mass fraction $f = 20$ per cent is used. Naturally, this result is even more true for the smaller f found in N-body simulations so we disregard the boost for the rest of this paper and consider only the smooth contribution.

[6] The difference between the level of boost observed for $r_{\rm s} = 0.1$ and 1 kpc can be understood if we recall that the total mass of the clump is fixed to 300 pc, regardless of the value of γ or $r_{\rm s}$. For $r_{\rm s} = 0.1$ kpc, $\rho_{\rm s} \sim \mathcal{O}(10^9\,{\rm M}_\odot\,{\rm kpc}^{-3})$, whereas for $r_{\rm s} = 1$ kpc, $\rho_{\rm s} \sim \mathcal{O}(10^7\,{\rm M}_\odot\,{\rm kpc}^{-3})$. As $J_{\rm sm} \propto \rho_{\rm s}^2$ whereas $J_{\rm sub} \propto \rho_{\rm s}$, the relative amount of $J_{\rm sub}$ with respect to $J_{\rm sm}$ is expected to decrease with smaller $r_{\rm s}$. This is indeed what we observe in the figure (solid versus dashed lines).

3 SENSITIVITY OF PRESENT/FUTURE γ-RAY OBSERVATORIES

Major new ground-based γ-ray observatories are in the planning stage, with the CTA (CTA Consortium 2010) and AGIS (AGIS Collaboration 2010) as the main concepts. As the designs of these instruments are still evolving, we adopt here generic performance curves (described below), close to the stated goals of these projects. For the LAT of the *Fermi* γ-ray satellite, the performance for 1-year observations of point-like, high-Galactic-latitude sources is known (Fermi-LAT Collaboration 2010), but no information is yet available for longer exposures or for extended objects. We therefore adopt a toy likelihood-based model for the *Fermi* sensitivity, tuned to reproduce the 1-year point-source curves. We note that whilst this approach results in approximate performance curves for both the ground- and the space-based instruments, it captures the key differences (in particular, the differences in collection area and angular resolution) and illustrates the advantages and limitations of the two instrument types, as well as the prospects for the discovery of DM annihilation in dSphs within the next decade.

3.1 Detector models

The sensitivity of a major future γ-ray observatory based on an array of Cherenkov telescopes (FCA in the following, for 'Future Cherenkov Array') is approximated based on the point-source differential sensitivity curve (for a 5σ detection in 50 hours of observations) presented by Bernlöhr et al. (2008). Under the assumption that the angular resolution of such a detector is a factor of 2 better than the HESS (Funk et al. 2008) and has the same energy dependence, and that the effective collection area for γ-rays grows from 10^4 m^2 at 30 GeV to 1 km^2 at 1 TeV, the implied cosmic-ray (hadron and electron) background rate per deg^2 can be inferred and the sensitivity thus adapted to different observation times, spectral shapes and source extensions. Given that the design of instruments such as the CTA is not yet fixed, we consider that such a simplified response, characterized by the following functions, is a useful tool to explore the capabilities of a generic next-generation instrument:

$$\mathrm{LS} = -13.1 - 0.33X + 0.72X^2, \tag{11}$$

$$\mathrm{LA} = 6 + 0.46X - 0.56X^2, \tag{12}$$

$$\psi_{68} = 0.038 + \exp -(X + 2.9)/0.61, \tag{13}$$

where

$$X = \log_{10}(\text{photon energy/TeV}), \tag{14}$$

LS = $\log_{10}$(differential sensitivity/erg cm^{-2} s^{-1}), LA = $\log_{10}$(effective area/m^2), and ψ_{68} is the 68 per cent containment radius of the PSF in degrees.

For the *Fermi* detector, a similar simplified approach is taken; the numbers used below are those provided by Fermi-LAT Collaboration (2010). The effective area changes as a function of energy and the incident angle to the detector, reaching a maximum of ≈8000 cm^2. The effective time-averaged area is then $\epsilon A\Omega/4\pi$ and the data-taking efficiency $\epsilon \approx 0.8$ (due to instrument dead-time and passages through the South Atlantic Anomaly). The PSF again varies as a function of energy (with a much smaller dependence as a function of incidence angle), from 10° to a few tenths of a degree over the LAT energy range. A rate of 1.5×10^{-5} cm^{-2} s^{-1} sr^{-1} (>100 MeV) and a photon index of 2.1 are assumed for the background. The sensitivity is then estimated using a simplified likelihood method which provides results within 20 per cent of the

sensitivity for a 1-year observation of a point-like source given by Fermi-LAT Collaboration (2010).

Whilst both detector responses are approximate, the comparison is still useful. Our work incorporates several key aspects not considered in earlier studies, including the strong energy dependence of the angular resolution of both ground- and space-based instruments in the relevant energy range of 1 GeV to 1 TeV and hence the energy-dependent impact of the angular size of the target region.

3.2 Relative performance for generic haloes

Using the results from Section 2.2.2 and the detector performance models defined above, we can begin to investigate the sensitivity of future ACT arrays and the *Fermi*-LAT detector (over long observation times) to DM annihilation in dSphs. The detectability of a source depends primarily not only on its flux, but also on its angular extent. The impact of source extension on detectability is dealt with approximately (in each energy bin independently) by assuming that the opening angle of a cone which incorporates 80 per cent of the signal is given by

$$\theta_{80} = \sqrt{\psi_{80}^2 + \alpha_{80}^2}\,, \tag{15}$$

where $\psi_{80} = 1.25\psi_{68}$ is assumed for the FCA and interpolated from values given for 68 and 95 per cent containment for the LAT (Fermi-LAT Collaboration 2010); here, α_{80} is the 80 per cent containment angle of the halo emission. The validity of this approximation (at the level of a few per cent) has been tested (see Appendix E) by convolving realistic halo profiles with a double Gaussian PSF as found for the HESS (Horns 2005). An 80 per cent integration circle is close to optimum for a Gaussian source on a flat background (in the background-limited regime). Fig. 6 shows the 80 per cent containment radius of the annihilation flux of generic haloes as a function of the inner slope γ. This result can be parametrized as

$$\alpha_{80} = 0.^{\circ}8(1 - 0.48\gamma - 0.137\gamma^2)\left(\frac{r_{\rm s}}{1\,{\rm kpc}}\right)\left(\frac{d}{100\,{\rm kpc}}\right)^{-1}. \tag{16}$$

It is clear that for a broad range of d, γ and $r_{\rm s}$, the characteristic angular size of the emission region is *larger* than the angular resolution of the instruments under consideration. It is therefore critical to assess the performance as a function of the angular size of the dSph as well as the mass of the annihilating particle.

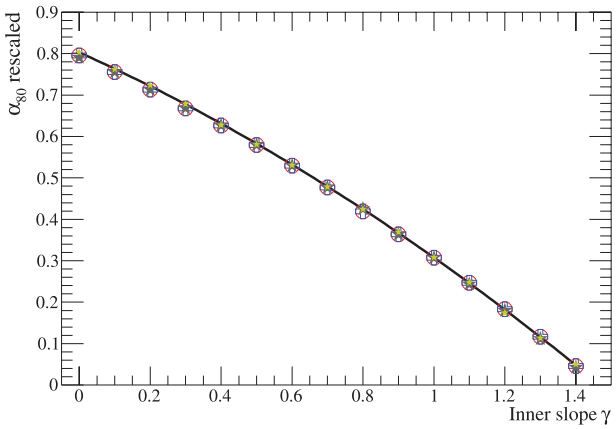

Figure 6. The cone angle encompassing 80 per cent of the annihilation flux as a function of the inner slope γ. Several different values of $r_{\rm s}$ and distance d are shown for each γ, all scaled by 1 kpc/$r_{\rm s}$ and 100 kpc/d. The best-fitting curve is also shown, corresponding to equation (16).

Fig. 7 shows the relative sensitivity of *Fermi* and an FCA within our framework as a function of the mass of the annihilating particle, adopting the annihilation spectrum given in equation (4), with the several panels illustrating different points. From Fig. 7 (top panel, the case of a point-like signal for different observation times), it is clear that the *Fermi*-LAT has a considerable advantage for lower mass DM particles ($m_\chi \ll 1$ TeV) on the time-scale for construction of an FCA (i.e. over a 5–10 yr mission lifetime) in comparison to a deep ACT observation of 200 h. Furthermore, the *Fermi*-LAT is less adversely affected by the angular extent of the target regions (see Fig. 7, bottom panel), due to its modest angular resolution in the energy range where it is limited by background, meaning that the source extension is well matched to the PSF of the instrument. The middle panel of this figure illustrates the impact of different approaches to the analysis. In the case that there is a DM candidate inferred from the discovery of supersymmetry at the Large Hadron Collider (LHC) (quite possible on the relevant time-scale), a search optimized on an assumed mass and spectral shape can be made (solid curves). However, all instruments are less sensitive when a generic search is undertaken. Simple analyses using all the photon flux above a fixed energy threshold (arbitrarily set to reduce background) are effective only in a relatively narrow range of particle mass. For example, keeping only >100 GeV photons works well for ACTs for 0.3–3 TeV particles, whereas keeping all photons >1 GeV works moderately well in the 0.1–0.2 TeV range, but is much less sensitive than the higher threshold cut over the rest of the candidate DM particle mass range. The features of these curves are dictated by the expected shape of the annihilation spectrum. From equation (4), the peak photon output (adopting the average spectrum for DM annihilation) occurs at an energy which is an order of magnitude below the particle mass – effective detection requires that this peak occurs within (or close to) the energy range of the instrument concerned.

The total annihilation flux from a dSph increases at smaller distances as $1/d^2$ for fixed halo mass, making nearby dSphs attractive for DM detection. However, as Fig. 7 shows, the increased angular size of such nearby sources raises the required detection flux. Fig. 8 illustrates the reduction of an FCA sensitivity as a function of the distance of a generic dSph. Inner slopes $\gamma = 0$ and $\gamma = 1$ have been considered and $r_{\rm s}$ is fixed to 1 kpc. The sensitivity is expressed relative to that obtained using the full annihilation signal in the point-like approximation. Even for $\gamma = 1$, the point-like approximation leads to an order of magnitude overestimate of the detection sensitivity for nearby (∼20 kpc) dSphs. A further complication is how to establish the level of background emission arising from the residual non-γ-ray background. A common method in ground-based γ-ray astronomy is to estimate this background from an annulus around the target source (see e.g. Berge, Funk & Hinton 2007). The dashed lines in Fig. 8 show the impact of estimating the background using an annulus between 3.°5 and 4.°0 from the target. This approach has a modest impact on sensitivity and is ignored in the following discussions as it reduces both the detectable flux and θ_{80} and leads to a small improvement in some cases only.

4 JEANS/MCMC ANALYSIS OF DSPH KINEMATICS

4.1 dSph kinematics with the spherical Jeans equation

Extensive kinematic surveys of the stellar components of dSphs have shown that these systems have negligible rotational support

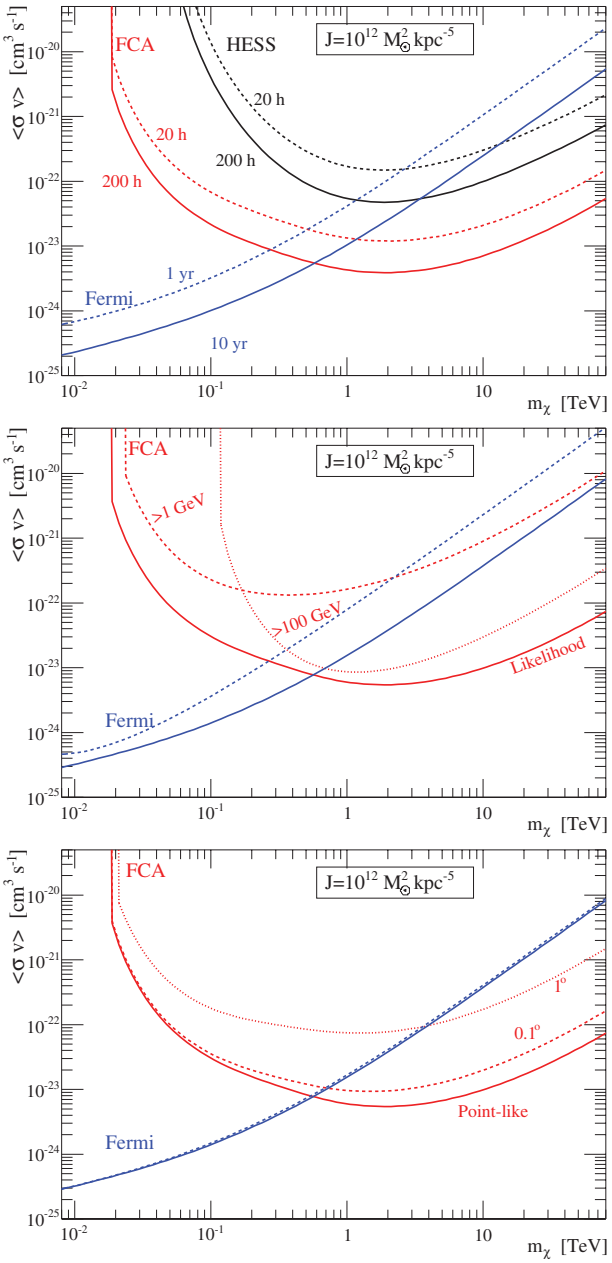

Figure 7. Approximate sensitivities of the *Fermi*-LAT (blue lines), HESS (black lines) and the FCA described above (red lines) to a generic halo with $J = 10^{12}\,\mathrm{M}_\odot^2\,\mathrm{kpc}^{-5}$, as a function of the mass of the annihilating particle and for the annihilation spectrum of equation (4). Top panel: the impact of observation time is illustrated: dashed lines give the 1-year and 20-hour sensitivities for *Fermi* and the FCA/HESS, respectively, while the solid lines refer to 10-year (200-hour) observations. Middle panel: the impact of analysis methods is considered for 5-year (100-hour) observations using *Fermi* (FCA). The solid lines show likelihood analyses in which the mass and spectrum of the annihilating particle are known in advance, while the dashed and dotted lines show simple integral flux measurements above fixed thresholds of 1 and 100 GeV, respectively. Note that the 1-GeV cut implies accepting all events for the FCA (where the trigger threshold is ≈20 GeV). Bottom panel: the impact of the angular extension of target sources, as given by the halo profile in Fig. 6, is illustrated. The solid lines reproduce the likelihood case from the middle panel for a point-like source, with the values of α_{80} of 0.°1 (dashed) and 1° also shown.

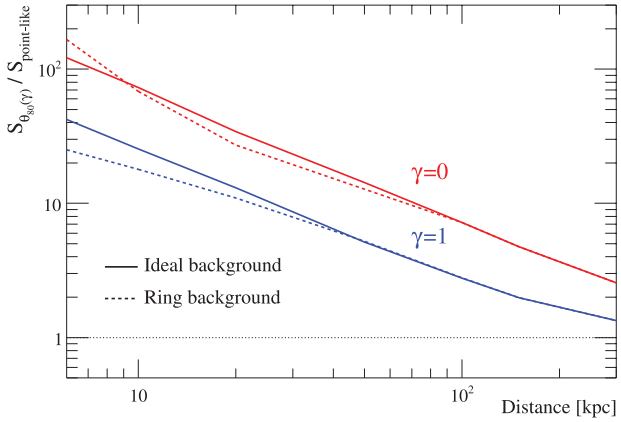

Figure 8. Relative DM annihilation detection sensitivity for a 100-hour FCA observation, as a function of dSph distance for different inner slopes γ and with r_s fixed to 1 kpc. The sensitivity for a realistic approach using θ_{80} is given relative to the sensitivity to a point-like source with the same flux. Larger values correspond to poorer performance (larger values of the minimum detectable flux). The assumed spectral shape is again as given by equation (4) with $m_\chi = 300$ GeV. This sensitivity ratio depends on the strategy used to estimate the background level at the dSph position. The dashed lines show the impact of using an annulus between 3.°5 and 4.°0 of the dSph centre as a background control region. The solid line assumes that the background control region lies completely outside the region of emission from the dSph.

(with the possible exception of the Sculptor dSph, see Battaglia et al. 2008). If we assume that the dSphs are in virial equilibrium, then their internal gravitational potentials balance the random motions of their stars. In order to estimate dSph masses, we consider here the behaviour of dSph stellar velocity dispersion as a function of distance from the dSph centre (analogous to rotation curves of spiral galaxies). Specifically, we use the stellar kinematic data of Walker, Mateo & Olszewski (2009c) for the Carina, Fornax, Sculptor and Sextans dSphs, the data of Mateo, Olszewski & Walker (2008) for the Leo I dSph, and data from Mateo et al. (in preparation) for the Draco, Leo II and Ursa Minor dSphs. W09 have calculated velocity dispersion profiles from these same data under the assumption that l.o.s. velocity distributions are Gaussian. Here we re-calculate these profiles without adopting any particular form for the velocity distributions. Specifically, for a given dSph, we divide the velocity sample into circular bins containing approximately equal numbers of member stars,[7] and within each bin, we estimate the second velocity moment (squared velocity dispersion) as

$$\langle \hat{V}^2 \rangle = \frac{1}{N-1} \sum_{i=1}^{N} [(V_i - \langle \hat{V} \rangle)^2 - \sigma_i^2], \qquad (17)$$

where N is the number of member stars in the bin. We hold $\langle V \rangle$ fixed for all bins at the median velocity over the entire sample. For each bin, we use a standard bootstrap re-sampling to estimate the associated error distribution for $\langle \hat{V}^2 \rangle$, which is approximately Gaussian. Fig. 9 displays the resulting velocity dispersion profiles, $\langle \hat{V}^2 \rangle^{1/2}(R)$, which are similar to previously published profiles.

In order to relate these velocity dispersion profiles to dSph masses, we follow W09 in assuming that the data sample in each

[7] Kinematic samples are often contaminated by interlopers from the Milky Way foreground. Following W09, we discard all stars for which the algorithm described by Walker et al. (2009b) returns a membership probability less than 0.95.

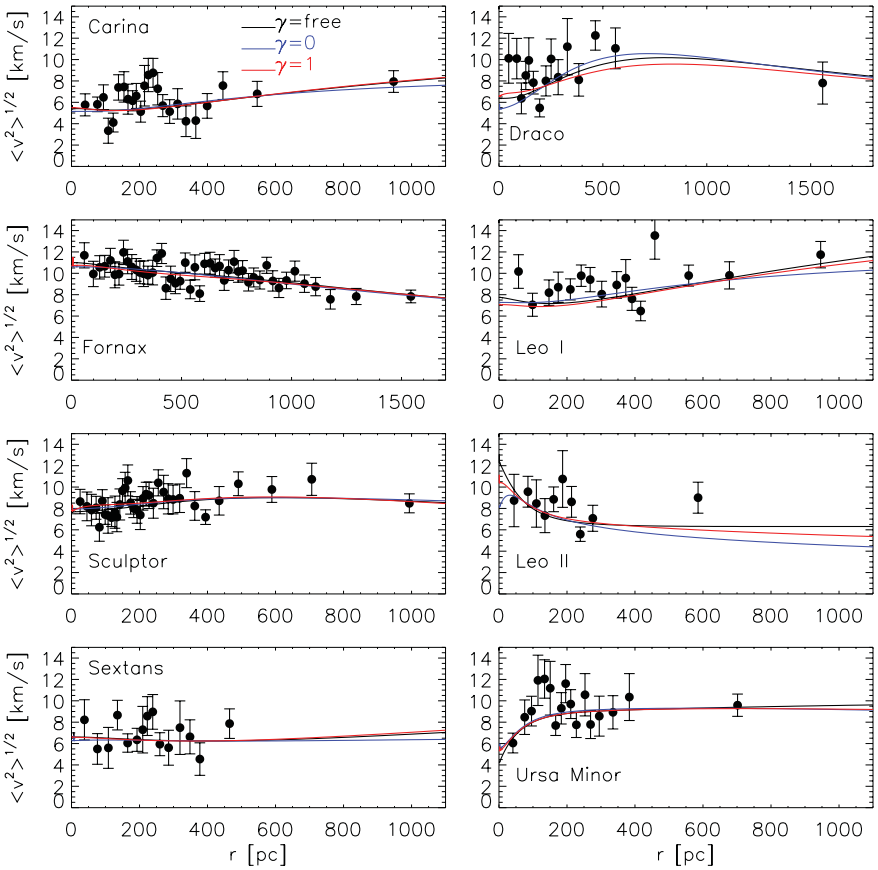

Figure 9. Velocity dispersion profile data for the eight classical dSphs, obtained as described in the text (the impact of the binning choice is discussed in Appendix H1). The solid lines correspond to the best-fitting models for the inner slope when γ is left free (dark), γ is fixed to 1 (blue) and γ is fixed to 0 (red). Because of the large degeneracies among the halo parameters (see Section 5.1 for a list), we do not list the corresponding best-fitting parameters. The motivation for showing these profiles is to illustrate that our halo model is capable of describing the kinematic data, and that the inner profile is not constrained by the data.

dSph a single, pressure-supported stellar population that is in dynamical equilibrium and traces an underlying gravitational potential dominated by DM. Implicit is the assumption that the orbital motions of stellar binary systems contribute negligibly to the measured velocity dispersions.[8] Furthermore, assuming spherical symmetry, the mass profile, $M(r)$, of the DM halo relates to (moments of) the stellar distribution function via the Jeans equation:

$$\frac{1}{\nu}\frac{\mathrm{d}}{\mathrm{d}r}(\nu\bar{v_r^2}) + 2\frac{\beta(r)\bar{v_r^2}}{r} = -\frac{GM(r)}{r^2}, \tag{18}$$

where $\nu(r)$, $\bar{v_r^2}(r)$ and $\beta_{\rm aniso} \equiv \beta(r) \equiv 1 - \bar{v_\theta^2}/\bar{v_r^2}$ describe the three-dimensional density, radial velocity dispersion and orbital anisotropy, respectively, of the stellar component. Projecting along the l.o.s., the mass profile relates to observable profiles, the projected stellar density $I(R)$ and velocity dispersion $\sigma_{\rm p}(R)$, according to (Binney & Tremaine 2008, hereinafter BT08)

$$\sigma_{\rm p}^2(R) = \frac{2}{I(R)}\int_R^\infty \left(1 - \beta_{\rm aniso}\frac{R^2}{r^2}\right)\frac{\nu\bar{v_r^2}r}{\sqrt{r^2-R^2}}\,\mathrm{d}r. \tag{19}$$

[8] Olszewski, Pryor & Armandroff (1996) and Hargreaves, Gilmore & Annan (1996) conclude that this assumption is valid for the classical dSphs studied here, which have measured velocity dispersions of $\sim$10 km s^{-1}. This conclusion does not necessarily apply to recently discovered 'ultrafaint' Milky Way satellites, which have measured velocity dispersions as small as $\sim$3 km s^{-1} (McConnachie & Côté 2010).

Note that while we observe the projected velocity dispersion and stellar density profiles directly, the l.o.s. velocity dispersion profiles provide *no* information about the anisotropy, $\beta_{\rm aniso}$. Therefore, we require an assumption about $\beta_{\rm aniso}$; here, we assume $\beta_{\rm aniso}$ = constant, allowing for non-zero anisotropy in the simplest way. For constant anisotropy, the Jeans equation has the solution (e.g. Mamon & Łokas 2005)

$$\nu\bar{v_r^2} = Gr^{-2\beta_{\rm aniso}}\int_r^\infty s^{2\beta_{\rm aniso}-2}\nu(s)M(s)\,\mathrm{d}s. \tag{20}$$

We shall adopt parametric models for $I(R)$ and $M(r)$ and then find values of the parameters of $M(r)$ that, via equations (19) and (20), best reproduce the observed velocity dispersion profiles.

4.1.1 Stellar density

Stellar surface densities of dSphs are typically fitted by Plummer (1911), King (1962) and/or Sérsic (1968) profiles (e.g. Irwin & Hatzidimitriou 1995). For simplicity, we adopt here the Plummer profile:

$$I(R) = \frac{L}{\pi r_{\rm h}^2}\frac{1}{(1+R^2/r_{\rm h}^2)^2}, \tag{21}$$

which has just two free parameters: the total luminosity L and the projected[9] half-light radius $r_{\rm h}$. Given spherical symmetry, the Plummer profile implies a three-dimensional stellar density (BT08) of

$$\nu(r) = -\frac{1}{\pi}\int_r^\infty \frac{{\rm d}I}{{\rm d}R}\frac{{\rm d}R}{\sqrt{R^2-r^2}} = \frac{3L}{4\pi r_{\rm h}^3}\frac{1}{(1+r^2/r_{\rm h}^2)^{5/2}}. \quad (22)$$

Since we assume that DM dominates the gravitational potential at all radii (all measured dSphs have central mass-to-light ratios $\gtrsim 10$, e.g. Mateo 1998), the value of L has no bearing on our analysis. We adopt values of $r_{\rm h}$ (and associated errors) from Table 1 in the published erratum to W09; these data originally come from the star count study of Irwin & Hatzidimitriou (1995). We have checked that a steeper outer slope or a steeper inner slope for the light profile leaves unchanged the conclusions (see Appendix H2).

4.1.2 DM halo

For the DM halo, we follow W09 in using a generalized Hernquist profile, as given by equation (6). In terms of these parameters, that is, the density $\rho_{\rm s}$ at scale radius $r_{\rm s}$, plus the (outer, transition, inner) slopes (α, β, γ), the mass profile is

$$M(r) = 4\pi\int_0^r s^2\rho(s){\rm d}s = \frac{4\pi\rho_{\rm s}r_{\rm s}^3}{3-\gamma}\left(\frac{r}{r_{\rm s}}\right)^{3-\gamma} {}_2F_1\left[\frac{3-\gamma}{\alpha}, \frac{\beta-\gamma}{\alpha}; \frac{3-\gamma+\alpha}{\alpha}; -\left(\frac{r}{r_{\rm s}}\right)^{\alpha}\right], \quad (23)$$

where ${}_2F_1(a, b; c; z)$ is Gauss' hypergeometric function.

Equation (6) includes plausible halo shapes ranging from the constant-density 'cores' ($\gamma = 0$) that seem to describe rotation curves of spiral and low-surface-brightness galaxies (e.g. de Blok 2010, and references therein) to the centrally divergent 'cusps' ($\gamma > 0$) motivated by cosmological N-body simulations that model only the DM component. For $(\alpha, \beta, \gamma) = (1, 3, 1)$, equation (6) is just the cuspy NFW (Navarro et al. 1996a; Navarro, Frenk & White 1997) profile.

4.2 MCMC method

For a given halo model, we compare the projected (squared) velocity dispersion profile $\sigma_{\rm p}^2(R)$ (obtained from equation 19) to the empirical profile $\langle\hat{V}^2\rangle(R)$ (displayed in Fig. 9) using the likelihood function

$$\zeta = \prod_{i=1}^{N}\frac{1}{\sqrt{2\pi{\rm Var}[\langle\hat{V}^2\rangle(R_i)]}}\exp\left[-\frac{1}{2}\frac{(\langle\hat{V}^2\rangle(R_i)-\sigma_{\rm p}^2(R_i))^2}{{\rm Var}[\langle\hat{V}^2\rangle(R_i)]}\right], \quad (24)$$

where ${\rm Var}[\langle\hat{V}^2\rangle(R_i)]$ is the variance associated with the empirical mean square velocity, as estimated from our bootstrap re-sampling.

In order to explore the large parameter space efficiently, we employ MCMC techniques, that is, we use the standard Metropolis–Hastings algorithm (Metropolis et al. 1953; Hastings 1970) to generate posterior distributions according to the following prescription: (1) from the current location in parameter space, S_n draw a prospective new location, S', from a Gaussian probability density centred on S_n; (2) evaluate the ratio of likelihoods at S_n and S'; and (3) if $\zeta(S')/\zeta(S_n) \geq 1$, accept such that $S_{n+1} = S'$, else accept with probability $\zeta(S')/\zeta(S_n)$, and $S_{n+1} = S_n$ with probability $1 - \zeta(S')/\zeta(S_n)$. In order to account for the observational uncertainty associated with the half-light radius adopted from Irwin & Hatzidimitriou (1995), for each new point, we scatter the adopted value of $r_{\rm h}$ by a random deviate drawn from a Gaussian distribution with standard deviation equal to the published error. This method effectively propagates the observational uncertainty associated with the half-light radius to the posterior distributions for our model parameters.

Solutions of the Jeans equations are not guaranteed to correspond to physical models, as the associated phase-space distribution functions may not be everywhere positive. An & Evans (2006) have derived a necessary relation between the asymptotic values of the logarithmic slope of the gravitational potential, the tracer density distribution and the velocity anisotropy at small radii. Models which do not satisfy this relation will not give rise to physical distribution functions. In terms of our parametrization, this relation becomes

$$\gamma_{\rm tracer} \gtrsim 2\beta_{\rm aniso}. \quad (25)$$

We therefore exclude from the Markov chain those models which do not satisfy this condition. Because the Plummer profiles we use to describe dSph surface brightness profiles have $\gamma_{\rm tracer} = 0$, this restriction implies $\beta_{\rm aniso} \lesssim 0$. Given our assumption of constant velocity anisotropy, this disqualifies all radially anisotropic models. Relaxing this condition affects the results on the J-factors, but the difference is contained within their CLs (see Appendix H2).

For this procedure, we use the adaptive MCMC engine CosmoMC (Lewis & Bridle 2002).[10] Although it was developed specifically for analysis of cosmic microwave background data, CosmoMC provides a generic sampler that continually updates the probability density according to the parameter covariances in order to optimize the acceptance rate. For each galaxy and parametrization, we run four chains simultaneously, allowing each to proceed until the variances of parameter values across the four chains become less than 1 per cent of the mean of the variances. Satisfying this convergence criterion typically requires $\sim 10^4$ steps for our chains. We then estimate the posterior distribution in parameter space using the last half of all accepted points (we discard the first half of points, which we conservatively assume corresponds to the 'burn-in' period).

5 DETECTABILITY OF MILKY WAY DSPHS

This section provides our key results. For the benefit of readers who start reading here, we summarize our findings so far.

In Section 2, we focused on generic $(1, 3, \gamma)$ profiles to show that, most of the time, the substructure contribution is negligible, and to check that the only relevant dSph halo parameters are the density normalization $\rho_{\rm s}$, the scale radius $r_{\rm s}$ and the inner slope γ (because $J_{\rm dSph} \propto r_{\rm s}^{2\gamma} \times (\alpha_{\rm int} d)^{3-2\gamma}$, see also Appendix B).

In Section 3, we provided the sensitivity of present and future γ-ray observatories, showing how it is degraded when considering 'extended' sources (e.g. a flat profile for close dSphs), and an instrument response that varies with energy.

In Section 4, we presented our method to perform a MCMC analysis of the observed stellar kinematics in the eight classical Milky Way dSphs under the assumptions of virial equilibrium, spherical symmetry, constant velocity anisotropy and a Plummer light distribution. The analysis uses the observed velocity dispersion

[9] For consistency with W09, we define $r_{\rm h}$ as the radius of the circle enclosing half of the dSph stellar light as seen in projection. Elsewhere, this radius is commonly referred to as the 'effective radius'.

[10] Available at http://cosmologist.info/cosmomc

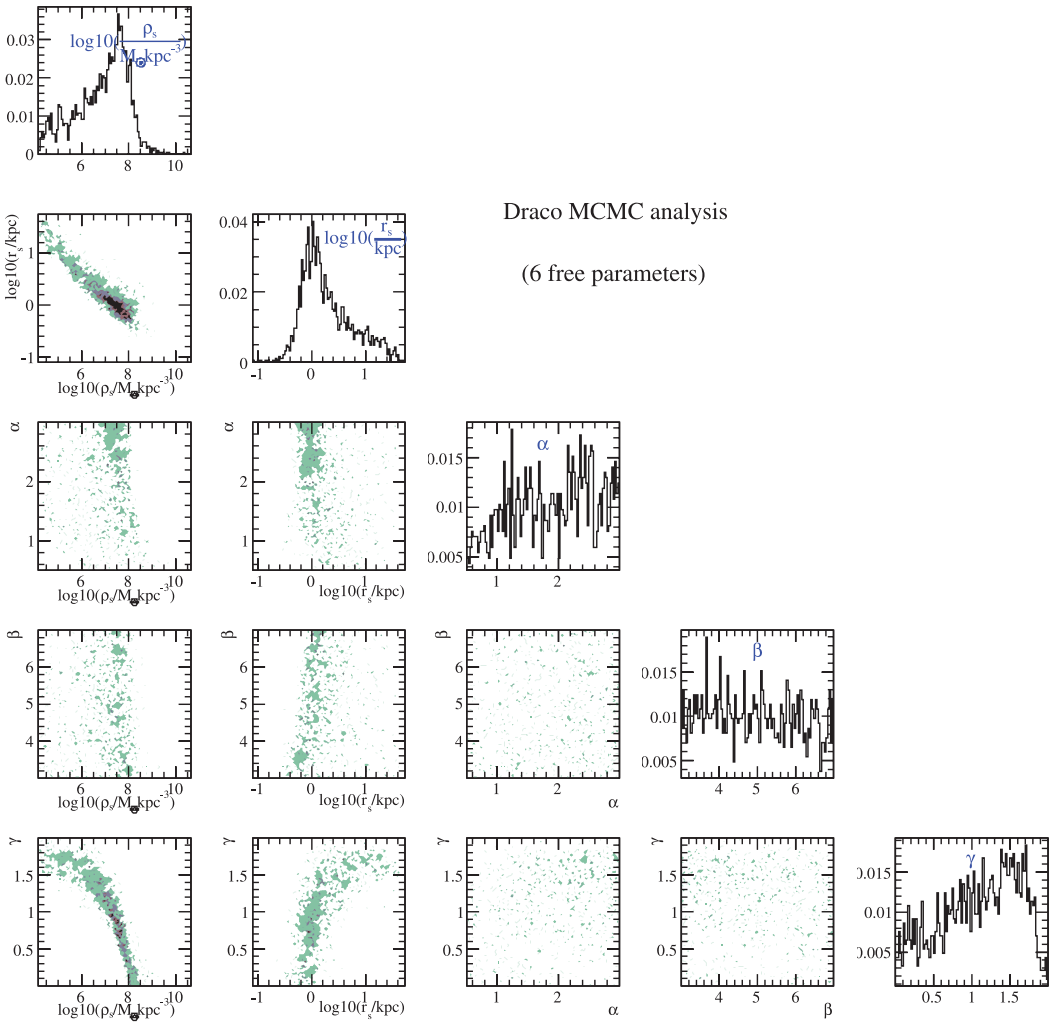

Figure 10. Joint distributions and marginalized PDFs of parameters entering the MCMC for the Draco dSph. The off-diagonal plots show joint distributions that highlight correlations between the parameters, while the on-diagonal plots are the marginalized PDFs of the parameters. This marginalization includes the marginalization over the velocity anisotropy parameter $\beta_{\rm aniso}$. (We do not plot a marginalized PDF or correlation for $\beta_{\rm aniso}$ since it is a nuisance parameter for our analysis here.)

profiles of the dSphs to constrain their underlying DM halo potentials, parametrized using the five-parameter models of equation (6).

5.1 Six-parameter MCMC analysis – varying γ

Our kinematic models have six free parameters, for which we adopt uniform priors over the following ranges:

$$
\begin{aligned}
-\log_{10}(1-\beta_{\rm aniso}) &: [-1,+1];\\
\log_{10}[\rho_{\rm s}/({\rm M}_\odot\,{\rm pc}^{-3})] &: [-10,+4];\\
\log_{10}[r_{\rm s}/{\rm pc}] &: [0,4];\\
\alpha &: [0.5,3];\\
\beta &: [3,7];\\
\gamma &: [0,2]\ \text{or}\ [0,1].
\end{aligned}
$$

The anisotropy parameter $\beta_{\rm aniso}$ does not enter directly the profile/mass/J calculation, although it is of fundamental importance for the fit as it can correlate with the DM profile structure parameters (so with the mass and the J-factor). We have not checked explicitly the details of these correlations, but we have checked that restricting the range of possible $\beta_{\rm aniso}$ does not significantly impact on the results for the J calculation. Hence, we do not discuss this parameter further below.

5.1.1 *Parameter correlations*

Fig. 10 shows the marginalized probability density functions (PDFs) of the profile parameters and the joint distributions of pairs of parameters. The features of these plots are driven by the fact that most of the stellar kinematic data lie at radii of up to few hundred parsecs (see Fig. 9). For instance, the outer slope β is not at all constrained (i.e. the fit is insensitive to the value of β), because only tracers beyond a radius of $r \gtrsim 1$ kpc are sensitive to this parameter and these radii are sparsely sampled by the observations. The transition slope α and then the inner slope γ are the two other least constrained parameters. In terms of best-fitting models, as shown in Fig. 9, the match to kinematic data is equally good for varying-γ (black) models and models in which we fix the value to $\gamma = 0$ (blue), or $\gamma = 1$ (red). In the following, we will not discuss further the best-fitting values. The more meaningful quantity, in the context of an MCMC analysis providing PDFs, is the *median* of the distribution.

Several groups have shown recently that in a Jeans analysis, the observed flatness of dSph velocity dispersion profiles (Walker et al. 2007) leads to a constraint on $M(r_h)$ – the mass enclosed within a sphere of radius r_h – that is insensitive to assumptions about either anisotropy or the structural parameters of the DM halo (W09; Wolf et al. 2010). Using for the appropriate radius the mass estimate (equation 9) and the above constraint leads to a relation between the profile parameters:

$$\log(\rho_s) + \gamma \log(r_s) \approx \text{constant}.$$

This relation explains the approximately linear correlations between these parameters seen, for instance, in the bottom left-hand panel of Fig. 10.

5.1.2 *From $\rho(r)$ to $J(\alpha_{int})$: uncertainty and impact of γ_{prior}*

Fig. F1 shows the density profile for Draco as recovered by our MCMC analysis. It is notable that the confidence limits are narrower for radial scales of a few hundreds pc – this is a common feature of the density profile confidence limits for all the dSphs we have considered. As discussed above, this is partly due to the fact that these are the radii at which the majority of the kinematic data lie. The least constrained $\rho(r)$ (less pronounced narrowing of the confidence limits) is that of Sextans, for which the range where useful data can be found is clearly the smallest compared to other dSphs (see Fig. 9).

The variation in the constraints on $\rho(r)$ as a function of radius impacts directly on the behaviour of J. Complications arise because it is the profile squared that is now integrated along a l.o.s. (given the integration angle α_{int}, see equation 5). The median value and 95 per cent CL on J as a function of the integration angle α_{int} is plotted in Fig. 11 (top panel), for two different priors on γ_{prior}.[11] The bottom panel gives the corresponding PDF for two integration angles. The prior has a strong impact on the result: the median (thick solid curves and large symbols – top panel) is changed by ∼50 per cent for $\alpha_{int} \gtrsim 0.^\circ1$, but by a factor of 10 for $\alpha_{int} \sim 0.^\circ01$. However, the most striking feature is the difference between the CLs: for the prior $0 \leq \gamma_{prior} \leq 2$, the typical uncertainty is three to four orders of magnitude (red dotted curves), whereas it is only less than or approximately equal to one order of magnitude for the prior $0 \leq \gamma_{prior} \leq 1$ (blue dotted curves).[12] The bottom panel of Fig. 11 shows that $\log_{10}J$ has a long and flat tail (associated with large γ values). This tail is responsible for the large upper limit of the J-factor CLs for $0 \leq \gamma_{prior} \leq 2$.

In Appendix G2, a detailed analysis of the impact of these two priors is carried on artificial data (for which the true profile is known). We find that the prior $0 \leq \gamma_{prior} \leq 2$ satisfactorily reconstructs $\rho(r)$ and $J(\alpha_{int})$, that is, the MCMC CLs bracket the true value. This is also the case when using the prior $0 \leq \gamma_{prior} \leq 1$. However, the following two important points are noteworthy:

(i) This prior obviously performs better for $0 \leq \gamma_{true} \leq 1$ profiles where it gives much tighter constraints on J.

[11] ASCII files containing the most-likely 68 and 95 per cent CLs on α_{int} for the eight classical dSph, for the prior $\gamma_{prior} \in [D - 1]$, may be found in the online version of this paper, see Supporting Information.

[12] Note that this behaviour is grossly representative of all dSphs, although the integration angle for which the uncertainty is the smallest and the amplitude of this uncertainty depend, respectively, on the dSph distance (see Section 2.3 for the generic dependence) and on the range/precision of the kinematic data (see above).

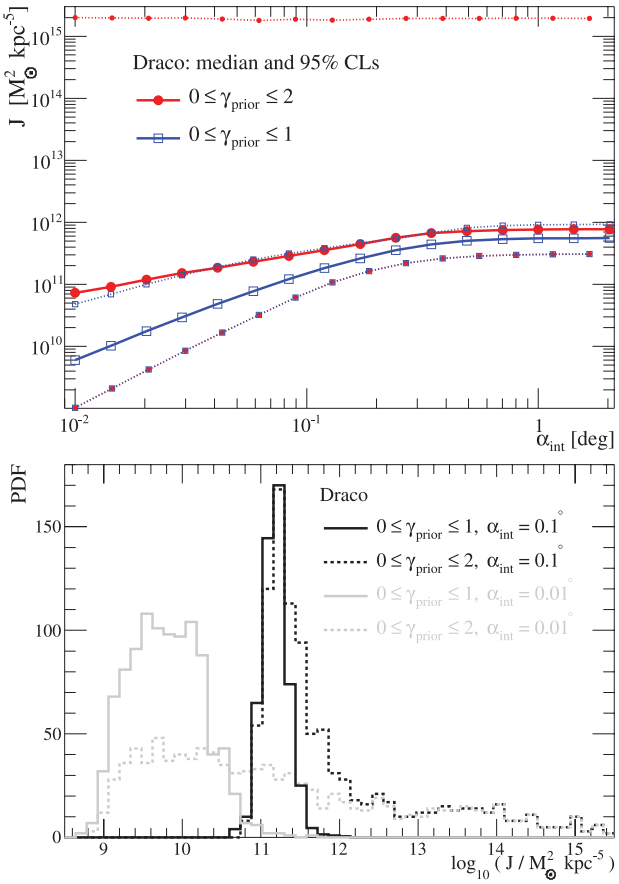

Figure 11. Top panel: $J(\alpha_{int})$ for Draco as a function of the integration angle. The solid lines correspond to the median model and dotted lines to the 95 per cent lower and upper CLs. The two sets of curves correspond to two different γ_{prior} for the MCMC analysis on the same data. Bottom panel: PDF of the J-factor for $\alpha_{int} = 0.^\circ01$ (grey) and $\alpha_{int} = 0.^\circ1$ (black), when the range of the inner slope prior is [0–1] (solid lines) or [0–2] (dashed lines).

(ii) For cuspier profiles (e.g. $\gamma_{true} = 1.5$), this prior succeeds slightly less (than the prior $0 \leq \gamma_{prior} \leq 2$) in reconstructing $\rho(r)$, but it does surprisingly better on J in terms of providing a value closer to the true one (see details and explanations in Appendix G2).

DM simulations and observations do not favour $\gamma > 1$, although steeper profiles can still fit the kinematic data in a Jeans analysis. Indeed, the Aquarius simulations indicate values of γ slightly smaller than 1, and although some recent simulations (Ishiyama, Makino & Ebisuzaki 2010) have argued for cuspy profiles, this happens for microhaloes only. Given that the J-factor for the cuspier profiles is only marginally more (or even less) reliable when using the prior $0 \leq \gamma_{prior} \leq 2$, we restrict ourselves to the $0 \leq \gamma_{prior} \leq 1$ prior below.

Note that other sources of bias exist. First, the reconstruction of $\rho(r)$ or $J(\alpha_{int})$ is affected by the choice of binning used in the estimation of the empirical velocity dispersion profiles. Appendix H1 shows that we obtain slightly different results when we apply our method to empirical velocity dispersion profiles calculated from the same raw kinematic data, but using different numbers of bins. We find that the effects of binning add an extra factor of a few uncertainty on J for the least well measured (in terms of radial coverage) dSphs, for which more measurements are desirable. (On the other hand, Fornax and Sculptor are found to provide robust results against different binnings.) Secondly, we note that the analysis presented here uses a fixed profile for the light distribution

Table 2. Positions of the classical dSphs (Mateo 1998) sorted according to their distance: longitude, latitude, distance, $2r_h$ (taken from Irwin & Hatzidimitriou 1995), the Galactic angle away from the centre $\phi = \cos^{-1}[\cos(\text{longitude})\cos(\text{latitude})]$ and $\alpha_c \approx 2r_h/d$ (see Walker et al. 2011). The remaining columns are the median values with 68 per cent (95 per cent) CLs for M_{300} and $\log_{10}[J(\alpha_{int})]$ from the six-parameter MCMC analysis ($0 \leq \gamma_{prior} \leq 1$). For conversion factors to units used in other studies, please refer to numbers given in Appendix A.

dSph	Longitude (°)	Latitude (°)	d (kpc)	$2r_h$ (kpc)	ϕ (°)	α_c (°)	M_{300} (10^7 $M_\odot$)	$\log_{10}[J(0.^\circ01)]$	$\log_{10}[J(0.^\circ1)]$ ($M_\odot^2$ kpc^{-5})	$\log_{10}[J(\alpha_c)]^a$
Ursa Minor	105.0	+44.8	66	0.56	100.6	0.49	$1.54^{+0.18(+0.33)}_{-0.21(-0.42)}$	$10.5^{+0.8(+1.5)}_{-0.6(-1.2)}$	$11.7^{+0.5(+0.8)}_{-0.3(-0.6)}$	$12.0^{+0.3(+0.5)}_{-0.1(-0.2)}$
Sculptor	287.5	−83.2	79	0.52	88.0	0.38	$1.34^{+0.12(+0.23)}_{-0.13(-0.23)}$	$10.0^{+0.5(+0.9)}_{-0.5(-0.8)}$	$11.3^{+0.2(+0.4)}_{-0.2(-0.3)}$	$11.7^{+0.1(+0.2)}_{-0.1(-0.1)}$
Draco	86.4	+34.7	82	0.40	87.0	0.28	$1.22^{+0.15(+0.28)}_{-0.14(-0.28)}$	$9.8^{+0.5(+0.9)}_{-0.5(-0.8)}$	$11.2^{+0.2(+0.4)}_{-0.2(-0.3)}$	$11.6^{+0.1(+0.2)}_{-0.1(-0.2)}$
Sextans	243.5	+42.3	86	1.36	109.3	0.91	$0.61^{+0.38(+0.96)}_{-0.31(-0.43)}$	$9.4^{+1.7(+2.9)}_{-1.2(-1.8)}$	$10.7^{+1.1(+1.9)}_{-0.8(-1.1)}$	$11.1^{+0.7(+1.5)}_{-0.4(-0.6)}$
Carina	260.1	−22.2	101	0.48	99.2	0.27	$0.59^{+0.10(+0.60)}_{-0.07(-0.14)}$	$9.3^{+0.3(+0.8)}_{-0.4(-0.8)}$	$10.5^{+0.2(+0.4)}_{-0.1(-0.2)}$	$10.9^{+0.1(+0.1)}_{-0.1(-0.1)}$
Fornax	237.1	−65.7	138	1.34	102.9	0.56	$1.01^{+0.30(+0.60)}_{-0.17(-0.28)}$	$9.5^{+0.5(+1.1)}_{-0.5(-0.8)}$	$10.8^{+0.2(+0.5)}_{-0.2(-0.3)}$	$10.5^{+0.3(+0.7)}_{-0.2(-0.4)}$
Leo II	220.2	+67.2	205	0.30	107.2	0.08	$0.94^{+0.26(+0.50)}_{-0.18(-0.29)}$	$11.6^{+0.8(+1.7)}_{-0.8(-1.5)}$	$11.7^{+0.7(+1.6)}_{-0.6(-0.9)}$	$11.7^{+0.7(+1.6)}_{-0.6(-0.9)}$
Leo I	226.0	+49.1	250	0.50	117.1	0.11	$1.22^{+0.24(+2.52)}_{-0.21(-0.36)}$	$9.7^{+0.3(+1.0)}_{-0.2(-0.5)}$	$10.7^{+0.1(+0.3)}_{-0.1(-0.2)}$	$10.7^{+0.1(+0.3)}_{-0.1(-0.2)}$

[a]Note that the values for $\log_{10}[J(\alpha_c)]$ differ from those quoted in Walker et al. (2011) as the MCMC analysis is slightly different here.

which, when combined with our assumption of constant velocity anisotropy, restricts the possible halo profiles we can recover. Our constraints on $\rho(r)$ and $J(\alpha_{int})$ are therefore sensitive to these assumptions (see e.g. Strigari, Frenk & White 2010, for an example of fitting the dSph kinematic data with cusped profiles when the light profile is also allowed to be cusped), although this does not change our conclusions (see Appendix H2 where different light profiles are used). This situation is set to change over the coming years as new distribution function-based models will permit constraints to be placed on the slope of the DM density profiles (Wilkinson et al., in preparation).

5.1.3 Best constraints on J: median value and CLs

As validated by the simulated data, we are now able to provide robust (although possibly not the best achievable with current data) and model-independent constraints on $J(\alpha_{int})$ for the eight classical dSphs. The results are summarized in Table 2 in terms of the median, and 68 and 95 per cent CLs. The J-factor is calculated for $\alpha_{int} = 0.^\circ01$ (an angle slightly better than what can be achieved with the FCA), $\alpha_{int} = 0.^\circ1$ (typical of the angular resolution of existing GeV and TeV γ-ray instruments) and $\alpha_c = 2r_h/d$ (as proposed in Walker et al. 2011). We do not report the values of ρ_s and r_s as these vary across a large range – and therefore do not give additional useful information – nor the value of γ as it is forced in the range $0 \leq \gamma_{prior} \leq 1$ to give the least biased J value.

There is no simple way to provide unambiguously the best target, as their relative merit depends non-trivially on their distance, their mass and the integration angle selected. As proposed in Walker et al. (2011), since the most robust constraint on J is obtained for $\alpha_{int} = \alpha_c$, having different integration angles for each dSph can be a good starting point to establish a relative ranking. The situation is complicated further for background-limited instruments such as the CTA, as some loss of sensitivity can occur (see e.g. fig. 4 of Walker et al. 2011). This is discussed, taking into account the full detail of the instruments, in Section 5.3. However, in this respect, the best target for future instruments may eventually become Leo II, which, despite a quite large uncertainty, outshines all other dSphs at $\alpha_{int} = 0.^\circ01$ (see also Fig. 12). We note, however, that it is the dsph with the smallest amount of kinematic data at present (so it has the most uncertain J-factor).

5.1.4 dSphs in the diffuse Galactic DM signal: contrast

The uncertainties in J are illustrated from a different viewpoint in Fig. 12. It shows, in addition to the mean, 68 and 98 per cent CLs on the J-factors, the latitudinal dependence of the Galactic DM background (smooth and Galactic clump contributions) for the same integration angle.[13] For a typical present-day instrument resolution (integration angle $\alpha_{int} \sim 0.^\circ1$), we recover the standard result that the Galactic Centre outshines all dSphs.

The three panels illustrate the loss of contrast (signal from the dSph with respect to the diffuse Galactic DM signal) as the integration angle is increased. This is understood as follows: the integrand appearing in equations (C4) and (C5) is mostly insensitive to the l.o.s. direction a few tens of degree away from the Galactic Centre, so that equation (C6) holds, giving an α_{int}^2 dependence.

For detectability (see also Section 3), the naïve approach of maximizing the integration angle (to maximize J_{dSph}) must be weighed against the fact that an increased integration angle means more astrophysical γ-ray and cosmic-ray background. For large integration angles, dSphs also have poor contrast against the diffuse Galactic DM annihilation signal, indicating that the Galactic halo is a better target for any search on angular scales $\gtrsim 1$ (see e.g. Abramowski et al. 2011b for such a search with the HESS).

5.1.5 Comparison with other works

Comparison between different works can be difficult as every author uses a different definition, notations and units for the astrophysical

[13] The smooth profile is taken to be an Einasto profile, the clump distribution is a core one, whereas their inner profile is Einasto with concentration and parameters *à la* B01. Normalizing the mass distribution to have 100 clumps more massive than 10^8 $M_\odot$, and taking $dP/dM \propto M^{-1.9}$, leads to a DM fraction into clumps of ∼10 per cent for clumps distributed in the range 10^{-6}–10^{10} $M_\odot$ (see e.g. Lavalle et al. 2008, and references therein). The local DM distribution is fixed to the fiducial value $\rho_\odot = 0.3$ GeV cm^{-3}. The exact configuration is unimportant here as this plot is mostly used for illustration purpose.

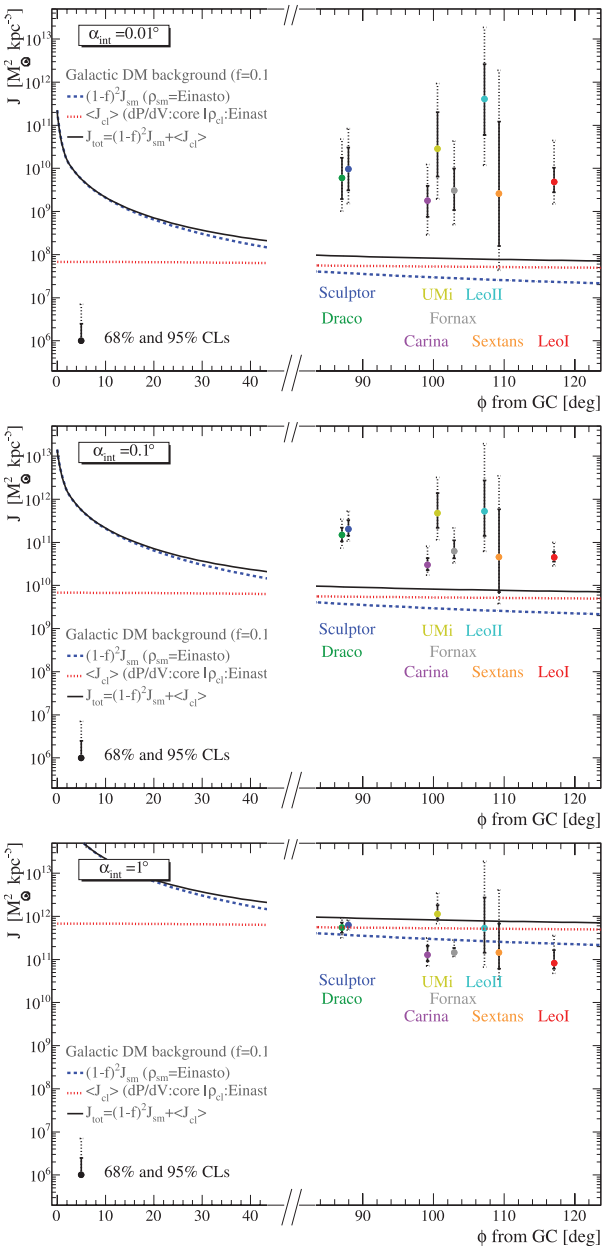

Figure 12. Galactic contributions to J for the smooth (blue-dashed line), mean clump (red-dotted line) and sum (black-solid line) versus the angle from the Galactic Centre. The symbols show J for the dSphs, assuming a prior of $0 \leq \gamma_{\rm prior} \leq 1$ on the central DM slope. The central point corresponds to the median values, the solid bars to the 68 per cent CLs and the dotted bars to the 95 per cent CLs. The integration angle is, from the top to bottom, 0.°01, 0.°1 and 1°, respectively. The Galactic contributions $J_{\rm sm}$ and $\langle J_{\rm subcl} \rangle$ scale as $\alpha_{\rm int}^2$, but $J_{\rm dSph}$ does not, changing the contrast of the dSphs with respect to the DM Galactic background (see text for details).

factor. To ease the comparison, we provide in Appendix A conversion factors between standard units (we also point out issues to be aware of when performing such comparisons).

Below is a comparison with just a few of the works published on the subject, and only for the objects that these studies and the present one have in common:

(i) The Evans et al. (2004) values of $J/\Delta\Omega$ for Draco (with $\Delta\Omega = 10^{-5}$ i.e. $\alpha_{\rm int} = 0.°1$) for all the profiles they explored (cored, $\gamma = 0.5$, $\gamma = 1$, $\gamma = 1.5$) are larger (after correction by $\Delta\Omega$, given their definition of the astrophysical factor) than our 95 per cent CL upper limit for this object, shown in Table 2. The difference is probably related to our data set which is about twice as large as that used by Evans et al. (2004).

(ii) Strigari et al. (2007b) provide directly the γ-ray flux (i.e. including the particle physics term), so that we can only compare our respective rankings. These agree in general but for Sculptor we find a larger flux than Draco, contrary to these authors.

(iii) Pieri et al. (2009a) focused on Sextans, Carina, Draco and Ursa Minor. They found the latter to have the largest J ($\Phi_{\rm cosmo}$ in their notation) of these four objects, followed by Draco, Carina and Sextans. For the last two, this ranking is similar to ours. However, while their values of J fall within our 68 per cent (Ursa Minor, Sextans) or 95 per cent (Carina) CL, their value for Draco is above our 95 per cent CL upper limit.

(iv) Essig et al. (2009) also performed a statistical study on Draco and Ursa Minor, to determine their profiles from kinematic data and to derive the CLs on the J-factor. Given that their integration is performed on a slightly larger opening angle (0.°14), our results appear to be in agreement. Their 90 per cent CL limits are two to three times larger than the 95 per cent CL limits given in Table 2, but this may be due to the larger range they adopt for the prior on the inner slope (see Appendix G1).

(v) Kuhlen (2010) gives the astrophysical factors of all the dSphs using a point-like approximation and a NFW DM profile, and integrated with a $\alpha_{\rm int} = 0.°15$ angular resolution. These can be compared to the median and CLs we derived in Table 2 for $\alpha_{\rm int} = 0.°1$. The values of Kuhlen (2010) (multiplied by 4π to match our definition of J) generally fall inside our 68 per cent CL intervals, but for Leo II his value is just within our 95 per cent confidence interval (CI), while Draco and Carina cannot be accommodated at all. For these two objects, the values of Kuhlen (2010) are much larger than the ones we find, and this is unlikely to be explained by the 0.°05 difference in integration angles. A simple explanation is that Kuhlen (2010) does not use stellar kinematic data directly in his analysis, but stacks suitable Via Lactea haloes ($M_{300} \approx 10^7\,{\rm M}_\odot$ and appropriate distances) and uses those averages to estimate J. Focusing on the ranking (without worrying about contrast to the background and the other instrumental constraints), both we and Kuhlen (2010) agree that among the classical dSphs, Ursa Minor is a most promising target. However, while we find Sculptor and Draco to be the next most favourable targets, Kuhlen (2010) names Draco and Carina from his 'simulation-based' approach.

For completeness, we also compare our median values with the J values used by different experimental groups:

(i) The MAGIC Collaboration published point source limits for Draco (Albert et al. 2008) adopting the scheme of Sánchez-Conde et al. (2007) of a power-law density profile, with an exponential cut-off. They examine two scenarios, a cored and a cusped model, but find no discernable difference when calculating J for integration angles $<0.°4$, that is, larger than the MAGIC PSF. The value of J they calculate for Draco is higher than ours (after appropriate scaling of the integration region and unit conversion) by about a factor of 2.

(ii) The VERITAS Collaboration also published limits on Draco and Ursa Minor (Acciari et al. 2010). They assume a NFW profile, take the density profiles from Strigari et al. (2007b) and follow Bergström et al. (1998) for the calculation of J. Whilst the range of density values in Strigari et al. (2007b) has a physical motivation, the values used in Acciari et al. (2010) are rather arbitrarily chosen to be the mid-point of that range, which leads to consistently higher

J-values than ours (by a factor of 3 for Draco and a factor of 1.2 for Ursa Minor).

(iii) The HESS Collaboration (Abramowski et al. 2011a) published limits on the southern sources Sculptor and Carina using NFW and isothermal profiles with a number of varying assumptions. This leads to a range of calculated J-values (rather than a single solution) that are consistent with our median value and estimated uncertainties.

(iv) The Fermi Collaboration (Abdo et al. 2010) has published limits for a number of the sources studied here. They adopted a NFW profile within the tidal radius and following Martinez et al. (2009) they calculated the J-value (using an MCMC approach on the observed stellar velocities) for a 1° integration angle which is compatible with their high-energy PSF. From this, they find Draco to have a larger J compared to the other dwarfs (a factor of ∼2 higher than the next dwarf which is Ursa Minor), contrary to what we find in this study.

5.2 Five-parameter MCMC analysis: $\gamma_{\rm prior}$ fixed

Higher resolution numerical simulations following both DM and gas, additional kinematic data and new modelling techniques may help constraining the value of γ in the near future. With the knowledge of γ, we should better constrain the radial dependence of J, which is crucial to disentangle, for example, DM annihilation from DM decay (Boyarsky et al. 2006; Palomares-Ruiz & Siegal-Gaskins 2010). The topic of decaying DM goes beyond the scope of this paper, and it will be discussed elsewhere. Below, we merely inspect the gain obtained on the J prediction when having a strong prior on γ, and briefly comment on the possibility to disentangle $\gamma = 0$ profiles from $\gamma = 1.0$ profiles in the case of annihilation (if this cannot be achieved, hopes for disentangling decay from annihilation would be quite low on a single object).

5.2.1 Parameter correlations

We repeat the MCMC analysis for fixed values of the inner slope $\gamma_{\rm prior} = 0.$, 0.5, 1., and 1.5. The priors for the five other parameters are as given in Section 5.1.

Using equation (9) for the mass having a robust estimate of $M(r_{\rm h})$ (W09; Wolf et al. 2010; Amorisco & Evans 2011) gives $\log(\rho_{\rm s}) + \gamma \log(r_{\rm s}) \approx$ constant which reduces to $\log(\rho_{\rm s}) \approx$ constant for $\gamma = 0$. As a result, we expect a strong correlation between $\rho_{\rm s}$ and $r_{\rm s}$ when $\gamma_{\rm prior} = 1$ and none when $\gamma_{\rm prior} = 0$. This is confirmed by the result of our MCMC analysis shown in Fig. 13 (here, for the Draco case). The half-light radius $r_{\rm h}$ for Draco is ∼200 pc, but we choose to show the PDF for M_{300} in the bottom panel of Fig. 13 as we wish to compare the mass of the dSphs among themselves (see Table 2). It confirms that the mass within an appropriate radius can be reliably constrained by the data regardless of the value of γ.

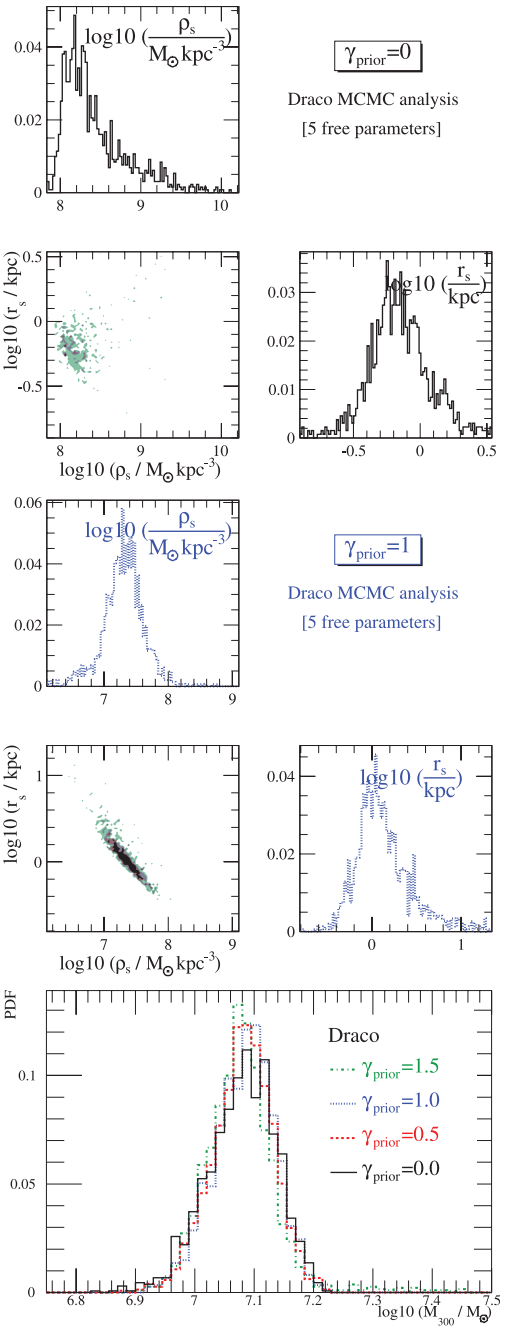

Figure 13. Top panels: correlation and PDF of the profile parameters $\rho_{\rm s}$ and $r_{\rm s}$ from the five-parameter MCMC analysis $\gamma_{\rm prior} = 0.0$. Middle panels: same, but for $\gamma_{\rm prior} = 1.0$. Bottom panel: PDF of M_{300}, the mass at 300 pc.

5.2.2 Uncertainties on the profile and on J

For any given γ, the uncertainty on $\rho(r)$ at small radii is related to the range of $r_{\rm s}$ values at which the asymptotic slope is reached (for each profile accepted by the MCMC analysis). For $\gamma_{\rm prior} = 0$, the maximum uncertainty on $\rho(r)$ is directly related to the maximum uncertainty on $\rho_{\rm s}$ [since for $r \ll r_{\rm s}$, $\rho(r)$ is constant] which can be read off the PDF (top left-hand panel of Fig. 13). This leads to an order of magnitude uncertainty on $\rho(r)$ for small r, which is consistent with the 95 per cent CL shown in the top panel of Fig. 14.

For $\gamma > 0$, the uncertainty has to be read from the dispersion in the values of $\rho_{\rm s} r_{\rm s}^{\gamma}$, or equivalently, the mass M_{300}. The bottom panel of Fig. 13 shows that this mass is well constrained, independently of γ for the case of Draco (see, however, in Table 2 for a larger spread for some dSphs), resulting in a smaller uncertainty for $\gamma_{\rm prior} = 1.5$ than for $\gamma_{\rm prior} = 0$ (top panel of Fig. 13). We checked that the CLs obtained in Fig. 14 (in Appendix G2) for the artificial data enclose correctly the range of reconstructed values: they are consistent with a larger reconstruction bias for $\gamma_{\rm prior} = 0$ than for $\gamma_{\rm prior} = 1.5$ at small radii.

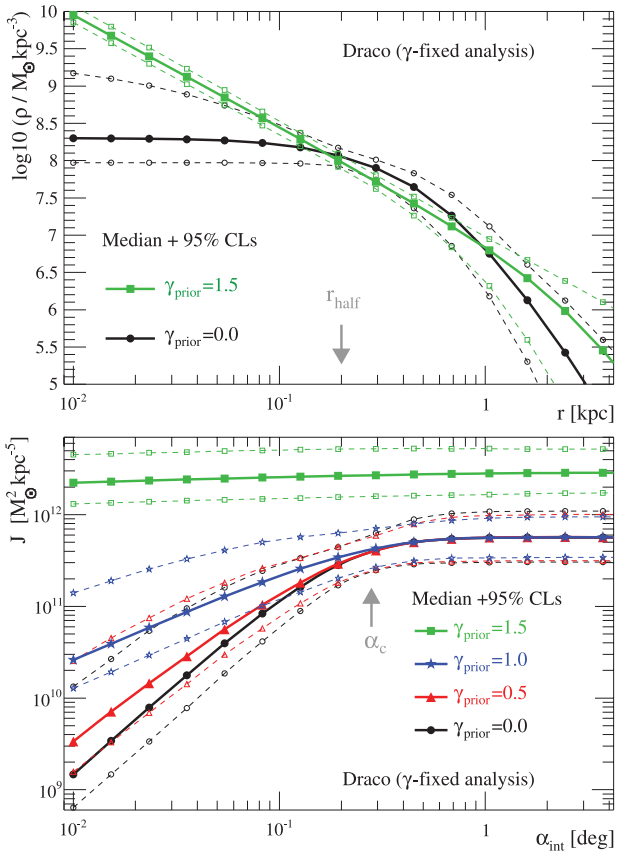

Figure 14. Median values (solid lines, filled symbols) and 95 per cent CLs (dashed lines, empty symbols) from the fixed $\gamma_{\rm prior}$ MCMC analysis on Draco. Top panel: density profiles (the grey arrow indicates the value of $r_{\rm h}$). Bottom panel: J-factor (the grey arrow indicates $\alpha_{\rm c} \approx 2r_{\rm h}/d$).

For the uncertainty on J, we can obtain a crude estimate by relying on the approximate formulae given in Appendix B. For $\gamma > 0$, $J \propto \rho_{\rm s}^2 r_{\rm s}^3$, and substituting the constant M_{300} relationship leads to $J \propto r_{\rm s}^{3-2\gamma}$. The value of $r_{\rm s}$, as seen in its PDF in the top and middle panels of Fig. 13, varies by roughly a factor of 10. Because of the weighting power $3 - 2\gamma$, the uncertainty on J is expected to be the smallest for $\gamma = 1.5$, which is in agreement with the curves in Fig. 14 (bottom panel). However, the analysis of the artificial data in Appendix G2 shows that the typical CL on J obtained in the bottom panel of Fig. 14 is likely to be underestimated for $\gamma_{\rm prior} = 1.5$ [up to factor $\mathcal{O}(2)$, see Fig. G2].[14] This happens for any integration angle. For this reason, we cannot rely on the J-value for $\gamma_{\rm prior} = 1.5$ and focus only on the three cases $\gamma_{\rm prior} = 0$, 0.5 and 1.0 below.

5.2.3 *J(d) and departure from the 1/d² scaling*

Fig. 15 shows the J median values, 65 and 95 per cent CIs as the symbols, dashed and solid error bars, respectively, for an integration angle of 0.°01 (top panel), 0.°1 (middle panel) and $\alpha_{\rm c} \approx 2r_{\rm h}/d$ (Walker et al. 2011). The x-axis is the distance from the dSph (in kpc). For point-like sources, the J-factor of a single dSph scales as $1/d^2$, as illustrated by the blue-dashed line. Departure from this scaling is interpreted as a combination of a mass effect and/or a profile effect. For instance, Sextans and Carina are dSphs with smaller M_{300} with respect to the other ones (see Table 2); consequently, they are located below the dashed blue line in the top panel of Fig. 15. The exception is Leo II, which has a 'small' mass but is nevertheless above the dashed line. Although this analysis cannot constrain γ, we are tempted to interpret this oddity in terms of a 'cuspier' profile (with respect to those for other dSphs), which would be consistent with the fact that its J remains similar in moving from $\alpha_{\rm int} = 0.°1$ (middle panel) to 0.°01 (top panel). However, an alternative explanation (which would be more consistent with the results obtained in this paper) could be the fact that Leo II has the smallest amount of kinematic data at present, and that its J is overestimated (see Appendix H1 to support this line of argument). We repeat that the relative brightness of the dSphs is further affected for background-dominated instruments (as described in Section 3), so that the ranking has to be based on Fig. 16 discussed in the next section.

The bottom panel of Fig. 15 shows the J-value for an 'optimal' integration angle $\alpha_{\rm c}$ that is twice the half-light radius divided by the dSph distance[15] (this corresponds to the integration angle that minimizes the CLs on J; see Walker et al. 2011). The yellow broken solid lines show the expected signal from the diffuse Galactic DM annihilation background, including a contribution from clumpy substructures (the extragalactic background, which also scales as $\alpha_{\rm int}^2$, has not been included). The total background may be uncertain by a factor of a few [depending on the exact Galactic (smooth) profile and local DM density]. Its exact level – which depends on the chosen integration angle – determines the condition for the loss of contrast of the dSph signal, that is, the condition for which looking at the DM halo (rather than at dSphs) becomes a better strategy.

5.2.4 *Conclusion for the fixed γ_{prior} analysis*

The analysis of simulated data shows that the analysis for $\gamma_{\rm prior} = 1.5$ is biased by a factor of $\mathcal{O}(10)$ and that the CLs obtained on the real data are likely to be severely underestimated in that case. However, such steeply cusped profiles are neither supported by observations nor motivated by current cosmological simulations. For values of $\gamma_{\rm prior} \leq 1$, this bias is a factor of a few only, so that it shows that the results from a fixed $\gamma_{\rm prior}$ analysis of the eight classical dSphs are robust. However, this analysis shows that unless very small integration angles, $\alpha_{\rm int} \lesssim 0.°01$, are chosen (or if $\gamma_{\rm true} \gtrsim 1$), knowing the exact value of γ does not help in improving the determination of J. Indeed, even using Draco, the stellar population of which is one of the most studied, the CLs of the three reconstructed fluxes ($\gamma_{\rm prior} = 0$ in black full circles, $\gamma_{\rm prior} = 0.5$ in red triangles and $\gamma_{\rm prior} = 1.0$ in blue stars) in Fig. 14 (bottom panel) overlap. Reversing the argument, if we do not know the inner slope, and if a γ-ray signal is detected from just one dSph in future, there will be little hope of recovering the slope of the DM halo from that measurement only.

This means that the best way to improve the prediction of the J-factor in the future relies on obtaining more *data* and a more refined MCMC analysis; an improved prior on the DM distribution makes little difference.

[14] This is understood as for the latter, the inner region ($r \ll r_{\rm s}$) contributes the most to J, and even small differences for $\rho(r \sim r_{\rm s})$ are bound to translate in sizeable differences for $\rho(r \to 0)$. Conversely, similar differences on ρ for shallower profiles are not an issue as their inner parts do not contribute to J.

[15] CLs for $J(\alpha_{\rm int})$ are provided along with this paper for readers interested in applying our analysis to existing and future observatories.

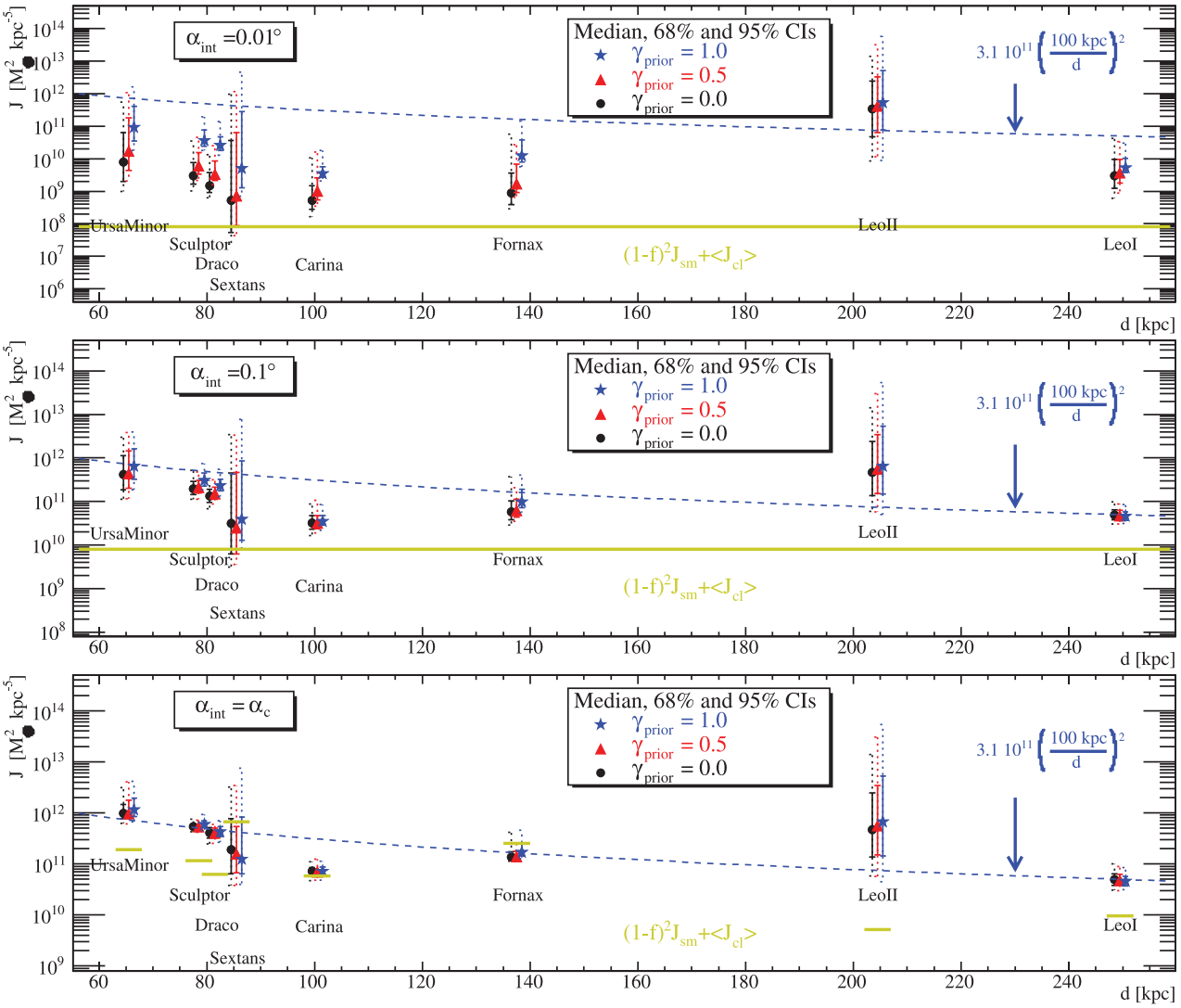

Figure 15. Median J-factor values (symbols) and 68 per cent/95 per cent CLs (solid bars/dashed bars) for the fixed $\gamma_{\rm prior}$ analysis (the result for $\gamma_{\rm prior} = 1.5$ is not shown because it is not reliable, see Section G2). The blue dashed line shows the expected scaling with distance for point sources: $3.1 \times 10^{15} d^{-2}$ ($M_\odot^2$ kpc^{-5}). The panels show, from the top to bottom, three integration angles $\alpha_{\rm int} = 0.^\circ01$, $0.^\circ1$ and $\alpha_{\rm c} \approx 2r_{\rm h}/d$ (an angle very similar to the angle enclosing 80 per cent of the flux, see Fig. 16) that optimize the determination of the J-factor for a given dSph (hence the error bars are smaller in this plot than in the other two). The yellow solid lines (and broken lines in the bottom panel) correspond to the Galactic DM background including both the smooth and clumpy distributions. For the bottom panel, this is not a smooth curve since it depends on the integration angle $\alpha_{\rm int}$ that varies from dSph to dSph in this figure. Note that the choice of using the critical angle $\alpha_{\rm int} = \alpha_{\rm c}$ is optimal in the sense that it gives the most constrained value for J. However, where the Galactic background annihilation signal approaches that of the dSphs (see e.g. Sextans and Fornax), the motivation for staring at the dSphs rather than simply looking at the Galactic halo is gone.

5.3 Sensitivity of γ-ray observatories to DM annihilation in the dSphs

The potential for using the classical dSph to place constraints on the DM annihilation cross-section, given the uncertainties in the astrophysical J-factor, can be seen in Fig. 16. Previous analyses have adopted the solid angle for the calculation of the J-factor to be the angular resolution of the telescope for a point-like source, typically assuming a NFW-like profile (Abdo et al. 2010; Acciari et al. 2010; Abramowski et al. 2011a). By contrast, our sensitivity plots take into account finite size effects: (i) the J values are based on the MCMC analysis with the prior $0 \leq \gamma_{\rm prior} \leq 1$, where the corresponding J are shown in Fig. 12; and (ii) the energy-dependent angular resolution has also been taken into account assuming a standard γ-ray annihilation spectrum (see Section 2.1.1). Moreover, for the *Fermi*-LAT, the background level assumed has been increased (resulting in a 25 per cent worsening of the sensitivity above 100 MeV) to reflect the average situation in the directions of the classical dSph (the variation between the individual dSphs is only 7 per cent rms). A likelihood-based analysis is used for both the FCA and *Fermi* and a nominal observation zenith angle of 20° assumed for the FCA[16] (see Section 3.2).

The panels from the top to bottom correspond to increasing DM (neutralino) masses. At low values, *Fermi* has a better sensitivity

[16] The energy threshold for a ground-based instrument is dependent on the zenith angle of observation. This means that the actual energy threshold for a given object will depend on the object's declination and the latitude of the, yet to be determined, FCA site.

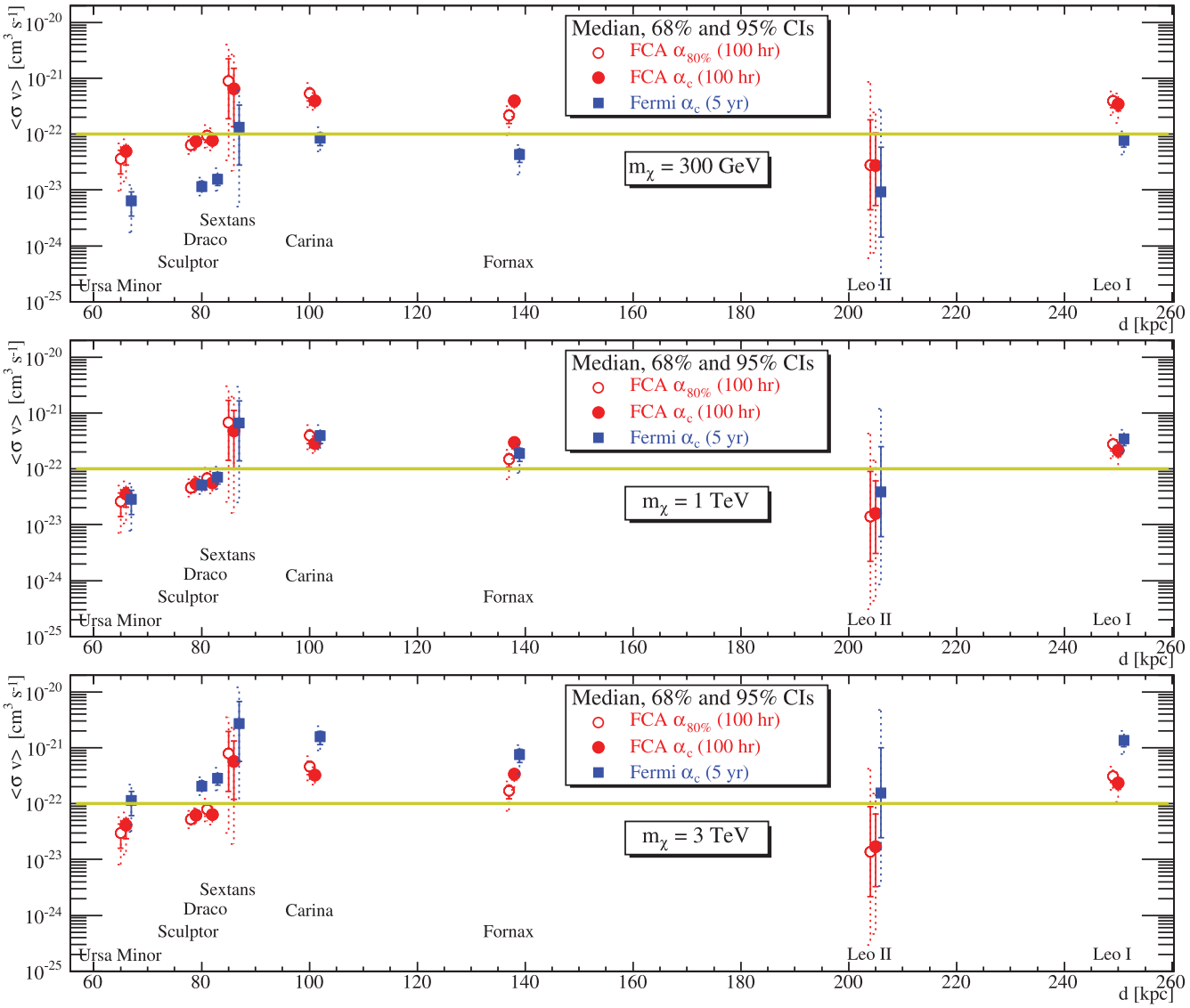

Figure 16. Minimum detectable $\langle\sigma v\rangle$ for known dSphs shown as a function of their distance, for different assumed DM masses (separate panels). 100-hour observations with an FCA (red circles) are compared to 5 years of *Fermi* observations (blue squares). Error bars indicate 65 per cent (solid lines) and 95 per cent (dotted lines) confidence limits. The integration angle is adapted to α_c of each dSph and the energy-dependent PSF of the two instruments. The strategy of using α_{80}, rather than α_c, is indicated with the hollow symbols for the FCA case. The line for $\langle\sigma v\rangle = 10^{-22}$ cm^3 s^{-1} is drawn for comparison purpose between the panels.

than the FCA; at a mass of about 1 TeV, the two are comparable, and for higher masses, the FCA becomes the more sensitive instrument due to the vastly greater effective area at the photon energies at which the annihilation spectrum is expected to peak. Note that the precise value of $\langle\sigma v\rangle$ where the relative sensitivities of the two instruments cross depends on the form of the DM annihilation spectrum. Since we are examining the uncertainties in the astrophysical J-factor to the detectability of dSphs, we have used a conservative spectrum averaged over a number of possible annihilation channels (see Fig. 1) which results in the majority of produced γ-ray photons having energies $\simeq 10$ per cent of the DM particle mass. If we were to move from a relatively soft spectrum, such as $b\bar{b}$ to a harder one, such as $\tau^+\tau^-$, this would benefit both instruments in different ways. For the *Fermi*-LAT, a harder spectrum makes the signal easier to distinguish above the diffuse γ-ray background; indeed, Abdo et al. (2010) found that the detectable flux limit from a potential source could vary by a factor of 2–20 (with lower particle masses benefiting the most) between these different annihilation spectra. For the FCA, which has a very large effective area to photons $\geq$ 100 GeV, the benefits of having more high-energy photons are very apparent when it comes to flux sensitivity. For both observatories, an increased number of high-energy photons needs to be balanced with the correspondingly better angular resolution, particularly if (e.g. for the *Fermi*-LAT) a point-like source becomes spatially resolved.

Our analysis places Ursa Minor as the best candidate for the northern sky (marginally better than Draco, which has long been a favourite target of Northern hemisphere observatories), and Sculptor for the southern sky, when it comes to a favourable median and low uncertainty in the J-factor. It should be noted, however, that although the closest objects seem to be favoured, Leo II has the potential to yield a stronger signal; however, more kinematic data are needed in order to constrain better its J-factor. In addition, it should be

noted that the uneven sensitivity of the *Fermi*-LAT across the sky, caused in particular by the proximity of bright sources[17] as well as the Galactic diffuse background, can change what is considered the favorite candidate.

We emphasize that in our analysis the inner slope γ has not been constrained, but that a better independent determination of γ in future will not help providing a better determination of J (see Fig. 15); this is discussed further in the appendices. Carina, Fornax and Leo I are the targets least favoured. When compared to existing limits from the *Fermi*-LAT (Abdo et al. 2010) or the current generation of ACTs (Acciari et al. 2010; Abramowski et al. 2011a), it can be seen that our limits are not dissimilar to those that have already been published. For *Fermi* this is not surprising, since the source is unresolved and any difference should relate only to the assumed increase in exposure from 1 to 5 years, resulting in a factor of a few at best. The similarity in sensitivity between current and future ACTs is perhaps more surprising, but this as stated earlier relates to the naïve assumptions made on the form for the J-factor and the solid angle integrated over; in order to reach the currently claimed limits requires a deep exposure with an instrument as sensitive as the CTA.

One last thing to note is that a common way to synthesize a deeper exposure is to stack observations of different sources together to provide an effective long exposure of a generic source. For a common universal halo profile, this may be fine; however, any analysis will have to take into account the different integration angles for each individual source correctly. If all dSphs do not share a common halo profile and hence have different γ values, we have to rely on the varying-γ analysis presented in the previous section and the relative ranking of potential targets would then be different.

6 DISCUSSION AND CONCLUSIONS

We have revisited the expected DM annihilation signal from dSph galaxies for current (*Fermi*-LAT) and future (e.g. CTA) γ-ray observatories. The main innovative features of our analysis are that: (i) we have considered the effect of the *angular size* of the dSphs for the first time. This is important since, while nearby dSphs have higher γ-ray flux, their larger angular extent can make them subprime targets if the sensitivity is limited by cosmic-ray and γ-ray backgrounds; (ii) we have determined the astrophysical J-factor for the classical dSphs directly from photometric and kinematic data. We have assumed very little about their underlying DM distribution, modelling the dSph DM profile as a smooth split power law, both with and without DM subclumps; (iii) we have used a MCMC technique to marginalize over unknown parameters and determined the sensitivity of our derived J-factors to both model and measurement uncertainties; and (iv) we have used simulated DM profiles to demonstrate that our J-factor determinations recover the correct solution within our quoted uncertainties.

Our key findings are as follows:

(i) Subclumps in the dSphs do *not* usefully boost the signal. For all configurations where the subclump distribution follows the underlying smooth DM halo, the boost factor is at most $\sim$2–3. Moreover, to obtain even this mild boost, one has to integrate the signal over the whole angular extent of the dSph. This is unlikely to be an effective strategy as the diffuse Galactic DM signal will dominate for integration angles $\alpha_{\rm int} \gtrsim 1^\circ$.

[17] In particular, there is a bright GeV emitter 1FGL J0058.4−3235 only $\sim$1.°1 away from Sculptor which significantly worsens the upper limit on that object as discussed by Abdo et al. (2010).

(ii) Point-like emission from a dSph is a very poor approximation for high-angular-resolution instruments, such as the next-generation CTA. For a nearby dSph, using the point-like approximation can lead to an order of magnitude overestimate of the detection sensitivity. In the case of a nearby cored profile consisting of very high mass DM particles, a point-source approximation can be unsatisfactory even for the modest angular resolution of the *Fermi*-LAT.

(iii) With the Jeans analysis, no DM profile can be ruled out by current data. The use of the MCMC technique on artificial data also shows that such an analysis is unable to provide reliable values for J if the profiles are cuspy ($\gamma = 1.5$). However, using a prior on the inner DM cusp slope $0 \leq \gamma_{\rm prior} \leq 1$ provides J-factor estimates accurate to a factor of a few.

(iv) The best dSph targets are not simply those closest to us, as might naïvely be expected. A good candidate has to combine high mass, close proximity, small angular size ($\lesssim 1^\circ$; i.e. not too close), and a well-constrained DM profile. With these criteria in mind, we find three categories: well constrained and promising (Ursa Minor, Sculptor and Draco), well constrained but less promising (Carina, Fornax and Leo I), and poorly constrained (Sextans and Leo II). Leo II may yet prove to be a viable target as it has a larger median J-factor than Ursa Minor; however, more data are required to confirm its status.

(v) A search based on a known DM candidate (from e.g. forthcoming discoveries at the LHC) will do much to optimize the search strategy and, ultimately, the detection sensitivity for all γ-ray observatories. This is because the shape of the annihilation spectrum is a strong driver of the photon energy range that can provide the best information on the candidate DM particle mass. The *Fermi*-LAT has great potential to probe down to the expected annihilation cross-section for particles of mass $\ll 700$ GeV, whereas a ground-based instrument is more suited for probing particle masses above a few hundred GeV with a sufficiently deep exposure. However, even for 5 years of observation with the *Fermi*-LAT or 100 hours with the FCA, the sensitivity reach (Fig. 17) remains anywhere between 4 and 10 orders of magnitude above the expected annihilation cross-section for a cosmological relic (depending on the mass of the DM particle candidate). Improving these limits will require a harder annihilation spectrum than the conservative average we have adopted in this study, or a significant boost (e.g. from the Sommerfeld enhancement) to the γ-ray production.

Finally, the ultrafaint dSphs have received a lot of interest in the community lately, as they could be the most DM dominated systems in the Galaxy. We emphasize that the MCMC analysis we have performed for the classical dSphs cannot be applied 'as is' for these objects. First, the sample of stars observed is smaller. Secondly, the velocity dispersion is smaller and suffers from larger uncertainties than those for the classical dSphs. The robustness and systematic biases of the MCMC analysis will be discussed elsewhere (Walker et al., in preparation). Results concerning J for the ultrafaint dSphs will be presented in a companion paper.

ACKNOWLEDGMENTS

We thank the anonymous referee for careful reading of the manuscript and useful comments. We thank Walter Dehnen for providing his code for use in generating artificial dSph data sets. MGW is supported by NASA through Hubble Fellowship grant HST-HF-51283, awarded by the Space Telescope Science Institute, which is operated by the Association of Universities for Research in Astronomy, Inc., for NASA, under contract NAS 5-26555. CC

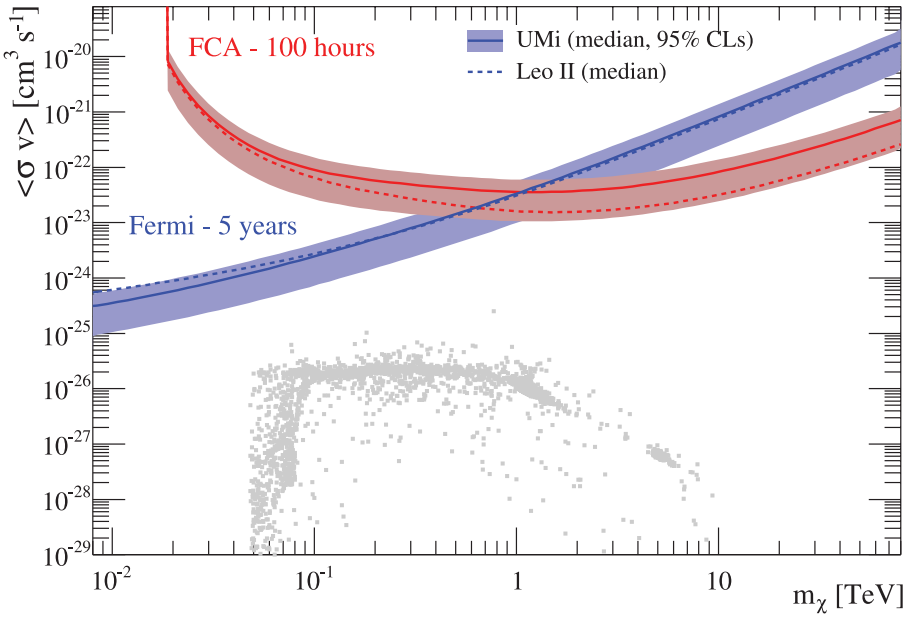

Figure 17. Sensitivity reach in the m_χ–$\langle\sigma v\rangle$ plane for the FCA (100 hours) and *Fermi* (5 years), for our best candidates – Ursa Minor (median value and 95 per cent CIs) and Leo II (median only). The black asterisks represent points from MSSMs that fall within three standard deviations of the relic density measured in the 3-year *WMAP* data set (taken from Acciari et al. 2010).

acknowledges support from an STFC rolling grant at the University of Leicester. JAH acknowledges the support of an STFC Advanced Fellowship. MIW acknowledges the Royal Society for support through a University Research Fellowship. JIR acknowledges support from SNF grant PP00P2_128540/1. SS acknowledges support by the EU Research & Training Network 'Unification in the LHC era' (PITN-GA-2009-237920). Part of this work used the ALICE High Performance Computing Facility at the University of Leicester. Some resources on ALICE form part of the DiRAC Facility jointly funded by the STFC and Large Facilities Capital Fund of BIS.

REFERENCES

Abdo A. A. et al., 2010, ApJ, 712, 147
Abramowski A. et al., 2011a, Astropart. Phys., 34, 608
Abramowski A. et al., 2011b, Phys. Rev. Lett., 106, 161301
Acciari V. A. et al., 2010, ApJ, 720, 1174
AGIS Collaboration, 2010, Advanced Gamma-ray Imaging System
Aharonian F. et al., 2004, A&A, 425, L13
Albert J. et al., 2008, ApJ, 679, 428
Amorisco N. C., Evans N. W., 2011, MNRAS, 411, 2118
An J. H., Evans N. W., 2006, ApJ, 642, 752
Battaglia G., Helmi A., Tolstoy E., Irwin M., Hill V., Jablonka P., 2008, ApJ, 681, L13
Berezinsky V. S., Gurevich A. V., Zybin K. P., 1992, Phys. Lett. B, 294, 221
Berge D., Funk S., Hinton J., 2007, A&A, 466, 1219
Bergström L., Hooper D., 2006, Phys. Rev. D, 73, 063510
Bergström L., Ullio P., 1997, Nucl. Phys. B, 504, 27
Bergström L., Ullio P., Buckley J. H., 1998, Astropart. Phys., 9, 137
Bernlöhr K., Carmona E., Schweizer T., 2008, in Caballero R., D'Olivo J. C., Medina-Tanco G., Nellen L., Sánchez F. A., Valdés-Galicia J.é F., eds, MC Simulation and Layout Studies for a Future Cherenkov Telescope Array. Universidad Nacional Autónoma de México, Mexico City, Mexico, p. 1469
Bertone G., Hooper D., Silk J., 2005, Phys. Rep., 405, 279
Binney J., Tremaine S., 2008, Galactic Dynamics, 2nd edn. Princeton Univ. Press, Princeton, NJ (BT08)
Boyarsky A., Neronov A., Ruchayskiy O., Shaposhnikov M., Tkachev I., 2006, Phys. Rev. Lett., 97, 261302
Bringmann T., Bergström L., Edsjö J., 2008, J. High Energy Phys., 1, 49
Bringmann T., Doro M., Fornasa M., 2009, J. Cosmol. Astropart. Phys., 1, 16
Bullock J. S., Kolatt T. S., Sigad Y., Somerville R. S., Kravtsov A. V., Klypin A. A., Primack J. R., Dekel A., 2001, MNRAS, 321, 559 (B01)
Cannoni M., Gómez M. E., Sánchez-Conde M. A., Prada F., Panella O., 2010, Phys. Rev. D, 81, 107303
Charbonnier A., Combet C., Maurin D., 2011, Comp. Phys. Comm., submitted
Cole D., Dehnen W., Wilkinson M., 2011, MNRAS, 416, 1118
CTA Consortium, 2010, preprint (arXiv:1008.3703)
Cuddeford P., 1991, MNRAS, 253, 414
de Blok W. J. G., 2010, Adv. Astron., 2010, 789293
Dehnen W., 1993, MNRAS, 265, 250
Diemand J., Moore B., Stadel J., 2005, Nat, 433, 389
Diemand J., Kuhlen M., Madau P., Zemp M., Moore B., Potter D., Stadel J., 2008, Nat, 454, 735
Essig R., Sehgal N., Strigari L. E., 2009, Phys. Rev. D, 80, 023506
Evans N. W., Ferrer F., Sarkar S., 2004, Phys. Rev. D, 69, 123501
Fermi-LAT Collaboration, 2010, LAT Performance
Fornengo N., Pieri L., Scopel S., 2004, Phys. Rev. D, 70, 103529
Funk S., Reimer O., Torres D. F., Hinton J. A., 2008, ApJ, 679, 1299
Goerdt T., Moore B., Read J. I., Stadel J., Zemp M., 2006, MNRAS, 368, 1073
Goerdt T., Moore B., Read J. I., Stadel J., 2010, ApJ, 725, 1707
Governato F. et al., 2010, Nat, 463, 203
Gunn J. E., Lee B. W., Lerche I., Schramm D. N., Steigman G., 1978, ApJ, 223, 1015
Hargreaves J. C., Gilmore G., Annan J. D., 1996, MNRAS, 279, 108
Hastings W. K., 1970, Biometrika, 57, 97
Hernquist L., 1990, ApJ, 356, 359
Hisano J., Matsumoto S., Nojiri M. M., 2004, Phys. Rev. Lett., 92, 031303
Hisano J., Matsumoto S., Nojiri M. M., Saito O., 2005, Phys. Rev. D, 71, 063528
Hogan C. J., Dalcanton J. J., 2000, Phys. Rev. D, 62, 063511
Horns D., 2005, Phys. Lett. B, 607, 225

Irwin M., Hatzidimitriou D., 1995, MNRAS, 277, 1354
Ishiyama T., Makino J., Ebisuzaki T., 2010, ApJ, 723, L195
Jungman G., Kamionkowski M., Griest K., 1996, Phys. Rep., 267, 195
King I., 1962, AJ, 67, 471
Kleyna J. T., Wilkinson M. I., Gilmore G., Evans N. W., 2003, ApJ, 588, L21
Koch A., Wilkinson M. I., Kleyna J. T., Gilmore G. F., Grebel E. K., Mackey A. D., Evans N. W., Wyse R. F. G., 2007, ApJ, 657, 241
Kuhlen M., 2010, Adv. Astron., 2010, 162083
Kuhlen M., Diemand J., Madau P., 2008, ApJ, 686, 262
Lake G., 1990, Nat, 346, 39
Lavalle J., Yuan Q., Maurin D., Bi X., 2008, A&A, 479, 427
Lewis A., Bridle S., 2002, Phys. Rev. D, 66, 103511
McConnachie A. W., Côté P., 2010, ApJ, 722, L209
Mamon G. A., Łokas E. L., 2005, MNRAS, 363, 705
Martinez G. D., Bullock J. S., Kaplinghat M., Strigari L. E., Trotta R., 2009, J. Cosmol. Astropart. Phys., 6, 14
Mashchenko S., Wadsley J., Couchman H. M. P., 2008, Sci, 319, 174
Mateo M. L., 1998, ARA&A, 36, 435
Mateo M., Olszewski E. W., Walker M. G., 2008, ApJ, 675, 201
Merritt D., Graham A. W., Moore B., Diemand J., Terzić B., 2006, AJ, 132, 2685
Metropolis A. W., Rosenbluth M. N., Teller A. H., Teller E., 1953, J. Chem. Phys., 21, 1087
Moore B., Gelato S., Jenkins A., Pearce F. R., Quilis V., 2000, ApJ, 535, L21
Navarro J. F., Frenk C. S., White S. D. M., 1996a, ApJ, 462, 563
Navarro J. F., Eke V. R., Frenk C. S., 1996b, MNRAS, 283, L72
Navarro J. F., Frenk C. S., White S. D. M., 1997, ApJ, 490, 493
Olszewski E. W., Pryor C., Armandroff T. E., 1996, AJ, 111, 750
Palomares-Ruiz S., Siegal-Gaskins J. M., 2010, J. Cosmol. Astropart. Phys., 7, 23
Pieri L., Bertone G., Branchini E., 2008, MNRAS, 384, 1627
Pieri L., Pizzella A., Corsini E. M., Dalla Bontà E., Bertola F., 2009a, A&A, 496, 351
Pieri L., Lattanzi M., Silk J., 2009b, MNRAS, 399, 2033
Plummer H. C., 1911, MNRAS, 71, 460
Putze A., Derome L., Maurin D., Perotto L., Taillet R., 2009, A&A, 497, 991
Read J. I., Gilmore G., 2005, MNRAS, 356, 107
Sánchez-Conde M. A., Prada F., Łokas E. L., Gómez M. E., Wojtak R., Moles M., 2007, Phys. Rev. D, 76, 123509
Sérsic J. L., 1968, Atlas de Galaxias Australes. Observatorio Astronomico, Cordoba, Argentina
Silk J., Bloemen H., 1987, ApJ, 313, L47
Springel V. et al., 2008, MNRAS, 391, 1685
Stecker F. W., 1978, ApJ, 223, 1032
Strigari L. E., Bullock J. S., Kaplinghat M., Diemand J., Kuhlen M., Madau P., 2007a, ApJ, 669, 676
Strigari L. E., Koushiappas S. M., Bullock J. S., Kaplinghat M., 2007b, Phys. Rev. D, 75, 083526
Strigari L. E., Bullock J. S., Kaplinghat M., Simon J. D., Geha M., Willman B., Walker M. G., 2008, Nat, 454, 1096
Strigari L. E., Frenk C. S., White S. D. M., 2010, MNRAS, 408, 2364
Ullio P., Bergström L., 1998, Phys. Rev. D, 57, 1962
Valkenburg W., Krauss L. M., Hamann J., 2008, Phys. Rev. D, 78, 063521
Walker M. G., Mateo M., Olszewski E. W., Gnedin O. Y., Wang X., Sen B., Woodroofe M., 2007, ApJ, 667, L53
Walker M. G., Mateo M., Olszewski E. W., Peñarrubia J., Wyn Evans N., Gilmore G., 2009a, ApJ, 704, 1274 (W09)
Walker M. G., Mateo M., Olszewski E. W., Sen B., Woodroofe M., 2009b, AJ, 137, 3109
Walker M. G., Mateo M., Olszewski E. W., 2009c, AJ, 137, 3100
Walker M. G., Combet C., Hinton J., Maurin D., Wilkinson M. I., 2011, ApJ, 733, L46
Wolf J., Martinez G. D., Bullock J. S., Kaplinghat M., Geha M., Muñoz R. R., Simon J. D., Avedo F. F., 2010, MNRAS, 406, 1220
Zhao H., 1996, MNRAS, 278, 488

APPENDIX A: DEFINITIONS, NOTATIONS AND CONVERSION FACTORS

Studies of DM annihilations in the context of dSphs involve both particle physics and astrophysics. The obvious difference of scales between the two fields and habits among the two communities have given rise to a plethora of notations and unit choices throughout the literature. In this appendix, we provide some explanatory elements and conversion factors to ease comparison between the different works published on the subject.

As mentioned in Section 2, we define the differential γ-ray flux as integrated over the solid angle $\Delta\Omega$ as

$$\frac{\mathrm{d}\Phi_\gamma}{\mathrm{d}E_\gamma}(E_\gamma, \Delta\Omega) = \Phi^{\mathrm{pp}}(E_\gamma) \times J(\Delta\Omega)\,,$$

where

$$\Phi^{\mathrm{pp}}(E_\gamma) \equiv \frac{\mathrm{d}\Phi_\gamma}{\mathrm{d}E_\gamma} = \frac{1}{4\pi}\frac{\langle\sigma_{\mathrm{ann}}v\rangle}{2m_\chi^2}\frac{\mathrm{d}N_\gamma}{\mathrm{d}E_\gamma}$$

and

$$J(\Delta\Omega) = \int_{\Delta\Omega}\int \rho^2_{\mathrm{DM}}(l,\Omega)\,\mathrm{d}l\,\mathrm{d}\Omega\,.$$

The solid angle is simply related to the integration angle α_{int} by

$$\Delta\Omega = 2\pi[1-\cos(\alpha_{\mathrm{int}})]\,.$$

In our work, the units of these quantities are as follows:

(i) $\mathrm{d}\Phi_\gamma/\mathrm{d}E_\gamma = \mathrm{cm}^{-2}\,\mathrm{s}^{-1}\,\mathrm{GeV}^{-1}$;
(ii) $\Phi^{\mathrm{pp}}(E_\gamma) = \mathrm{cm}^3\,\mathrm{s}^{-1}\,\mathrm{GeV}^{-3}\,(\mathrm{sr}^{-1})$;
(iii) $J = \mathrm{M}^2_\odot\,\mathrm{kpc}^{-5}\,(\mathrm{sr})$.

First of all, note that the location of the $1/4\pi$ factor appearing in Φ^{pp} is arbitrary. We followed Pieri et al. (2009a) and included it in the particle physics factor. In other works, it can appear in the astrophysical factor J (e.g. Bringmann et al. 2009). Therefore, to compare the astrophysical factors between several studies, one must first ensure to correct the value of J by 4π if needed. In the text, we did not explicitly state the solid angle dependence in units of J as it is a dimensionless quantity.[18] The conversion factors (once the 4π issue is resolved) from our J units to those traditionally found in the literature are as follows:

(i) $1\,\mathrm{M}^2_\odot\,\mathrm{kpc}^{-5} = 10^{-15}\,\mathrm{M}^2_\odot\,\mathrm{pc}^{-5}$
(ii) $1\,\mathrm{M}^2_\odot\,\mathrm{kpc}^{-5} = 4.45\times10^6\,\mathrm{GeV}^2\,\mathrm{cm}^{-5}$
(iii) $1\,\mathrm{M}^2_\odot\,\mathrm{kpc}^{-5}\,(\mathrm{sr}) = 1.44\times10^{-15}\,\mathrm{GeV}^2\,\mathrm{cm}^{-6}\,\mathrm{kpc}\,(\mathrm{sr})$

Before comparing any number, one must also ensure that the solid angle $\Delta\Omega$ over which the integration is performed is the same. In most works, an $\alpha_{\mathrm{int}} = 0.^\circ1$ angular resolution is chosen, corresponding to $\Delta\Omega = 10^{-5}$ sr. However, this is not always the case, as in this study we explore several angular resolutions. Note that the quantity $\bar{J} \equiv J/\Delta\Omega$ (in $\mathrm{GeV}^2\,\mathrm{cm}^{-5}\,\mathrm{sr}^{-1}$, for example) is also in use and the astrophysical factor can be found under this form in some papers (e.g. Evans et al. 2004).

APPENDIX B: TOY MODEL FOR J (IN DSPHS)

The volume of the dSph is not always fully encompassed in the integration solid angle, as sketched in Fig. B1 (vertical hatched

[18] Some authors do, however, explicitly express the solid angle dependence in their units, for example, Pieri et al. (2009a), who express J (Φ_{cosmo} in their notation) in $\mathrm{GeV}^2\,\mathrm{cm}^{-6}\,\mathrm{kpc}\,\mathrm{sr}$. This is completely equivalent to our $\mathrm{M}^2_\odot\,\mathrm{kpc}^{-5}$ but for the unit numerical conversion factor.

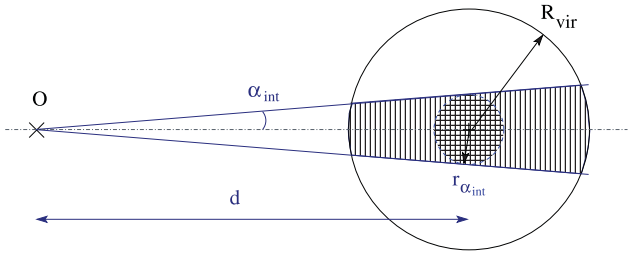

Figure B1. Sketch of the integration regions contributing to the J-factor: shown are the full integration region (vertical hatched) or a subregion (cross-hatched) used for the toy calculations. The letter O shows the observer position, $\alpha_{\rm int}$ is the integration angle, d is the distance from the dSph and $R_{\rm vir}$ is its virial radius.

region) so that a numerical integration is required in general.

However, a reasonable approximation for estimating the dependence of J on the parameters of the problem, that is, the distance from the dSph d, the integration angle $\alpha_{\rm int}$, and the profile parameters $\rho_{\rm s}$, $r_{\rm s}$ and γ, is to consider only the volume within the radius

$$r_{\alpha_{\rm int}} = d \times \sin(\alpha_{\rm int}) \approx d \times \alpha_{\rm int}, \tag{B1}$$

where the approximation is valid for typical integration angles $\alpha_{\rm int} \lesssim 0.^\circ 1$. This volume corresponds to the spherical cross-hatched region in Fig. B1.

The toy model proposed below to calculate J allows us to cross-check the results of the numerical integration for both the smooth and the subclump contributions. We find that the model is accurate enough up to a factor of 2 for $\gamma = 0$ and $\gamma > 0.5$, so can be used for gross estimates of any signal from a DM clump.

B1 For the smooth distribution

About 90 per cent of the clump luminosity is usually contained in a few $r_{\rm s}$, whatever the profile. The consequences are twofold: first, as can be read off Table 2, $r_{\rm s}/d \ll 1$, so that the J-factor amounts to a point-like contribution

$$J_{\rm point\text{-}like} = \frac{4\pi}{d^2} \int_0^{\min(r_{\alpha_{\rm int}}, r_{\rm s})} r^2 \rho^2(r) {\rm d}r. \tag{B2}$$

Secondly, it means that equation (6) for the profile can be simplified into the approximate expression

$$\rho_{\rm approx}(r) = \begin{cases} \rho_{\rm sat} & \text{if } r \le r_{\rm sat}; \\ \rho_{\rm s} \times \left(\dfrac{r}{r_{\rm s}}\right)^{-\gamma} & \text{if } r_{\rm sat} < r \le r_{\rm s}; \\ 0 & \text{otherwise.} \end{cases} \tag{B3}$$

However, for all applications of our toy model, we will keep $\gamma < 3/2$, so that the saturation density above is never reached in the dSphs considered below.

Various regimes. The approximate formulae for J are obtained by combining equations (B2) and (B3):

$$J_{\rm approx} = \frac{4\pi}{d^2} \int_0^{\min(r_{\alpha_{\rm int}}, r_{\rm s})} r^2 \rho^2_{\rm approx}(r) {\rm d}r. \tag{B4}$$

Using equation (B1), this leads to

$$J_{\rm approx} = \frac{4\pi}{d^2} \frac{\rho_{\rm s}^2 r_{\rm s}^{2\gamma}}{3-2\gamma} [\min(r_{\alpha_{\rm int}}, r_{\rm s})]^{3-2\gamma}. \tag{B5}$$

This formula gives satisfactory results for cuspy profiles (see below), but has to be modified in the following cases:

(i) If $r_{\alpha_{\rm int}} \gtrsim r_{\rm s}$, the integration region encompasses $r_{\rm s}$. The (1, 3, γ) profiles decrease faster than $r^{-\gamma}$ for $r \sim r_{\rm s}$; hence, integrating the toy model up to $r_{\rm s}$ is bound to overshoot the true result. We thus stop the integration at the radius r_x such that $\rho_{\rm true}(r_x) = \rho_{\rm approx}(r_x)/x$, that is,

$$r_x = r_{\rm s}[x^{1/(3-\gamma)} - 1].$$

Taking $x = 2$ gives a satisfactory fit to the full numerical calculation (see below).

(ii) If $r_{\alpha_{\rm int}} \gtrsim r_{\rm s}$ and $\gamma = 0$, the integration can be performed analytically up to $R_{\rm vir}$ and is used instead.

(iii) If $r_{\alpha_{\rm int}} \lesssim r_{\rm s}$ and $\gamma = 0$, the profile is constant, and integrating on the cross-hatched region (instead of the vertical hatched one, see Fig. B1) undershoots the true result. A better approximation is to integrate on a conic section. For the same reason as given for the first item, we replace $r_{\rm s}$ by r_x (with $x = 2$) in the calculation of the cone volume.

Resulting formula. To summarize, the final toy-model formula proposed for the smooth contribution of the dSph is

$$J_{\rm toy} = \frac{4\pi\rho_{\rm s}^2}{d^2} \times \begin{cases} r_{\rm s}^{2\gamma} \dfrac{\min(r_x, r_{\alpha_{\rm int}})^{3-2\gamma}}{3-2\gamma} & \text{if } \gamma > 0; \\ [I(r_{\alpha_{\rm int}}) - I(0)] & \text{if } \gamma = 0,\ r_{\alpha_{\rm int}} > r_x; \\ \dfrac{r_{\alpha_{\rm int}}^2 r_{\rm s}}{2} & \text{if } \gamma = 0,\ r_{\alpha_{\rm int}} < r_x; \end{cases} \tag{B6}$$

where

$$\begin{aligned} r_{\alpha_{\rm int}} &= \alpha_{\rm int} d, \\ r_x &= r_{\rm s}[x^{1/(3-\gamma)} - 1], \\ I(x) &= -r_{\rm s}^6(r_{\rm s}^2 + 5r_{\rm s}x + 10x^2)/[30(r_{\rm s}+x)^5]. \end{aligned} \tag{B7}$$

Toy model versus numerical integration. Finally, we check the validity of this toy model by confronting it with the full numerical integration. Various inner slopes γ of the profile are considered, as provided in Table 1. Defining the critical distance $d_{\rm crit}$ for which the dSph is fully encompassed by the integration region, that is,

$$d_{\rm crit} = \frac{r_{\rm s}}{\alpha_{\rm int}},$$

we find $d_{\rm crit} \sim 50$ and 500 kpc for $r_{\rm s} = 0.1$ and 1 kpc, respectively (the integration range is $\alpha_{\rm int} = 0.^\circ 1$). If r_x is used instead of $r_{\rm s}$, this distance is even smaller. This allows us to test the toy model for the two regimes. The result is shown in Fig. B2. The symbols show the full numerical integration, while the lines show the toy-model calculations.

For profiles steeper than 0.5, the agreement is better than a factor of 2 for all distances. For flatter profiles, the toy model only gives results within an order of magnitude. However, for $\gamma = 0$, the fix applied to the toy model allows to regain the correct results within a factor of 2.

Hence, given the current uncertainties on the profiles, the set of formulae (B7) and (B7) can safely be used for quick inspection of the J value of any profile with an inner slope γ of 0, or greater than 0.5.

B2 For the subclump distribution

The influence of DM substructures on the γ-ray production has been widely discussed in the literature. These substructures may enhance the detectability by boosting the γ-ray signal. In this appendix, we

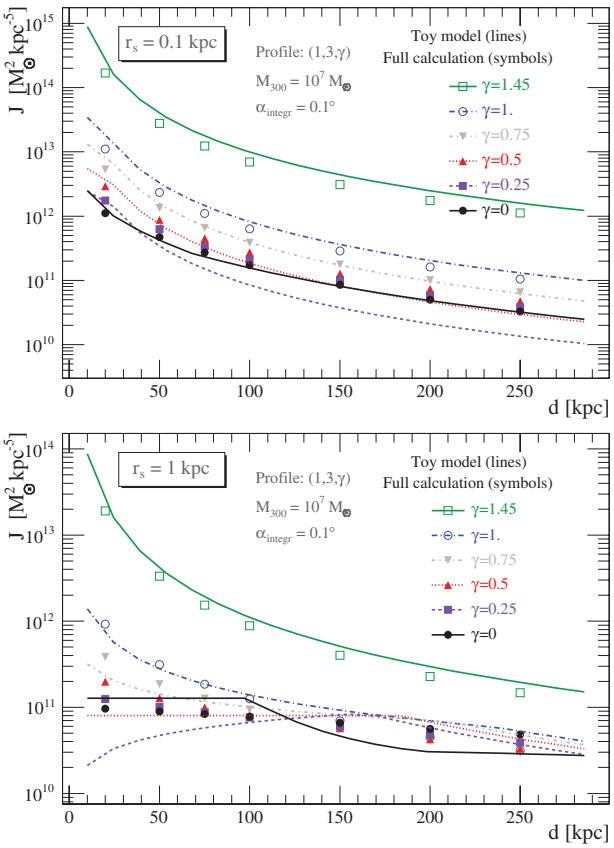

Figure B2. Toy-model calculation (lines) versus full numerical integration (symbols) of J as a function of the distance from the dSph. The integration angle is fixed to $\alpha_{\rm int} = 0.^\circ 1$ and the $(1, 3, \gamma)$ profiles are taken to vary from $\gamma = 0$ to 1.45. For each model, $\rho_{\rm s}$ is calculated such as to provide $M_{300} = 10^7\,{\rm M}_\odot$. Top panel: dSphs for which $r_{\rm s} = 0.1$ kpc. Bottom panel: dSphs for which $r_{\rm s} = 1$ kpc.

give an analytical estimation of the effect of subclumps in dSph spheroidal galaxies, in the same spirit as the toy model developed in the previous section for the smooth component. For simplicity, we restrict ourselves to one cored $(\alpha, \beta, \gamma) = (1, 3, 0)$ and one cusped (1, 3, 1) profile. To characterize the clump distribution, we use the formalism given in Lavalle et al. (2008).

Substructure distribution. The clump spatial distribution is assumed to follow the dSph DM profile, namely

$$\frac{{\rm d}P(r)}{{\rm d}V} \propto \left(\frac{r}{r_{\rm s}}\right)^{-\gamma} \left[1 + \left(\frac{r}{r_{\rm s}}\right)^{-\alpha}\right]^{\frac{\gamma-\beta}{\alpha}} . \tag{B8}$$

The mass distribution of the clumps is taken to be independent of the spatial distribution and takes the usual form

$$\frac{{\rm d}P}{{\rm d}M} = AM^{-a} , \tag{B9}$$

with $M \in [M_{\rm min}, M_{\rm max}]$ and $a \sim 1.9$ from cosmological N-body simulations (A is the normalization constant for ${\rm d}P/{\rm d}M$ to be a probability).

Clump luminosity. Defining L_i, the *intrinsic luminosity* of the subclump i, to be

$$L_i \equiv \int_{V_{\rm cl}} \rho^2 {\rm d}V , \tag{B10}$$

the astrophysical contribution to the γ-ray flux from the substructures of the dSph is

$$J_{\rm clumps} = \frac{1}{d^2} \sum_{i=1}^{N^{\rm cl}} L_i , \tag{B11}$$

where $N^{\rm cl}$ is the number of clumps contained within the integration angle α and d is the distance from the dSph. The luminosity depends only on the mass of the clump, once a concentration–mass ($c_{\rm vir}$–$M_{\rm vir}$) relationship is chosen (see e.g. Lavalle et al. 2008, and references therein), so that $L_i = L(M_i)$. Moving to the continuous limit, equation (B11) reads

$$J_{\rm clumps} = \frac{1}{d^2} N^{\rm cl} \int_{M_{\rm min}}^{M_{\rm max}} L(M) \frac{{\rm d}P}{{\rm d}M} {\rm d}M . \tag{B12}$$

Fitting the results from Lavalle et al. (2008), the intrinsic luminosity[19] varies almost linearly with the mass of the clump as

$$L^{\rm NFW}(M) = 1.17 \times 10^8 (M/{\rm M}_\odot)^{0.91}\,{\rm M}_\odot^2\ {\rm kpc}^{-3}, \tag{B13}$$

so we have

$$J_{\rm clumps} = \frac{N^{\rm cl} A}{d^2} \left(\frac{1.17 \times 10^8}{1.91 - a}\right) \left(M_{\rm max}^{1.91-a} - M_{\rm min}^{1.91-a}\right) . \tag{B14}$$

Number of clumps. The fraction F of clumps in the spherical integration region $r_{\alpha_{\rm int}} \approx \alpha_{\rm int} d$ (cross-hatched region in Fig. B1) is given by

$$F = \frac{N^{\rm cl}}{N^{\rm cl}_{\rm tot}} = \int_0^{r_{\alpha_{\rm int}}} 4\pi r^2 \frac{{\rm d}P}{{\rm d}V} {\rm d}r , \tag{B15}$$

where $N^{\rm cl}_{\rm tot}$ is the total number of clumps within the dSph. Upon integration and defining $x_{\rm int} = r_{\alpha_{\rm int}}/r_{\rm s}$ and $x_{\rm vir} = R_{\rm vir}/r_{\rm s}$, this becomes

$$F_{\rm core} = \left[\frac{4x_\alpha + 3}{2(x_\alpha + 1)^2} + \ln(x_\alpha + 1) - \frac{3}{2}\right] \times \left[\frac{4x_{\rm vir} + 3}{2(x_{\rm vir} + 1)^2} + \ln(x_{\rm vir} + 1) - \frac{3}{2}\right]^{-1} \quad \text{for } (1, 3, 0) \tag{B16}$$

and

$$F_{\rm cusp} = \left[\frac{1}{(x_\alpha + 1)} + \ln(x_\alpha + 1) - 1\right] \times \left[\frac{1}{(x_{\rm vir} + 1)} + \ln(x_{\rm vir} + 1) - 1\right]^{-1} \quad \text{for NFW.} \tag{B17}$$

Some care is necessary when evaluating the number of clumps $N^{\rm cl} = F \times N^{\rm cl}_{\rm tot}$ in the integration region. Whatever the profile, most of the clumps are located within $r_{\rm s}$ so when $r_{\alpha_{\rm int}} > r_{\rm s}$, the spherical integration region of our toy model (cross-hatched region in Fig. B1) is a good enough approximation, and equations (B16) and (B17) hold. However, if $r_{\alpha_{\rm int}} < r_{\rm s}$, then the remainder of the intersecting cone (vertically hatched region in Fig. B1) could amount to a significant contribution to the number of clumps. Cuspy distributions should only be marginally affected, given their high central concentration. However, this effect may be important for cored profiles. Whenever $r_{\alpha_{\rm int}} < r_{\rm s}$, as for the smooth contribution, equation (B16) is therefore multiplied by the ratio of the intersecting cone volume to the integration sphere volume, in order to account for that effect.

If the mass of the dSph is $M_{\rm vir}$ and assuming a fraction f of this mass is in the form of clumps, one gets using equation (B9)

$$N^{\rm cl}_{\rm tot} = f\ \frac{2 - a}{A} M_{\rm vir} \left(M_{\rm max}^{2-a} - M_{\rm min}^{2-a}\right)^{-1} .$$

[19] In this toy model, we limit ourselves to the NFW profiles for the subclumps in the dSph, and a $c_{\rm vir}$–$M_{\rm vir}$ relation taken from B01.

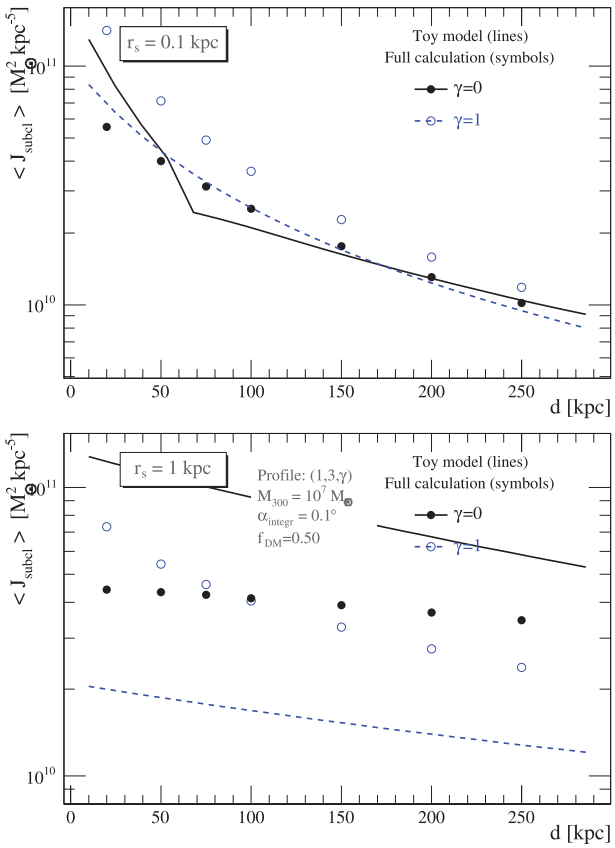

Figure B3. Toy-model calculation (lines) versus full numerical integration (symbols) of J as a function of the distance from the dSph. The integration angle is fixed to $\alpha_{\rm int} = 0.^\circ 1$ and the two $(1, 3, \gamma)$ subclump spatial distributions are $\gamma = 0$ and 1 (their inner profile is a NFW with a $c_{\rm vir}$–$M_{\rm vir}$ relation taken from B01). The calculations assume the fraction of DM in subclumps to be $f = 50$ per cent of the total mass of the dSphs, where the smooth profile is taken as in Fig. B2. Top panel: $r_{\rm s} = 0.1$ kpc. Bottom panel: $r_{\rm s} = 1$ kpc.

Resulting formulae. Adding all ingredients together, the contribution of the substructures to the flux is

$$J_{\rm clumps} = 1.17 \times 10^8 \frac{F_{\rm core/cusp}}{d^2} \left(\frac{2-a}{1.91-a} \right) \times \left(\frac{M_{\rm max}^{1.91-a} - M_{\rm min}^{1.91-a}}{M_{\rm max}^{2-a} - M_{\rm min}^{2-a}} \right) f M_{\rm vir} \, . \quad \text{(B18)}$$

Toy model versus numerical integration. The comparison between the two is shown in Fig. B3. The symbols show the full numerical integration, while the lines show the toy-model calculations.

For $r_{\rm s} = 100$ pc, the agreement is better than a factor of 2 for all distances. For $r_{\rm s} = 1$ kpc, the toy model only gives results correct to within a factor of 4 for $\gamma = 1$.

Hence, given the current uncertainties on the profiles, equation (B18) can be used for quick inspection of the J value for the subclump contribution.

APPENDIX C: DISTANCE AND INTEGRATION ANGLE DEPENDENCE ON J FOR GENERIC DSPHS

This appendix completes the study of the J-factor dependences started in Section 2.3. All the plots and discussions below rely on the generic profiles given in Table 1, and the substructure reference configuration given in Section 2.2.3.

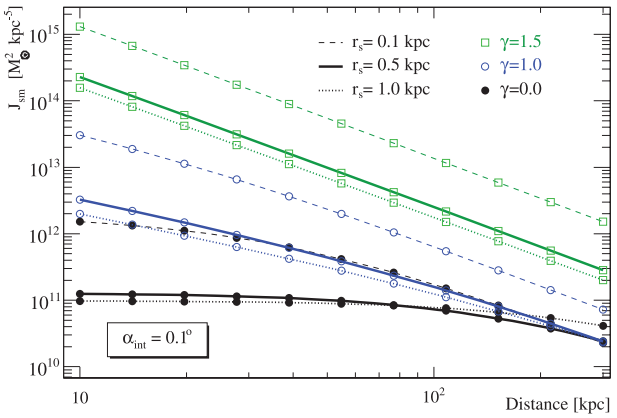

Figure C1. $J_{\rm sm}(\theta = 0)$ as a function of the distance from the dSph for three profiles γ and three values of $r_{\rm s}$. The corresponding values for $\rho_{\rm s}$ are given in Table 1.

C1 Distance dependence $J(d)$

Fig. C1 shows $J_{\rm sm}$ as a function of the distance from the dSph (we assume $\alpha_{\rm int} = 0.^\circ 1$ here and that we are pointing towards the dSph centre, that is, $\theta = 0$). As we have checked earlier, the subclump contribution for the reference model at $\theta = 0$ is always subdominant, so for clarity only $J_{\rm sm}$ is displayed ($f = 0$) in the figure.

If the angular size of the signal is smaller than the integration angle, the distance dependence is expected to be $J_{\rm sm} \propto d^{-2}$. This is the case for $\gamma = 1.5$ for any value of $r_{\rm s}$ (hollow squares curves). Actually, the three curves follow the point-like source toy formula (B6) appropriate for steep γ, that is,

$$J(\theta = 0) \propto \rho_{\rm s}^2 \times \frac{r_{\rm s}^3}{d^2} \, . \quad \text{(C1)}$$

However, when the angular size of the emitting region becomes larger than the integration angle, the above relationship fails. As most of the flux is emitted within $r_{\rm s}$, this happens for a critical distance

$$d_{\rm crit} \approx \frac{r_{\rm s}}{\alpha_{\rm int}} \, . \quad \text{(C2)}$$

For $r_{\rm s} = 0.1$ kpc, this corresponds to $d_{\rm crit} \approx 60$ kpc (see the full circles dashed curve for $\gamma = 0$). Having a dSph closer than this critical distance does not increase further the signal (see e.g. the solid and dotted full circles curves for $\gamma = 0$ and $r_{\rm s} \gtrsim 0.5$ kpc). In the latter case, taking a larger integration region is not always the best strategy as, from an experimental point of view, a larger integration region increases not only the signal but also the background. In this case, the gain in sensitivity from having a dSph close by is not as important as what might naïvely be expected from the point-like approximation (see Section 3).

C2 Integration angle dependence $J(\alpha_{\rm int})$

We recall that $\int_{\Delta\Omega} {\rm d}\Omega = \int_0^{2\pi} {\rm d}\beta_{\rm int} \int_0^{\alpha_{\rm int}} \sin(\alpha_{\rm int}) {\rm d}\alpha_{\rm int}$, where $\Delta\Omega = 2\pi[1 - \cos(\alpha_{\rm int})]$, so that the J-factor from equation (5) can be rewritten in the symbolic notation

$$J(\psi, \theta, \Delta\Omega) = \int_0^{2\pi} F_{[\beta_{\rm int}]} \, {\rm d}\beta_{\rm int} \quad \text{(C3)}$$

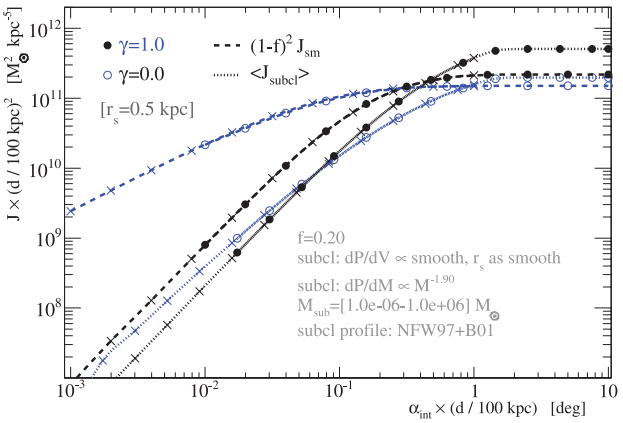

Figure C2. $J \times (d/100\,\mathrm{kpc})^2$ as a function of $\alpha_{\rm int} \times (d/100\,\mathrm{kpc})$ for a generic dSph with $r_{\rm s} = 0.5$ kpc: smooth (thick dashed lines) and subclumps (thin dotted lines). With this rescaling, the case $d = 10$ kpc (stars) superimposes on the case $d = 100$ kpc (empty and full circles).

with

$$F_{[\beta_{\rm int}]} = \int_0^{\alpha_{\rm int}} F_{[\beta_{\rm int},\alpha_{\rm int}]}\,\mathrm{d}\alpha'_{\rm int} \tag{C4}$$

and

$$F_{[\beta_{\rm int},\alpha_{\rm int}]} = \sin(\alpha_{\rm int}) \int_0^{l_{\rm max}} \mathcal{F}[r(l,\beta_{\rm int},\alpha_{\rm int})]\,\mathrm{d}l. \tag{C5}$$

For small integration angles and the case of a flat enough profile, the integrand in equations (C4) and (C5) does not vary much with $\alpha_{\rm int}$, so that for the smooth ($\mathcal{F} \equiv \rho^2$) and the mean subclumps ($\mathcal{F} \equiv \rho$), we have, respectively,

$$J_{\rm sm} \propto \alpha_{\rm int}^2 \quad \text{and} \quad \langle J_{\rm subcl}\rangle \propto \alpha_{\rm int}^2\,. \tag{C6}$$

Fig. C2 shows the integration angle dependence for the smooth $(1-f)^2 J_{\rm sm}$ (dashed lines) and the subclump mean $\langle J_{\rm subcl}\rangle$ (dotted lines) contributions. (The pointing direction is towards the dSph centre.)

For $\gamma = 0$ (solid black circles), the $\alpha_{\rm int}^2$ scaling holds up to $\alpha_{\rm int}^{\rm crit} \sim 3^\circ$ if $d = 10$ kpc (as given by equation C2). A plateau is reached when the entire emitting region of the dSph is encompassed (i.e. for a few $r_{\rm s}/d$). For $\gamma = 1$ (blue empty circles), the curves are slightly more difficult to interpret, as the profile is not steep enough for it to be considered fully point like (and thus 'independent' of $\alpha_{\rm int}$), given the integration angles considered.[20] Finally, the rescaling used in Fig. C2 implies

$$J_{\rm d1}(\alpha_{\rm int}) = J_{\rm d2}\left(\alpha_{\rm int}\frac{d_2}{d_1}\right) \times \left(\frac{d_2}{d_1}\right)^2. \tag{C7}$$

[20] The dependence can be understood by means of the toy-model formulae (B6) and (B7). For $\alpha_{\rm int} < \alpha_{\rm int}^{\rm crit}$, we have

$$J_{[\gamma \gtrsim 0.5]} \propto r_{\rm s}^{2\gamma} \times (\alpha_{\rm int} d)^{3-2\gamma}\,.$$

For $\gamma = 1$ (empty blue circles), J is then expected to scale linearly with $\alpha_{\rm int}$, which is observed for the smooth (dashed blue line) and to some extent for the subclump contribution (dotted blue line). However, for the latter, the transition region (around $r_{\rm s}$) falls from a slope $\alpha = 1$ towards an outer slope $\beta = 3$ (instead of falling from $\alpha^2 = 1$ to $\beta^2 = 6$). Hence, for $\alpha_{\rm int} > \alpha_{\rm int}^{\rm crit}$, the subclump contribution continues to build up gradually.

Table D1. Maximum boost and transition regime, that is, $(\alpha_{\rm int} d)_{B=1}$ in deg kpc, for which $B = 1$, for various smooth/subclump parameters for three inner slopes γ (for the smooth).

Configuration[a]	$\gamma = 0$	$\gamma = 0.5$	$\gamma = 1$
		$B_{\rm max}\|(\alpha d)_{B=1}$	
Reference[b]	1.9|19	2.2|21	2.0|30
[global parameters]			
$\alpha = 1$	1.0|40	1.3|60	1.6|160
$\beta = 5$	2.3|11	2.0|18	1.3|36
$R_{\rm vir} = 6$ kpc	3.0|15	3.5|20	2.9|29
$M_{300} = 2 \times 10^7\,\mathrm{M}_\odot$	1.3|66	1.4|52	1.3|64
[subclump parameters]			
$\mathrm{d}P/\mathrm{d}V =$ Einasto[c]	1.4|...	1.7|...	1.7|22
$a = 1.7$	1.3|62	1.5|50	1.3|61
$a = 2.0$	2.8|0.2	3.4|8	2.9|16
$M_{\rm min} = 1\,\mathrm{M}_\odot$	1.5|43	1.7|37	1.5|47
$M_{\rm max} = 10^4\,\mathrm{M}_\odot$	2.4|4	2.8|14	2.5|22
$f = 0.5$	3.4|10	4.2|16	3.5|25
$\rho_{\rm subcl} =$ Einasto	8.7|0.05	10.6|0.35	9.0|4
$c_{\rm vir} \times 2$	7.6|0.06	9.3|0.4	7.9|4.5

[a] All parameters are as for *reference*, except those quoted.
[b] Reference configuration ($M_{300} = 10^7\,\mathrm{M}_\odot$):
(i) $\rho_{\rm sm}$ with $(\alpha, \beta, \gamma) = (1, 3, \gamma)$ and $\mathrm{d}P/\mathrm{d}V \propto \rho_{\rm sm}$;
(ii) $R_{\rm vir} = 3$ kpc and $r_{\rm s} = 1$ kpc (for $\rho_{\rm sm}$ and $\mathrm{d}P/\mathrm{d}V$);
(iii) $\mathrm{d}P/\mathrm{d}M = M^{-a}$ ($a = 1.9$) and $M_{\rm sub} \in [10^{-6}$–$10^6]\,\mathrm{M}_\odot$;
(iv) $f = 0.2$, $\rho_{\rm subcl} =$ NFW and $c_{\rm vir}$–$M_{\rm vir} =$ B01.
[c] Einasto parameters taken from Merritt et al. (2006).

APPENDIX D: COMPLEMENTARY STUDY OF THE BOOST FACTOR

In Section 2.3.2, we concluded that the boost could not be larger than a factor of 2 for all configurations where the subclump spatial distribution follows that of the smooth halo in the dSph. The calculations were also made for a 'reference' configuration of the subclumps. However, the boost can be smaller (or larger) when the latter parameters are varied.

In Table D1, we systematically vary all the parameters entering the calculation in order to compare with the reference-model case. The two quantities of importance are the maximum boost possible (which is obtained when $\alpha_{\rm int}$ fully encompasses the clump) and the transition point $\alpha_{\rm int} d$ for which the boost equals 1 [the minimum value is always given by $(1-f)^2$]. The *reference* results correspond to the numbers obtained from the dotted lines in Fig. 5, that is, for $r_{\rm s} = 1$ kpc. Note that most of the values for $B_{\rm max}$ in the table would be close to unity if $r_{\rm s} = 0.1$ kpc were to be selected.

D1 Varying the [global parameters]

The four lines under '[global parameters]' keep the recipe of $\mathrm{d}P/\mathrm{d}V \propto \rho_{\rm sm}$, but some previously fixed parameters are now varied. The trend is that a sharper transition zone (larger α), a larger radius of the dSph, or a smaller mass imply a larger $B_{\rm max}$. The impact of the outer slope β depends on the value of the inner slope γ. However, the maximum boost factor reached for these parameters is never larger than ~3. The typical transition value lies around 20 deg kpc , which corresponds, for a dSph located 100 kpc away, to an integration angle of 0.°2. Hence, for all these configurations, a large integration angle should be preferred (this is even worse for closer dSphs).

D2 Varying the [subclump parameters]

The remaining lines under '[subclump parameters]' show the impact of the choice of the distribution of subclumps, the mass distribution parameters (minimal mass and maximal mass of the subclumps, slope a of dP/dM) and the density profile of the subclumps. Relaxing the condition dP/d$V \propto \rho_{\rm sm}$ has no major impact. In Springel et al. (2008), a simple Einasto profile with universal parameters was found to fit all haloes (from the Aquarius simulation) independently of the halo mass. For that specific case, we use the values found for the Galaxy in Merritt et al. (2006). The Einasto profile is steeper than $\gamma = 0$, but it decreases logarithmically inwards. Only for $\gamma \gtrsim 1$ (for the smooth component) such a model is able to marginally increase the maximum boost with respect to the reference model (instead of decreasing it), which is not unexpected.[21] Varying the mass distribution slope a is understood as follows: for $a \approx 1.9$, all decades in mass contribute about the same amount. When a is decreased, the less massive subhaloes dominate, whereas for $a \gtrsim 1.9$, the most massive subhaloes dominate the luminosity (e.g. fig. 4 of Lavalle et al. 2008). This has to be balanced by the fact that the fraction of DM going into subclumps remains the same ($f = 0.2$), regardless of the value of a, so that the total number of clumps in a mass decade also changes. The net result is a smaller boost when a is decreased, and a larger boost from the more massive substructure when α is increased. In a similar way (a is now fixed to 1.9 again), the mass also has impact on B, but in a marginal way. The only sizeable impact comes from varying the fraction of mass into clumps, the subclump profile or the concentration of subclumps. In the first case, when f increases, the smooth signal decreases by $(1 - f)^2$, whereas the subclump signal increases as f. Even if f is increased up to 50 per cent, which is very unlikely (recent simulations such as Springel et al. 2008 tend to give an upper limit of $f \lesssim 10$ per cent), this gives only a mild enhancement. In the second configuration, the NFW profile for the subclumps is replaced by an Einasto one. Despite its logarithmic slope decreasing faster than the NFW slope $\gamma = 1$ below some critical radius, the latter profile is known to give slightly more signal than the NFW one [$\rho_{\rm Einasto}(r) > \rho_{\rm NFW}(r)$ for a region that matters for the J calculation]. This results in a boost close to 10, regardless of the dSph's smooth profile. Finally, we recall that the B01 $c_{\rm vir}$–$M_{\rm vir}$ relation is used to calculate the value of the scale parameter for any subclump mass. In the last configuration, the concentration parameter is simply multiplied by a factor of 2, which is probably not realistic. Again, the same boost of $\sim$10 is observed. Accordingly, for these last two cases, the transition angle is reduced, and corresponds to $\alpha_{\rm int} < 0.^{\circ}01$ (for a dSph at 100 kpc).

To conclude, although boosts by as large as a factor of 10 can be obtained through suitable combinations of parameters, most of these combinations are unlikely and require the signal to be integrated on large angles.

APPENDIX E: IMPACT OF THE PSF OF THE INSTRUMENT

Fig. E1 shows the impact of the instrument angular resolution on the 80 per cent containment radius for J (for the generic dSphs studied in Section 3). The solid line corresponds to the quadrature approximation given by equation (15), whereas the symbols correspond to the convolved PSF$*$halo profile. The PSF is described by the sum of two Gaussians and is a scaled (factor of 2 improved) version of the PSF appropriate for the HESS at 200 GeV. Calculated haloes for a range of α, β, γ models consistent with the stellar kinematics of the classical dSphs are shown as the grey squares. The quadrature sum approximation used in this work is shown as a solid line.

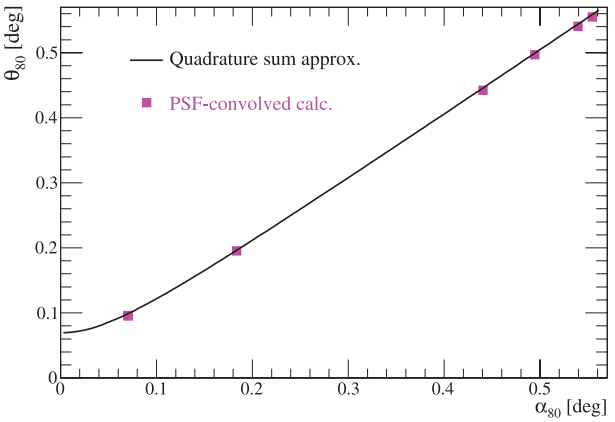

Figure E1. 80 per cent containment radius (θ_{80}) of PSF-convolved DM annihilation halo models versus α_{80}.

APPENDIX F: CONFIDENCE LEVELS AND PRIORS

In this appendix, we describe how CIs for the quantities such as $\rho(r)$ or J are chosen.

F1 Sensitivity of the result to the choice of prior

In the Bayesian approach, the PDF of a parameter x is given by the product of the MCMC output PDF $\mathcal{P}(x)$ and the prior $p(x)$. The resulting PDF is therefore subjective, since it depends on the adoption of a prior. However, whenever the latter is not strongly dependent on x, or if $\mathcal{P}(x)$ falls in a range where $p(x)$ does not strongly vary, the PDF of the parameter becomes insensitive to the prior. This happens, for instance, if the data give tight constraints on the parameters.

In our MCMC analysis, we assumed a flat prior for all our halo parameters, as there is no observationally motivated reason for doing otherwise. Note, however, that flat priors on the model parameters do not necessarily translate into flat priors on quantities derived from those parameters. Specifically, the flat priors on our model parameters imply a non-flat prior on the DM density (and also on its logarithm) at a given radius, and hence a non-flat prior on J. In principle, it is possible to choose a combination of priors for the parameters that would translate into flat priors on $\rho(r)$, but we have not done so here. The general impact of such choices, and the methodology to study the prior-dependent results, has been discussed in the context of cosmological studies by Valkenburg, Krauss & Hamann (2008). In this study, we only use a flat prior on the parameters (or on the log for $r_{\rm s}$ and $\rho_{\rm s}$). The test with artificial data demonstrates that our reconstructed ρ and J values are sound.

[21] For smaller γ, the smooth distribution, in that case, is flatter than the subclump one, so that the boost is larger than 1 for small $\alpha_{\rm int}$ and the transition where $B = 1$ is ill-defined. However, such a configuration is highly unlikely as it is exactly the opposite of what is observed in all N-body simulations.

F2 CIs for $\rho(r)$ and cross-checks

F2.1 Definition

CIs Δ_x, associated with a CL x per cent, are constructed from the PDF. The asymmetric interval $\Delta_x \equiv [\theta_x^-, \theta_x^+]$, such as

$$\mathrm{CL}(x) \equiv \int_{\Delta_x} \mathcal{P}(\theta)\mathrm{d}\theta = 1 - \gamma,$$

defines the $1 - \gamma$ CL, along with the CI of the parameter θ. We rely on two standard practices for the CI selection. The first one (used only in this appendix) is to fix θ_x^- to be the lowest value of the PDF. The CLs then correspond to quantiles. This is useful for the CI selection of χ^2 values to ensure that the best-fitting value of a model (i.e. the lowest χ^2) falls in the CI (see e.g. fig. 7 of Putze et al. 2009). In the second approach, the CI, that is, θ_x^- (θ_x^+), is found by starting from the median θ^{med} of the PDF and decreases (increases) θ_x until we get x per cent/2 of the integral of the PDF. This approach ensures that the median value of the parameters falls in the CI; any asymmetry in the CI illustrates the departure from a Gaussian PDF: this is the one used throughout this paper.

F2.2 Comparison of several choices for the PDF of $\rho(r)$

Fig. F1 shows the projection for each r of the PDF calculated from the output MCMC file. To do so, $\rho(r)$ is calculated for each entry of the thinned chains and then stored as an histogram. This results in 'boxes': the larger the box, the more likely the value of $\rho(r)$. From this distribution, we can calculate the median (thick solid black line) and the most probable value (thick dotted black line). The thick solid red line corresponds to the model having the smallest χ^2 value. We see that the latter differs from the median one for this dSph, though they can be close for other dSphs in our sample. In this paper, as our analysis is based on the Bayesian approach, we disregard the best-fitting model and only retain the median value.

In the first approach, the 68 and 95 per cent CLs are calculated from the distribution ρ_r (at each r). They are shown as the dashed and dotted thick black lines. Note that none of the above lines corresponds to a *physical* configuration of $\rho(r)$.

The second approach is to construct the 68 per cent CLs from a sampling of the (still) correlated parameters. This is achieved by using all sets of parameters $\{\boldsymbol{\theta}\}_{x\,\mathrm{per\,cent\,CL}} = \{\boldsymbol{\theta}_i\}_{i=1,\ldots,p}$, for which

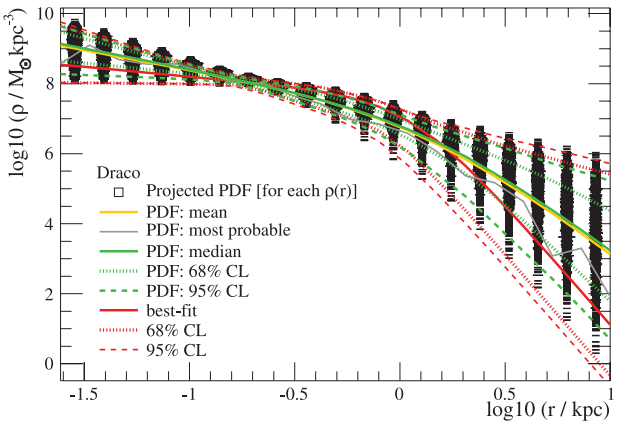

Figure F1. Projected distribution of $\log_{10}(\rho)$ along with the values of several other estimators for the MCMC analysis of Draco. In this box projection, the larger the box, the most likely the probability of $\log_{10}(\rho)$. For instance, in the top panel, for $\log_{10}(r) = -1.5$, the PDF of $\log_{10}(\rho)$ is distributed in the range [8–10] and peaks around 9.5.

$\chi^2(\boldsymbol{\theta}_i)$ falls in the 68 per cent CL of the χ^2 PDF (see above). Once these sets are found, we calculate $\rho(r)$ for each of them, and keep the maximum and minimum values for each position r. This defines envelopes of $\rho(r)$ (CIs are found for each r). This is shown as the dotted and dashed red lines. Such an approach was used in Putze et al. (2009). The CLs obtained from it are larger than the previous one. In the above paper, the uncertainties were small even with that method, so that was not an issue. However, in this study, this makes a huge difference in the resulting value CL of J.

In order to check which approach is the correct one, we bootstrapped the Draco kinematic data and calculate from the collection of $\rho(r)$ from each bootstrap sample the median value and the uncertainty. The first approach, where the CLs are directly calculated from the full set of MCMC samples, was in agreement with the bootstrap approach, meaning that the second one biases the results towards too large uncertainties. The results of this paper thus rely on the first and correct approach.

APPENDIX G: ARTIFICIAL DATA SETS: VALIDATION OF THE MCMC ANALYSIS

In this section, we examine the reliability of the Jeans/MCMC analysis by applying it to artificial data sets of 1000 stellar positions and velocities drawn directly from distribution functions with constant velocity anisotropy. We assume the form $L^{-2\beta_{\mathrm{aniso}}} f(\varepsilon)$ for the distribution functions, where the (constant) velocity anisotropy is given by $\beta_{\mathrm{aniso}} = 1 - \sigma_{\mathrm{t}}^2/\sigma_{\mathrm{r}}^2$, with σ_{t}^2 and σ_{r}^2 being the second moments of the velocity distribution in the tangential and radial directions, respectively. The function $f(\varepsilon)$ is an unspecified function of energy ε which we determine numerically using an Abel inversion once the halo model and stellar density are specified (Cuddeford 1991). We used the same models as used in Walker et al. (2011), but we present here a more general study. The set of artificial data covers a grid of models with $\gamma = 0.1, 0.5, 1.0, r_{\mathrm{h}}/r_{\mathrm{s}} = 0.1, 0.5, 1.0$ and $\beta = 3.1$. For each halo model, we assume β_{aniso} values of 0 (isotropic), 0.25 (radial) or -0.75 (tangential): the β_{aniso} values for the anisotropic models are chosen to give models with roughly equivalent levels of anisotropy (in terms of the ratios of the velocity dispersions in the radial and tangential directions). We also generate a grid of models with a steeper inner slope $\gamma = 1.5$ and $\beta = 4.0$. In all cases, the haloes contain $\sim 10^7\,\mathrm{M}_\odot$ within 300 pc. We mimic the effects of observational errors by adding Gaussian noise with a dispersion of $2\,\mathrm{km\,s^{-1}}$ to each individual stellar velocity generated from the distribution function. The reconstruction depends on the choice of the prior γ_{prior}, and this effect is explored in the two sections below.

G1 Prior: $0 \leq \gamma_{\mathrm{prior}} \leq 1$ versus $0 \leq \gamma_{\mathrm{prior}} \leq 2$

We start with the free γ_{prior} analysis (see Section 5.1) based on two different priors. The top panels of Fig. G1 show the ratio of the reconstructed median profile to the true profile. There are no significant differences for $\rho(r \gtrsim 1\,\mathrm{kpc})$ when using the prior $0 \leq \gamma_{\mathrm{prior}} \leq 2$ (top left-hand panel) or $0 \leq \gamma_{\mathrm{prior}} \leq 1$ (top right-hand panel): at large radii, the profile does not depend any longer on the γ parameter. However, it is striking to see that restricting the prior to $0 \leq \gamma_{\mathrm{prior}} \leq 1$ greatly improves the determination of the inner regions for the profile, regardless of the value of γ_{true}. Even for $\gamma_{\mathrm{true}} = 1.5$ (green curves), using an incorrect prior does not degrade too much the reconstruction of the profile.

This result is further emphasized when looking at J. The bottom panels of Fig. G1 are plotted with the same scale to emphasize the difference. As J integrates over the inner parts of the profile,

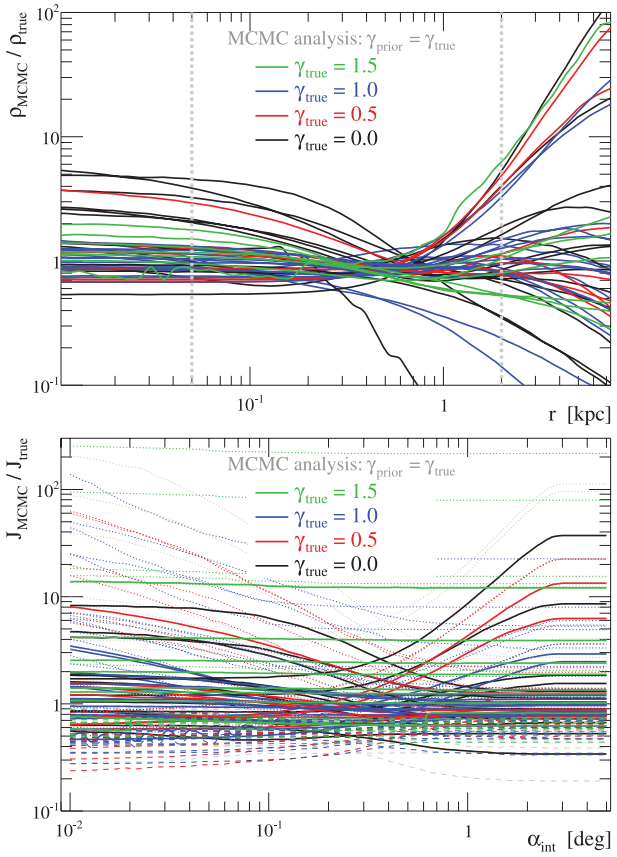

Figure G1. Ratio of the MCMC profile to the true profile. The lines are colour-coded with respect to the value of the true inner slope γ_{true} of the artificial data. Top panels: ratio of the median $\rho(r)$. The two vertical grey dashed lines correspond to the typical range within which the artificial data bins are taken. Bottom panels: ratio of $J(\alpha_{int})$ for the artificial dSphs located at 100 kpc. Left-hand panels: MCMC analysis with the prior $0 \leq \gamma_{prior} \leq 2$. Right-hand panels: the prior is $0 \leq \gamma_{prior} \leq 1$.

the median MCMC value can strongly differ from the true value for cuspy profiles. This difference can reach up to five orders of magnitude (over the whole range of α_{int}) for $\gamma_{true} \gtrsim 0.5$ when using the prior $0 \leq \gamma_{prior} \leq 2$. The prior $0 \leq \gamma_{prior} \leq 1$ does generally better and, accordingly, the CIs are much smaller than for the other prior (for any integration angle).

The behaviour of the $\gamma_{true} = 1.5$ case is unexpected. Using the prior $0 \leq \gamma_{prior} \leq 1$ does better than the other one for any integration angle. Indeed, even if the reconstructed median value is shifted by a factor of 10, its CLs correctly encompass the true value. It does better than the $0 \leq \gamma_{prior} \leq 1$ prior, which correctly provides CLs (that bracket the true value), but which are completely useless as these CLs can vary on approximately eight orders of magnitude.

G2 Strong prior: γ_{prior} fixed

In Fig. G2 below, we use a prior $\gamma_{prior} = 0$ for models having $\gamma_{true} = 0$, a prior $\gamma_{prior} = 0.5$ for models having $\gamma_{true} = 0.5$, etc.

A comparison of Figs G1 (using $0 \leq \gamma_{prior} \leq 1$ or $0 \leq \gamma_{prior} \leq 2$) and G2 (fixed γ_{prior}) shows that the latter prior only slightly improves the precision of the J-factor reconstruction for $\gamma_{true} = 0$, 0.5 and 1. However, if $\gamma_{true} = 1.5$ (green curves), although the corresponding J-factor is now better reconstructed than when using the prior $0 \leq \gamma_{prior} \leq 2$ (Fig. G1, top left-hand panel), it is surprisingly less reliable than the strongly biased $0 \leq \gamma_{prior} \leq 1$ prior.

The main conclusion is that the knowledge of γ_{true} does not help providing tighter constraints on J: the uncertainty remains a factor of a few, except when the inner profile is really cuspy ($\gamma_{true} = 1.5$), in which case it becomes strongly biased/unreliable.

APPENDIX H: OTHER RECONSTRUCTION 'BIASES' ON THE J-FACTOR

In this appendix, the MCMC analysis is performed based on the prior $0 \leq \gamma_{prior} \leq 1$, for which the analysis is found to be the most robust (see the previous appendix).

H1 Impact of the binning of the stars

Fig. H1 shows the impact of using different binnings in the MCMC analysis. The left-hand panels show the reconstructed (median) value of the velocity dispersion as a function of the logarithm of r (to emphasize the differences at small radii), for the binning used in this paper (black; where each of $\sqrt{N}$ bins has $\sqrt{N}$ member stars, where N is the total number of members), a binning with two times (red) and four times (blue) fewer bins. For Fornax and Sculptor, the profiles are insensitive to the binning chosen, so that the reconstruction of the J values' median and 68 per cent CLs (right-hand panels) is robust. For other dSphs, the adjusted velocity dispersion profile is affected either at small radii or at large radii. In the latter case, the J calculation should not be affected, as the outer part does not contribute much to the annihilation signal. In the former case, a deviation even at small radii can affect the associated J by a factor of a few. The exact impact depends on the integration angle, the distance from the dSph (which corresponds to a given radius) and the 'cuspiness' of the reconstructed profile (the J value of a core profile will be less sensitive to differences in the inner parts than would be that of a cuspy profile). For instance, Draco and Leo I both have a 2 km s^{-1} uncertainty below 100 pc, but Draco is three times closer than Leo I: their J for a given α_{int} have different behaviours (right-hand panels). The strongest impact is for Leo I that has the fewest data. The flatness of the J curve seems to indicate a cuspy profile (all the signal in the very inner parts), which we know are the least well reconstructed ones (see Appendix G1). Leo I is thus the most sensitive dSph to the binning, for which a balance between a sufficient coverage over r and small error bars cannot be achieved. The ultrafaint dSphs are expected to have even fewer stars, so that their J calculation is expected to be even more uncertain.

Overall, the choice of binning can produce an additional bias of a few on the J reconstruction. This is an extra uncertainty factor that makes Fornax and Sculptor the more robust targets with respect to their annihilation signal. Surveys in the inner parts and outer parts of Carina, Draco, Sextans, Leo I, Leo II and Ursa Minor are desired to get rid of this binning bias.

H2 Impact of the choice of the light profile

Fig. H2 shows the various median values and 68 per cent CIs of J when changing the assumptions made on the light profile. The black lines labelled 'physical' correspond to the Plummer model used for the main analysis (see equation 21); the red lines labelled 'unphysical' are also Plummer, but the physical constraint given by equation (25) is relaxed; the blue lines and green lines correspond, respectively, to a light profile modelled with an (α, β, γ) profile in

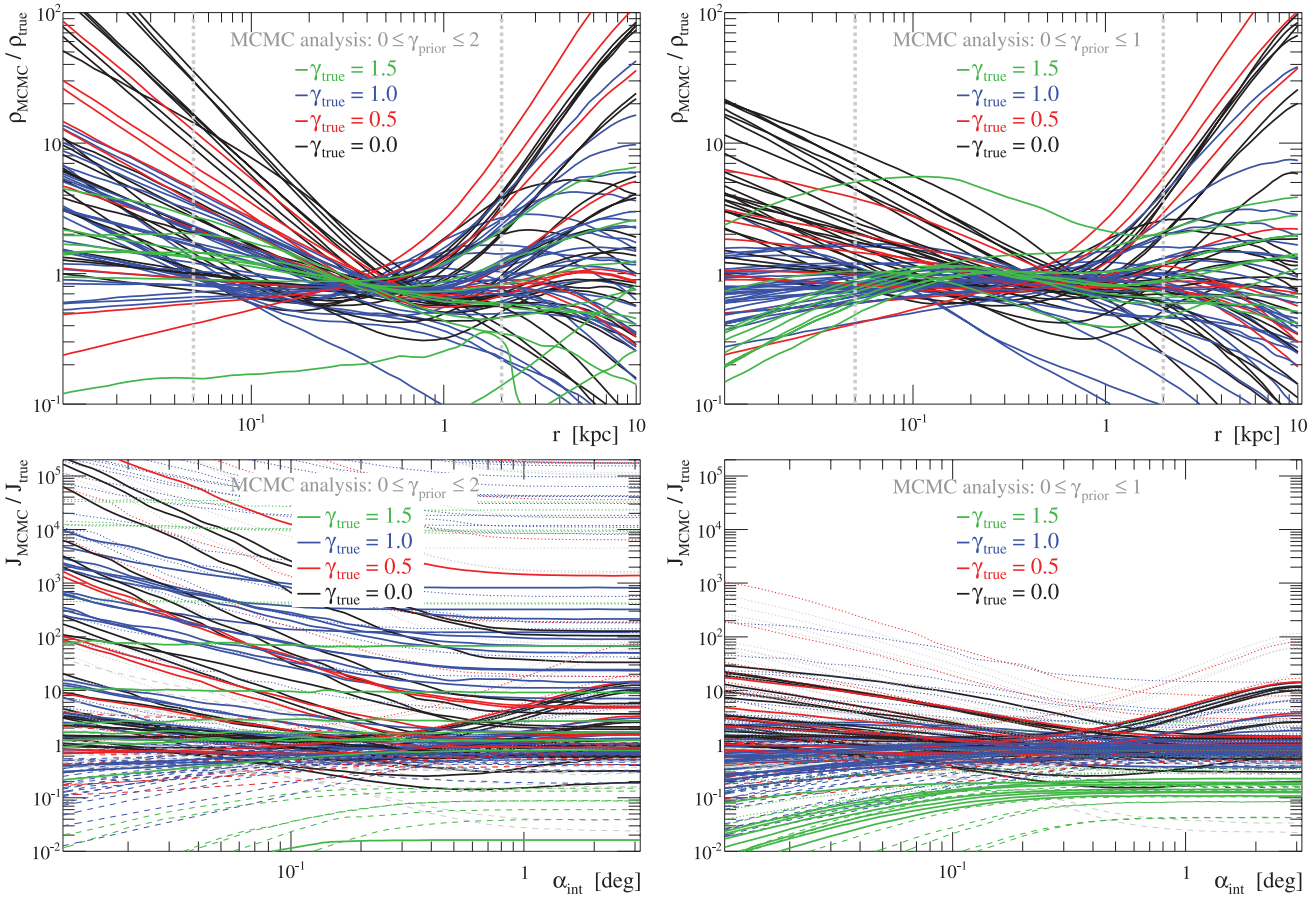

Figure G2. Fixed γ_{prior} MCMC analysis. Top panel: $\rho(r)$. Bottom panel: $J(\alpha_{int})$.

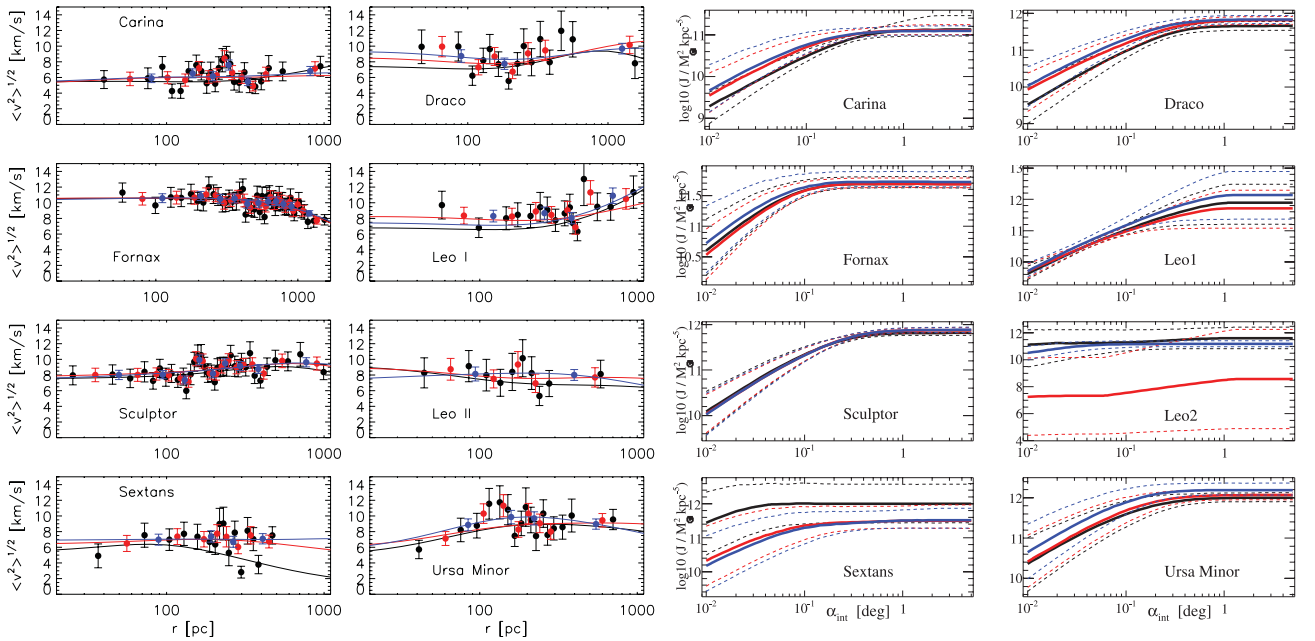

Figure H1. For the eight classical dSphs, impact of using several binnings of the stars: black is the binning used throughout this paper (i.e. $\sqrt{N}$ bins), red has $\sqrt{N}/2$ bins and blue has $\sqrt{N}/4$ bins. Left-hand panels: velocity dispersion as a function of $\log(r)$ (symbols are data and lines are the MCMC median values based on the data). Right-hand panels: corresponding median values and 68 per cent CI for $J(\alpha_{int})$.

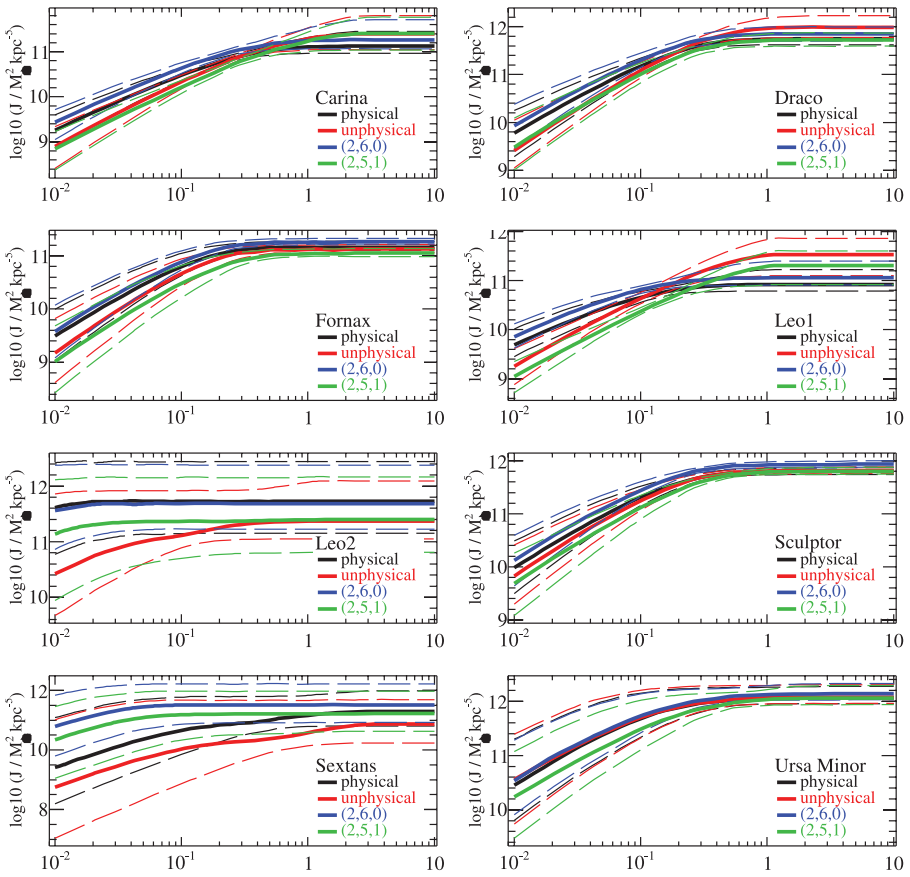

Figure H2. For the eight classical dSphs, impact of using different light profiles (see text). The solid lines are the MCMC median values and the dashed lines are the 68 per cent CIs for $J(\alpha_{\rm int})$.

order to get a steeper outer slope (2, 6, 0) or a steeper inner slope (2, 5, 1) with respect to the Plummer profile.

Regardless of the light profile used, we recover similar critical angles for which J is the most constrained. The impact on the J value is strongest for the least-well-measured profiles (Leo II and Sextans), but is contained within the 95 per cent CI and marginally within the 68 per cent CL.

SUPPORTING INFORMATION

Additional Supporting Information may be found in the online version of this article.

ASCII files. ASCII files containing the most-likely, 68 and 95 per cent CLs on the quantity $J(\alpha_{\rm int})$ for the eight classical dSphs that we analysed.

Please note: Wiley-Blackwell are not responsible for the content or functionality of any supporting materials supplied by the authors. Any queries (other than missing material) should be directed to the corresponding author for the article.

This paper has been typeset from a TEX/LATEX file prepared by the author.